2022

Thermofluidic Characterization of Carbon Dioxide Near Critical Conditions at Microscale

Anatoly Parahovnik
University of Central Florida

THERMO-FLUIDIC CHARACTERIZATION OF CARBON DIOXIDE NEAR CRITICAL CONDITIONS AT MICROSCALE

by

ANATOLY PARAHOVNIK

M.Sc. Technion-Israel Institute of Technology, 2015

B.Sc. Technion- Israel Institute of Technology, 2010

A dissertation submitted in partial fulfillment of the requirements
for the degree of Doctor of Philosophy
in the Department of Mechanical and Aerospace Engineering
in the College of Engineering and Computer Sciences
at the University of Central Florida
Orlando, Florida

Spring Term

2022

Major Professor: Yoav Peles

ABSTRACT

This work revealed the thermo physical characteristics of near critical and supercritical carbon dioxide at the micro scale. The results include the extension of flow boiling heat transfer correlations, boiling inception, near critical bubble dynamics, thermalization mode shift, Joule Thomson effect and pressure drop evaluation. It was found that extremely low superheat temperatures are required for boiling inception near the critical conditions (i.e., T=31.4 °C, and P=7.37 MPa), and boiling heat transfer correlations were extended up to a reduced pressure of 0.99. The work also revealed a significant enhancement of the heat transfer coefficient as the critical conditions approached, which was partially attributed to a shift of the thermalization mode (i.e., up to ×3 higher compared to lower reduced pressures). For the first time, the thermalization shift in convective micro scale flows was visualized and measured using marker-less technique. Additionally, it was found that near the critical conditions the growth and translation of bubbles slowed down and were driven by thermal diffusion (i.e., asymptotical thermally driven models described the bubble dynamics well). Moreover, the interactions between the bubbles had major influence on the bubbles' growth rate. Subsequently, a micro-orifice was integrated into the microchannel to demonstrate the importance and applicability of the Joule Thomson coefficient (JTh) in the vicinity of the critical point of CO2. In the experiments the fluid's temperature was reduced to -10.8 °C, which is 34 °C below ambient, without complicated thermal insulation due to the sustainable Joule-Thomson effect. Lastly, pressure drop for the micro-orifice were compared with different models (i.e., homogeneous and separated two phase flow, capillary tube, and short tube orifice correlation). The capillary tube model best predicted the measured pressure drop. To conclude, this work presents a major advancement in understanding the thermophysical behavior of carbon dioxide and will lay the foundation to its wider utilization in the future.

To:

My beloved family, Lora, Adam, and Matan

ACKNOWLEDGMENTS

I sincerely thank my advisor, Prof. Yoav Peles. He has been a beacon of knowledge, and a role model in this process. His supervision of the research was both inspirational and supportive. His guidance has shaped my personality and will lead me in all my future professional endeavors.

My committee members at UCF; Prof. Shawn Putnam, Prof. Aravinda Kar, and Prof. Subith Vasu were very supportive through the course of my PhD. I thank them for their feedback about my research plan, during the course work, and in the process of research.

I am very fortunate and thankful to have great lab mates that have worked with me through the research; A special thank you to Yingying Wang, Stephen Adeoye, Uday Manda, and all other professional and personal friends along the way like Yftach Gepner, Yoni Sorokin and many more.

Most importantly, great thank you to Lora, my better half; that have agreed to make this journey with me. Without you this would have not been possible, your emotional, professional, and social intelligence have made this a once in a lifetime journey.

And finally, to my sons, Adam and Matan, who are the joy and happiness that had driven me forward and welcomed me back home at the end of each and every day.

TABLE OF CONTENTS

LIST OF FIGURES

LIST OF TABLES

LIST OF ACRONYMS/ABBRIVIATIONS

Nomenclature:

A – Cross sectional area of the channel, m^2

A_1 – Fitting coefficient for parameter 'a'

A_2 – Fitting coefficient for parameter 'a'

A_i – Song et al. correlation variables

A_L – Cross sectional area occupied by liquid phase, m^2

A_{Ch} – Churchill's correlation constant

a – fitting parameter to account for bubble-to-bubble interactions

a_i – Kandlikar's correlation constants (for critical heat flux calculation)

B – Churchill's correlation constant

B_i – Song et al. correlation variables

Bo – Boiling number (i.e., $Bo = \frac{q''}{G \cdot h_{fg}}$)

C –Pressure drop correlation constant

C_i – Kandlikar's correlation constants

Ca – Capillary number, (i.e., $Ca = \frac{\mu_l \cdot G}{\rho_l \cdot \sigma}$)

C_o – Convection number (i.e., $C_o = \left(\frac{1}{x} - 1\right)^{0.8} \cdot \left(\frac{\rho_g}{\rho_l}\right)^{0.5}$)

C_p – Specific heat, J/kgK

C_v – Specific heat at constant volume, J/kgK

D_h – Tube diameter or channel hydraulic diameter, m

D – Bubble diameter, m

dp – Pressured difference for evaluation of density's partial derivative $(\partial\upsilon/\partial p)_h$ for the capillary tube model (100 kPa)

E – Fidel's correlation constant (Separated flow model)

F – Fidel's correlation constant (Separated flow model)

F – Shah's correlation coefficient

F_i – Song et al. correlation variables (i =1 or 2)

F_l – Kandlikar's correlation constant (i.e., F_l=2.1 for CO_2)

Fr – Froude number with all mass flux considered as a liquid (i.e., $Fr = \frac{G^2}{\rho_l^2 \cdot g \cdot D}$)

f – Friction factor

G – mass flux, kg/m^{2}s (For orifice analysis it calculated using orifice's cross section)

Gr^* – Modified Grashof number for the turbulent film boiling model

g – Gravitational constant, m^2/s

H – Fidel's correlation constant (Separated flow model)

h – Heat transfer coefficient, W/m^{2}K

h – channel's height, m

h – Specific enthalpy (J/kg)

h_{fg} – The heat of vaporization, J/kg

h_{fg}' – Heat of vaporization for film boiling, J/kg

JT_h – Joule-Thomson coefficient

$K_{2,CHF}$ – variable in Kandlikar's correlation for CHF

k – Partition factor, Eq. 1 (k=3.5)

L – heated length, m

M – Molar mass kg/kmol

MAE- Mean average error, %

$\dot{m}$ – Mass flow rate (kg/s)

n – Kandlikar's correlation constant (for critical heat flux calculation)

n – number of samples

n– Number of partitions

P – Pressure, MPa

P_c – Critical pressure (P_c=7.377 MPa)

Pr – Prandtl number

P_r – Reduced pressure

q'' – Heat flux, W/m^2

R_2 – Mathematical fitting evaluation value

$R_{thermal}$ – Package thermal resistance, 3.45 m^2·K/W.

Re –Reynolds number

RTD – Resistive Temperature Detector

S – Chang et al. correlation coefficient

t – time, s

T – Temperature, K

T_c– Critical temperature (T_c=304.12 K)

U– Velocity (m/s)

u – Apparent liquid velocity, m/s

v – Bubble velocity, m/s

W– heaters diameter, m

We – Weber number, (i.e., $We_D = (G^2 \cdot D)/(\rho \cdot \sigma)$ or $We_L = (G^2 \cdot L)/(\rho \cdot \sigma)$)

w – channel's width, m

w_m – Relative velocity ratio, $w_m=(v-u)/u$

x – Mass quality

x – position, m

Y – Cheng et al. correlation coefficient

Greek letters:

α – Thermal diffusivity, m^2/s

γ – Specific heats ratio, (i.e. C_p/C_v)

Δ – Property differences (i.e., $\Delta T_{sat}=T_{RTD}-T_{sat}$)

ΔP– the i-th partition pressure difference for orifice's pressure drop analysis, Pa

ΔT_{sat} – superheat temperature, K

ΔT_{sub} – subcooled temperature, K

Δt – time difference between frames, s

Δx – position step between frames, m

Δx– the i-th partition length for orifice partition, m

δ – Liquid film thickness, m

ε – Relative roughness (i.e., $870e^{-9}/81e^{-6} = 0.0107$)

ε – Void fraction

ε_m – Void fraction in Cheng et al. correlation [1]

θ – Flow contact angle, rad

κ − Thermal conductivity of the liquid, W/mK

μ – Dynamic viscosity, Pa·s

ν – Kinematic viscosity (m^2/s)

ρ – Density, kg/m^3

σ – Surface tension, N/m

σ_{SB} – Stefan-Boltzmann constant, $5.67 \cdot 10^{-8}$ W/m^2K^4

υ – Specific volume (m^3/kg)

ϕ – Separated flow factor

Ψ – Ratio of the two-phase heat transfer to a liquid-portion heat transfer, (i.e., $\Psi=h_{TP}/h_l$)

Subscripts:

@x= – The equation is evaluated at the relevant quality.

1,2,3,4 – RTDs locations

∞ – Fluid's bulk property

a – Pressure drop due to acceleration.

amb – Ambient measured property

av – Conditions averaged between the inlet and exit.

b – Bubble

bs – Boiling suppression regime

c – Microchannel.

calc – Theoretically calculated value

cb – Convective boiling regime

CHF– Critical Heat Flux

D – Diameter base

dry – dry contact

exit – Exit.

exp – experimentally measured value

f – film boiling

f – Pressure drop due to friction.

g (v) – Gas (vapor) phase

H – Homogenous

i – Numerical counter for correlations' constants

i – Orifice subdivision element.

inlet – Inlet.

L – Length based

l – Liquid phase

lo (L_o) – All the mass flux considered liquid

loss – Thermal losses related property

M – Mist regime

m – Mean (Average)

n – nucleation site relative to the heater's leading edge, m

nb – Nucleate boiling regime

o – Orifice.

RTD – Property measured or evaluated by the RTD

R – Receding contact

r – Radiative component

sat – Saturation

sp – Single-phase.

TP (tp) – Two-phase

wet – Boiling region of the heat exchange area

1. INTRODUCTION

Carbon Dioxide (CO_2) is a promising fluid for a range of applications. From lab-on-chip chemical reactors [2] to large scale power cycles [3]–[6]. Micro scale chemical reactors are more efficient, inexpensive and environmentally friendly for chemical production processes than their large-scale counterparts. For power cycles, the use of supercritical CO_2 as a working fluid reduces the footprint of power plants by a factor of 4, compared to steam-based Rankine or Bryton power cycles while maintaining the same power output. Such reduction allows to produce offshore and more efficient portable power plants [7]. CO_2 is a natural coolant with low Ozone Depletion Potential (ODP) and low Global Warming Potential (GWP), Table. 1, which makes it a more environmentally friendly and viable candidate to replace artificial refrigerants that is widely used in refrigeration systems.

Table 1 -Different Coolants and their properties, CO_2 has a low ODP and GWP

Refrigerant	**R22**	**R134a**	**R410a**	**R407C**	**R290 (Propane)**	**R744 (CO_2)**
ODP	0.05	0	0	0	0	0
GWP	1700	1300	1900	1600	3	1

Portions of this chapter previously appeared in:

A. Parahovnik, M. Asadzadeh, S. S. Vasu, and Y. Peles, "Subcooled Flow Boiling of Carbon Dioxide Near the Critical Point Inside a Microchannel," *Phys. Rev. Appl.*, vol. 14, no. 5, p. 054050, Nov. 2020.

Anatoly Parahovnik, Yoav Peles, 2022, "High pressure saturated flow boiling of CO2 at the micro scale", *International Journal of Heat and Mass Transfer*, Vol. 186.

Anatoly Parahovnik, Yoav Peles, 2022, "Bubble dynamics in a subcooled flow boiling of near-critical carbon dioxide", *International Journal of Heat and Mass Transfer*, Vol. 183, Part C.

Anatoly Parahovnik, Yoav Peles, 2022, "Heat transfer mode shift to adiabatic thermalization in near-critical carbon dioxide with flow boiling in a microchannel", *International Journal of Heat and Mass Transfer*, Vol. TBD.

A. Parahovnik, P. Ahmed, Y. Peles, "Pressure drop and Joule-Thomson effect in a micro orifice with trans critical carbon dioxide flow", *Journal of supercritical fluids*, under review.

The use of CO_2 as a coolant begun in the 19th century primarily for portable marine refrigeration systems [8]. Because of its high operational pressure and the emergence of alternative artificial coolants, such as Chlorofluorocarbon (CFC) and Hydrochlorofluorocarbon (HCFC) research pertinent to CO_2 subdued. In recent years, CO_2 is regaining interest as a potential candidate to replace artificial refrigerants due to an increase in environmental awareness and the progress in design of pneumatic components like compressors, regulators, and valves.

At its supercritical phase CO_2 has liquid-like density and gas-like viscosity, this combined with other thermal properties suggests that supercritical CO_2 can transfer a large amount of heat with relatively small pressure drop. As such it is a good candidate for working fluid in compact systems like printed heat exchangers [9], [10].

1.1. Critical point and thermodynamic properties

Carbon dioxide has a triple point at a pressure and temperature of 0.518 MPa, 216 K, respectively. Its critical condition corresponds to a pressure of 7.3773 MPa and a temperature of 304.13 K (Fig. 1) [11]. Above the pressure and temperature of the critical point, the fluid is in a supercritical state.

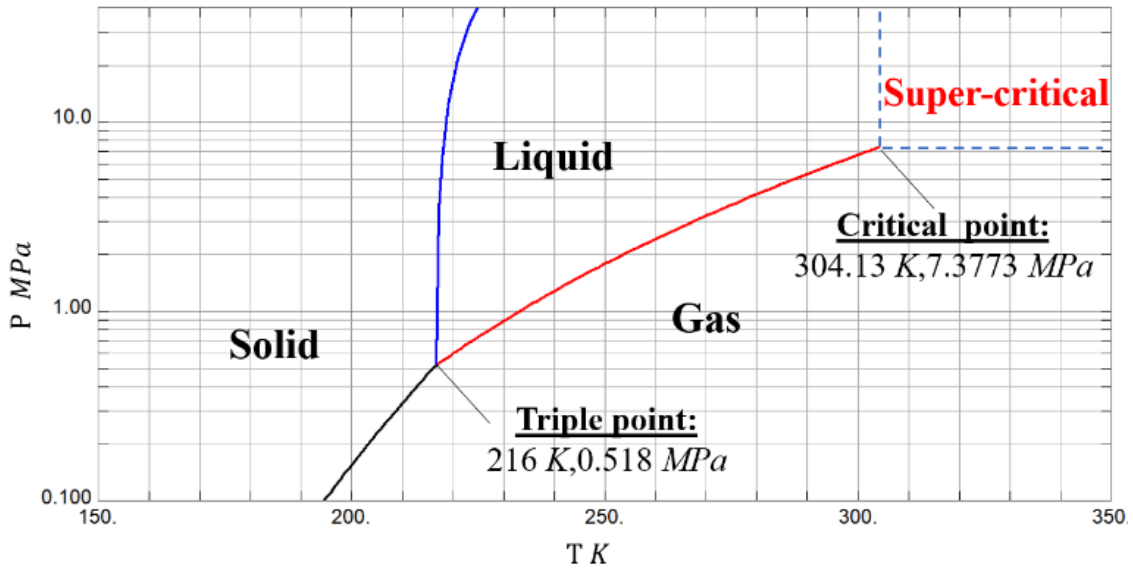

Figure 1- Phase diagram of carbon dioxide, the triple point is at 0.518 *MPa*, and 216 *K*, and critical point is at 7.3773 *MPa*, and 304.13 *K*.

Fig. 2a presents the density of CO_2, ρ, as a function of pressure for four different temperatures of 300 K, 304.13 K, 306 and 310 K. At 300 K, CO_2 is in the liquid phase for all the displayed pressure range, with no significant density change. For other temperatures, there is a significant increase in density, which means a transition from a gas and gas-like (-like refers to the supercritical phase) density values to liquid and liquid-like values. Fig. 2b. presents the dynamic viscosity, μ, as a function of temperature for pressures of 0.1 MPa, 7.3773 MPa, 10 MPa, and 14 MPa. For 0.1 MPa, CO_2 is considered gas regardless of the temperature, and the viscosity is fairly constant. For other pressures, there is a significant drop in the viscosity toward the gas-like values. These transitions are very abrupt close to the critical pressure (i.e., 7.3773 MPa) and become more gradual at elevated pressures.

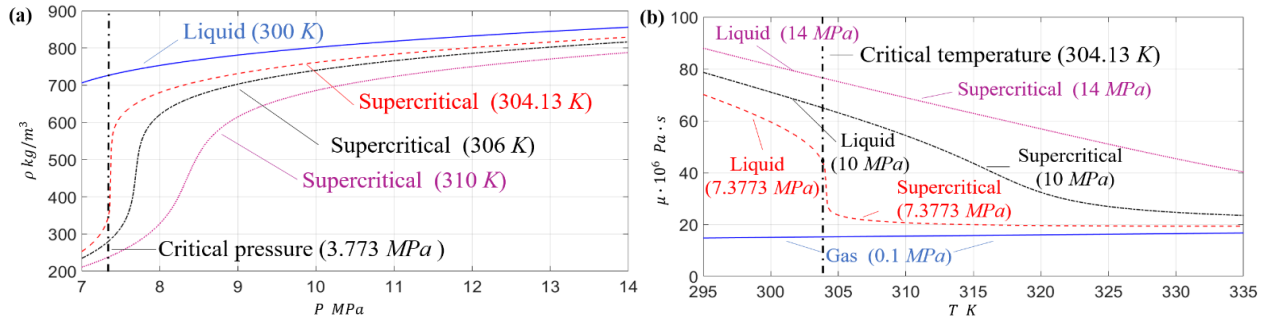

Figure 2- Density and Viscosity of CO2 in vicinity of the critical point, the density increases with the pressure and viscosity drops with temperature increase.

Specific heat (C_p), and Prandtl number (Pr) present similar behavior, Fig. 3. For 300 K, there is no significant change in C_p and Pr values; however, for above critical temperatures, there is an increase with the pressure until they reach local maxima. This collection of local maxima points is considered a pseudo-critical line that divides the supercritical phase into liquid-like and gas-like regions.

These properties variations have positive effects; for instance, the increase in density allows to reduce the needed pumping power. The decrease in the viscosity will reduce the pressure drop in the system's tubing. On the other hand, these variations also pose a challenge in understanding the heat transfer phenomena associated with CO_2.

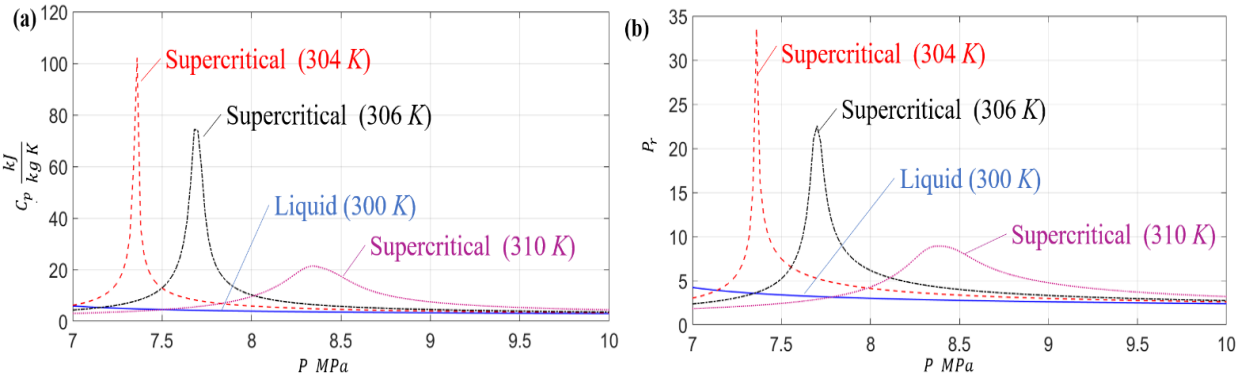

Figure 3-Specific heat (C_p) and Prandtl number (Pr) as a function of pressure and temperature, both experience local maxima at pseudo-critical temperature.

1.2. Historical perspective for cooling with micro-channels

Since the 80's, when cooling using micro channels was first demonstrated [12], micro channels were of an interest for increasing number of studies [13], Fig. 4. Micro channels are perspective method for different applications, they have a high surface to volume ratio that leads to

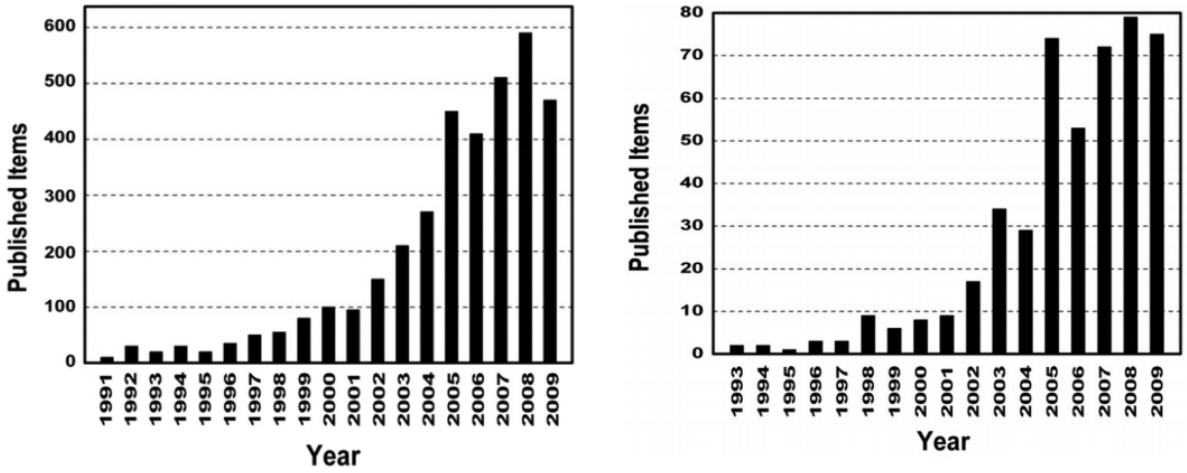

Figure 4- Microchannel related publications, LHS- single phase works, RHS- boiling or condensation processes in microchannels [13]

higher heat transfer rates, and with the growing demand for high-end cooling capabilities, micro channels become a valid solution for thermal problems. Research effort to explore the full potential of the technology were made both for single phase [14]–[18] and two phase [19]–[24] flows. Understanding of the physics involving microchannels has advanced through the years starting with answering basic questions regarding continuum and incompressibility assumptions, followed by channels' classification to macro, mini, micro, and nano size according to its diameters. Currently the main effort is focused on an implementation of the micro-channels' technology in practical applications. The majority of the research was done using common fluids and refrigerants like water, R134a, R113 and R12 which were applied at ambient pressures [25]–[29], and can be a valid solution for many applications. However, some practices in chemical processes [2], [30] and cryogenics [31]–[33] require working with high pressures. These works demonstrated the feasibility of applying high pressure in microchannels. Researching CO_2 heat transfer characteristics in the

vicinity of the critical point requires the introduction of elevated pressure levels into microchannel, a combination that is not widely practiced.

1.3. Onset of nucleate boiling and subcooled heat transfer coefficient

A century-long effort revealed many of the characteristics of flow boiling heat transfer under a range of flow and thermal conditions. Boiling is considered as one the most efficient heat transfer methods [20], [34], [35], and it is associated with extremely high heat transfer coefficients. Boiling is a complex process which involve variety of phenomena: bubble formation, thin film evaporation, boundary layer fragmentation, local convective effects like thermocapillary or Marangoni effect [36], [37] and more. Boiling at the micro- scale as a cooling method had been since early 2000, however, thermal engineers have been reluctant to integrate microchannel flow boiling in their systems because of flow instabilities, the critical heat flux (CHF) condition, and inconsistencies between available correlations. Recent results [38] suggested that these issues can be resolved with CO2, especially at reduced pressures close to unity. Nevertheless, besides a couple of studies at reduced pressures of up to 0.87 [39]–[43], not much is known about flow boiling heat transfer characteristics under such conditions.

Flow boiling scientists seek to obtain data and reveal the underlining physics controlling the onset of nucleate boiling (ONB), two-phase heat transfer coefficient (HTC), and CHF condition. Flow morphologies and a range of other effects, such as flow instabilities, have been meticulously documented and modeled. Frequently used models to predict ONB include Hsu's model [44], the Davis and Anderson model [45], and the Lienhard's correlation [46]. Numerous correlations and models have been developed to predict the two-phase HTC. Several of the more notable include the Shah's correlation [47], Kandlikar's correlation [48], and the Cheng's correlation [43]. They were developed based on experimental results at lower reduced pressures and applied to Boiling numbers that are, for the most part, below those pertinent to CO2 near the critical condition.

Despite many years of research, flow boiling near the critical condition at the microscale has been rarely studied, and data pertinent to heat transfer is missing. Therefore, knowledge about the mechanisms controlling the heat transfer process under such important conditions is lacking.

1.4. Saturated flow boiling and critical heat flux of carbon dioxide

Serious issues are currently hindering saturated flow boiling from practical implementation in micro domains, such as flow boiling instabilities [49]–[52], critical heat flux (CHF) conditions [53]–[55], and lack of robust and universal heat transfer and fluid flow models/correlations. To help resolve these issues, the Defense Advanced Research Projects Agency (DARPA) launched in 2012 the two ambitious ICECool programs [56]–[58] that greatly extended micro scale convective cooling capabilities. However, much is still to be revealed and developed to fully leverage this type of cooling method in practical applications. One of the major objectives in these types of systems calls for saturated flow boiling at high mass qualities to take advantage of latent heat of vaporization and minimize mass flow rate. However, because of the high liquid/vapor density ratio at low pressures, at the micro scale, high mass qualities are associated with an excessively thin liquid layer of a few micrometers or less in an annular flow pattern. This thin layer is seriously susceptible to rupture, and, as a result, to the formation of dry spots on the surface that leads to a much inferior thermal performance. Various techniques to preserve the integrity of the liquid film were explored, such as surface topography and morphology modifications [59]–[61], multiscale hierarchical surfaces [62], [63], etc. While these techniques show some capacity to extend the integrity of the liquid film, they have limited potential.

Recently, flow boiling of carbon dioxide (CO2) at pressures approaching the critical condition has been proposed as a potential solution to resolve this state-of-affairs [64]. Because the liquid/vapor density ratio is much reduced under these conditions, the transition from nucleate flow boiling to convective boiling and the rupture of the liquid film are delayed to much higher mass qualities. On the other hand, the beneficial heat transfer effect of the latent heat of vaporization (i.e., h_{fg}) gradually diminishes with pressure. Thus, a

"sweet" spot at high pressures in which saturated flow boiling heat transfer in microchannels can be much enhanced should be explored, and here such effort is reported.

1.5. Bubble dynamics in a subcooled flow boiling of near-critical carbon dioxide

In addition to looking into the onset, subcooled heat transfer coefficients, saturated heat transfer coefficients, and critical heat flux, it is also of interest to examine the bubble dynamics of a near critical boiling fluid. As the fluid approaches its critical condition, it experiences several fundamental property changes, such as reduced liquid-to-vapor density ratio, increased thermal conductivity of the vapor, and a drastic change in the specific heats. Therefore, flow boiling heat transfer at high reduced pressures are expected to differ, or at least be modified, relative to low pressure flows. Nucleate boiling is expected to continue dominating at much higher mass qualities than at low pressures, and conversely, the bubble dynamics might be modified. Under these conditions, it is interesting to examine the asymptotic expressions developed by Mikic et al. [65] for bubble growth. (Asymptotic solutions are simplified versions of the Rayleigh-Plesset equation [66] that provides an elegant description using little computational resources.) Specifically, inertia vs. thermal bubble growth, where the inertia growth is mainly driven by pressure gradients while thermal driven growth is linked to thermal diffusion. Thermally driven process, which is proportional to $t^{1/2}$, is slower than inertia driven growth, which is linearly proportional to time, and results in slower growth rate [67]. The evolution of bubbles differs between inertia and thermal driven growth and affects bubble dynamics.

Archival literature about bubble dynamics is rich and provides sound foundation to extend knowledge about such processes to near critical condition. Bubble growth in an infinite body of incompressible fluid was first modeled by Besant [68] and integrated by Rayleigh [69] using an energy balance. Plesset [66] extended the model by including the effect of surface tension and applying it to traveling bubbles. The asymptotic solution of Mikic et al. [65] was then derived to infer the mechanisms controlling the bubble growth (i.e., thermally or inertia controlled growth) in boiling systems. Other aspects of bubble characteristics in boiling fluids were examined, such as Hsu's model [70] that describes bubble nucleation on a heated surface by

predicting the surface roughness conditions requiring nucleation. Davis et al. [71] then integrated Hsu's model into a convective flow with thermal boundary layer developed in the vicinity of the heated surface. Mohanty et al. [72] reviewed the influence of bubble dynamics on boiling heat transfer, and concluded that bubble departure, active nuclei site density and departure frequency were important factors influencing the nature of boiling. They stated that understanding bubble dynamics is important for the formulation of generalized boiling heat transfer models. The growing interest in carbon dioxide as a cooling fluid resulted in new understanding of flow boiling near the critical conditions. For instance, Hellenschmidt et al. [38] experimentally investigated flow boiling of CO_2 in mini- and micro-channels with hydraulic diameters ranging from 0.1 mm to 2 mm, and stainless steel tubes, and reported heat transfer coefficients ranging from 10 to 50 kW/m^{2}K for saturation temperatures from -25 °C to 15 °C, respectively. Lei et al. [73] experimentally studied flow boiling heat transfer of carbon dioxide in a 4 mm stainless steel tube and concluded that active nucleation sites become denser, and the nucleated bubbles become smaller with pressure, which increased the heat transfer coefficient near the critical conditions. Pham et al. [74] numerically modeled the growth and collapse of bubbles in a near-critical carbon dioxide to better understand cavitation processes for a trans critical cycle compressor. They concluded that bubble growth and collapse were governed by the thermal layer formed within the bubbles, and therefore, was a slow process compared to non-near-critical fluid. Thome et al. [39] presented a heat transfer coefficient correlation for carbon dioxide based on experiments in horizontal tubes ranging from 0.79 mm to 10 mm. Comparison with experiments found that 86% of the data was correlated within a ±30% range. Cheng et al. [1], [40], [43] studied pressure drop and heat transfer coefficient of CO_2 for mass fluxes ranging from 50 to 1500 kg/m^{2}s and heat fluxes from 1.8 to 46 kW/m^2 and produced an updated flow map, pressure drop and heat transfer correlations. Ducoulombier et al. [41], [42] investigated pressure drop and heat transfer in a 0.529 mm tube with a mass flux of 200 kg/m^{2}s to 1200 kg/m^{2}s and heat flux ranging from 10 kW/m^2 to 30 kW/m^2 and found that the mass flux had little influence on the heat transfer coefficient while the vapor quality was influential. Hosler [75] presented a flow boiling pattern map for pressurized flow and observed deviations in the boiling patterns compared to non-pressurized flows that influenced the heat transfer and

critical heat flux conditions. These deviations were a result of the increase of vapor density compared to the liquid phase, where the former is usually neglected. Subcooled flow boiling is a condition where the fluid adjacent to the heated wall exceeds the saturation temperature, while the fluid's bulk temperature is still below it. Bubble dynamics in subcooled flow boiling was studied experimentally [76]–[78] and theoretically [79]–[81], and it was found that the bubble ebullition cycle depends on the mass flux and the subcooled degree. It is well established that starting from the onset of nucleate boiling, the contribution of nucleate boiling mode gradually increases and completely dominates the heat transfer process once fully developed boiling is established [82], and that heat transfer enhancement is a result of both vaporization of the fluid and condensation outside the thermal boundary layer and augmentation of a microlayer below the bubble [81]. However, most of the formulated theory and the models were derived using water and pertinent to boiling fluid at low reduced pressures. Therefore, knowledge about bubble dynamics under these conditions will aid the development of improved subcooled flow boiling heat transfer models pertinent to high reduced pressures. As the fluid approaches the critical pressure, the surface tension diminishes and the liquid-to-vapor density ratio approaches unity, and as a result, the characteristics of the bubble dynamics are expected to differ from the more explored low reduced pressure flows.

1.6. Adiabatic thermalization (i.e., the piston effect) of a near critical carbon dioxide

Heat transfer, also known as a thermalization process, is a fundamental and ubiquities phenomenon that is vital to humans, and managing it is a critical part of most modern technologies. Better and more advanced heat transfer methods are critical for human-friendly environment in outer space [83], to the development of fusion reactors for clean energy [84], and to the design of faster computers and larger datacenters [85]. An adiabatic thermalization or the piston effect, was discovered in the 1980s [86], in addition to the previously known thermalization modes of radiation, diffusion, and convection. Although the phenomenon can be explained by known thermodynamic equations [87]–[89], some tend to refer to it as a fourth mode of thermalization. Under this mode, applied heat is dissipated through acoustic waves, and the dissipation is most notable near the critical conditions where the thermophysical properties of the fluids change

significantly with temperature [90]–[92]. The piston effect was experimentally studied under microgravity conditions [93]–[95], in natural convection in enclosures with gravity [96]–[98], and was theoretically explained [99]–[106]. This effect was also reported at slightly subcritical conditions in microgravity, where a transition from a first-order phase change process (i.e., discontinuity in the primary thermodynamic properties, e.g., density) to a second-order process (i.e., discontinuity in the derivatives of thermodynamic properties, e.g., specific heat and isothermal compressibility) was observed [95], [107]. Garabos et al. [93], [94] studied bubble formation of near-critical fluids in microgravity and suggested that the effect leads to the presence of nonequilibrium liquid and gas phases, and that the liquid-vapor interface becomes unstable as the critical point is approached. Until now, experiments were conducted with near-critical, quiescent fluids using experimental rigs with a characteristic length scale of centimeters. The current study demonstrates that the piston effect is the mechanism responsible for heat transfer enhancement near the critical point [108]–[112]. Critical opalescence is used to measure the fluid's bulk temperature and compare it to the temperature rise due to the piston effect [113]. The phenomenon observed is pertinent to other fluids in similar reduced conditions due to the universality principle of critical fluid [114].

1.7. Pressure drop and Joule-Thomson effect

Flow through an orifice is encountered in copious engineering devices and is often accompanied by a large pressure drop. Typically, the fluid inside an orifice undergoes an isenthalpic process, and under certain conditions, its temperature may change — either decrease or increase. This phenomenon, known as the Joule-Thomson effect [115], constitutes the mechanisms used to throttle flow in cryogenic applications [116] and in Vapor Compression Refrigeration cycles [117] where the fluid exiting the orifice is a two-phase mixture at a low pressure (and a low temperature). The Joule-Tomson coefficient (Eq. 1) links between the pressure drop and the temperature drop according to:

$$JT_h = \left(\frac{\partial T}{\partial P}\right)_h \tag{1}$$

Like their conventional scale counterparts, micro scale flows through orifices can result in significant temperature drops when the Joule-Tomson coefficient is large. Although an orifice is a rudimentary geometry, developing an appropriate model that captures the nature of the flow can be challenging [118]. When phase change occurs, several unique conditions are present, and the orifice may be divided into two distinct regions — one for the single-phase flow and another for the two-phase flow. To calculate the two-phase flow pressure drop, the homogeneous flow model or the separated flow model can be used [119]. Alternatively, the orifice can be modeled as a capillary tube [120]–[122] — a typical approach to model the expansion process in refrigeration cycles. Capillary tubes are straight or spiral and usually have extremely high length to diameter ratio of ~ 1000 [123]. Due to its usage in refrigeration cycles, trans-critical and two-phase flows are common phenomena for such components [124], [125]. Other studies used the "short-tube orifice" approach [126]–[128] that is also adopted in refrigeration cycles for orifices with length to diameter ratios of up to ~15. Complex flow phenomenon like metastable two-phase flow and shock waves inside and outside the short-tube orifice were recorded, and therefore, the pressure drop in such cases is usually calculated using correlations [126], [127].

2. RESEARCH OBJECTIVES

- CO_2 as a coolant recently gain much interest due to its superior environmental impact compared to CFCs and HFCs. In cooling applications flow boiling plays an important role since phase transition absorbs large amounts of heat, and is therefore, an effective heat transfer mechanism. However to date, limited studies about flow boiling of CO_2 were reported where all of them were conducted in circular, macroscale geometries [1], [40]–[43],. This works seeks to address the shortcoming and reveal the thermal and hydrodynamic nature of flow boiling near critical CO_2. Thus, the following objectives were set for this effort: Produce, analyze, and compare experimental data about the onset of nucleate boiling, the heat transfer coefficient, and the critical heat flux (CHF) conditions of flow boiling of Carbon Dioxide at the micro scale near its critical condition.
- Reveal the bubble dynamics during nucleate flow boiling of near critical carbon dioxide inside a microchannel. Obtain imagery of the bubble evolution and map the flow patterns. Reveal pressure effect on bubble morphology and produce accurate bubble growth models with the obtained data.
- Reveal and explore the mechanism of heat transfer during the transition from subcritical conditions to supercritical conditions (i.e., the piston effect).
- Characterize the pressure drop of carbon dioxide through a micro-orifice and identify the relevant physics and correlations. Reveal the Joule-Thomson effect in the pertinent experimental conditions.

3. MICROFLUIDIC DEVICE AND ITS FABRICATION PROCESS

3.1. Microfluidic device description

Microfluidic device is built out of two pieces, named top and bottom, Fig. 5a. The fluid enters through the top piece inlet port, flows in the microchannel formed between the two pieces and exit, through the outlet port. On the surface of the bottom piece there is a preheater, heater and four Resistive Temperature Detectors (RTDs) that are made of metallic layers, Fig 5b. These microfabricated components enable us to apply heat and readout the microchannel wall's local temperature.

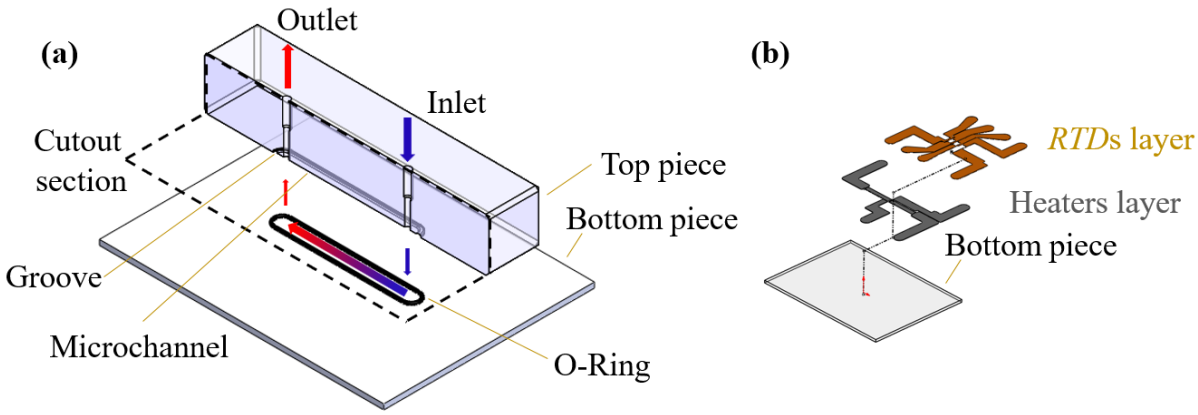

Figure 5- a-Microfluidic device design, b- bottom piece microfabricated components

Portions of this chapter previously appeared in:

A. Parahovnik, M. Asadzadeh, S. S. Vasu, and Y. Peles, "Subcooled Flow Boiling of Carbon Dioxide Near the Critical Point Inside a Microchannel," *Phys. Rev. Appl.*, vol. 14, no. 5, p. 054050, Nov. 2020.

Anatoly Parahovnik, Yoav Peles, 2022, "High pressure saturated flow boiling of CO2 at the micro scale", *International Journal of Heat and Mass Transfer*, Vol. 186.

Anatoly Parahovnik, Yoav Peles, 2022, "Bubble dynamics in a subcooled flow boiling of near-critical carbon dioxide", *International Journal of Heat and Mass Transfer*, Vol. 183, Part C.

Anatoly Parahovnik, Yoav Peles, 2022, "Heat transfer mode shift to adiabatic thermalization in near-critical carbon dioxide with flow boiling in a microchannel", *International Journal of Heat and Mass Transfer*, Vol. TBD.

A. Parahovnik, P. Ahmed, Y. Peles, "Pressure drop and Joule-Thomson effect in a micro orifice with trans critical carbon dioxide flow", *Journal of supercritical fluids*, under review.

Top pieces are made of transparent material to enable optical access. They were fabricated using material removal techniques by Mindrum Precision®, a vendor that specialized in production of delicate optical components. The outer surfaces and the upper wall of the microchannels were polished to enhance optical clarity and to minimize the leakage between top and bottom pieces. Top pieces have two microchannel configurations that differ in the channel's height, which are 0.1 mm and 0.2 mm. The pieces with a channel of 0.1 mm height have additional peripheral groove to accommodate an O-ring in case of substantial leakage during the operation. The groove's height is 0.2 mm, the same as the channel's height for some of the top pieces' configurations, and therefore the groove blends with the channel's upper wall for these pieces.

The heater was placed in the optical window section as far as possible downstream from the inlet in order to be located in a fully developed hydrodynamic regime. To control the thermal boundary layer and in some cases to be able to adjust the inlet temperature a preheater was integrated upstream to the heater. RTD '0' was placed between the heater and the preheater to better understand the thermal leakage of the heater. RTDs '1', '2' and '3' were spaced on top of the heater to be seen through the optical window, Fig. 6.

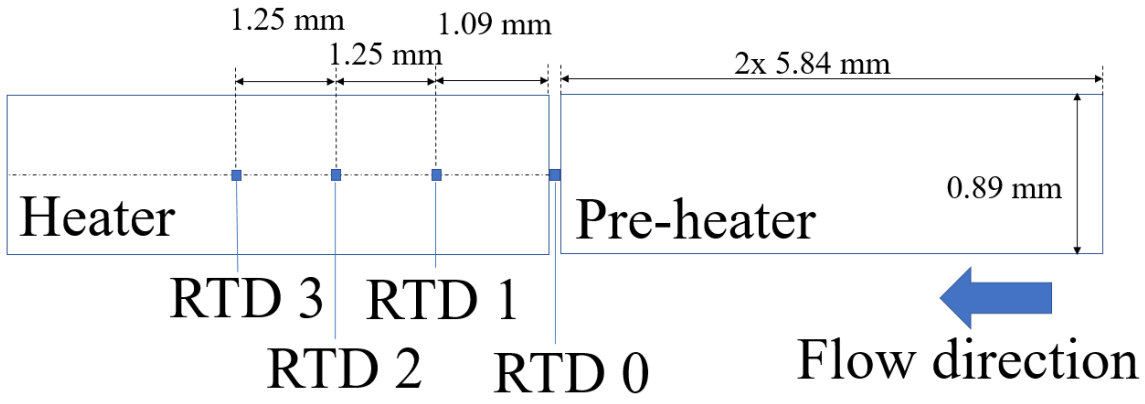

Figure 6- Components layout on top of the bottom piece

The microfabrication recipe is presented in detail in the Appendix.

3.2. Top piece fabrication

The top pieces contain the volume of the microchannels and were produced in three configurations:

0.1 mm-height microchannel with cavity for O-ring (although the O-ring consequently wasn't used), 0.2 mm-height microchannel without an O-Ring cavity, and a microchannel with an integrated micro-orifice, the fabrication drawings of the parts are in Appendix C. Figure 7, present schematic cross sections of the microchannels and the micro-orifice, however the rounds at the microchannle's corners were significantly larger (due to the limiting geometry of the tooling). To account for it the hydraulic diameters were calculated using the dedicated equation (i.e., 4× area / perimeter), where the values were obtained using a CAD model. The hydraulic diameters of the channels were 0.294 mm, 0.4 mm, 0.296 mm, and 0.081 mm for 0.1 mm-height microchannel, 0.2 mm-height microchannel, the microchannel with embedded orifice, and the micro-orifice, respectively.

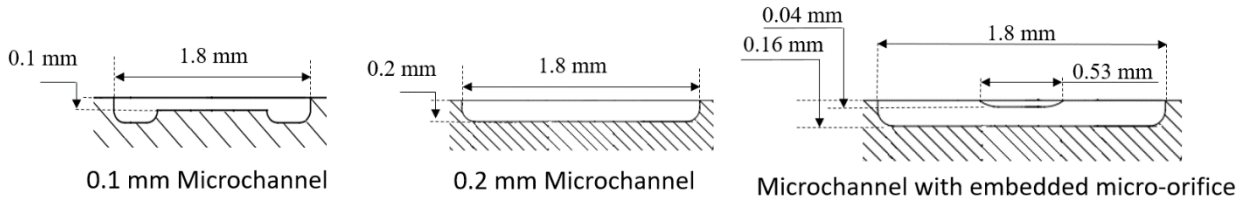

Figure 7- Sketches of the microchannles' and micro-orifice's cross sections

Figure 8 shows the relative location of the micro-orifice to the RTDs and the heaters. As can be seen RTD 0 was located inside the orifice close to the exit, and the rest of the RTDs located inside the microchannel on top of the heater, the ratio of the distance from the micro-orifice's exit to hydraulic diameter were 3.2, 7.4, and 11.6 for RTD1, RTD2, and RTD3, respectively.

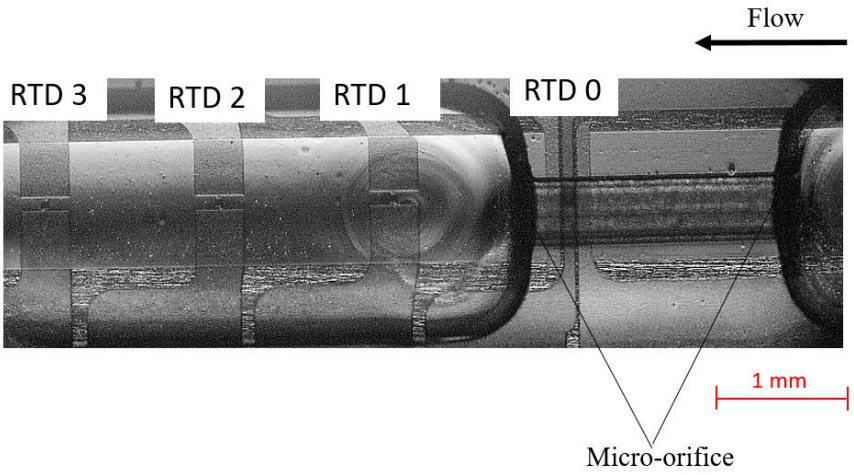

Figure 8- micro-orifice positioning. RTD0 was located inside the micro-orifice close to its exit. The length to hydraulic diameter ration for RTD1, RTD2, and RTD3 were 3.2,7.4, and 11.6 respectively.

The production drawings of the top pieces are presented in detail in the Appendix.

3.3. Bottom piece microfabrication process

The microfabricated components on the bottom piece were preheater, heater, RTDs and vias, the former connects the components to the sampling rig, Fig. 9.

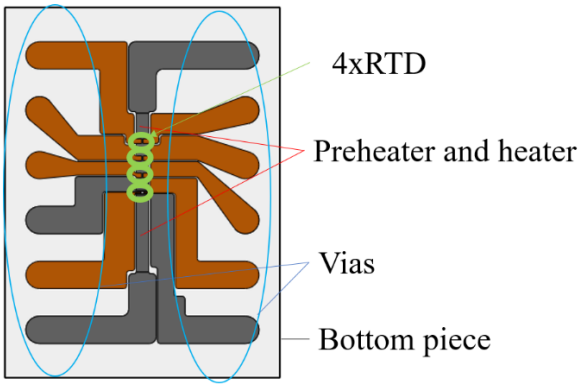

Figure 9- Micro components on the bottom piece

The first layer to be fabricated is the preheater and heater layer, the metals are sputtered simultaneously [129], then using the photolithographic process the required pattern is transferred to the wafer and the access

aluminum is removed using wet aluminum etchant [130]. The third step using ion milling tool [131] the platinum and aluminum metals are shaped. Finally, the heater layer is sealed with the silicon oxide layer which is deposited using the PECVD process [132]. The visible pattern in figure 10a is the preheater heater layer with its' vias, there are 6 similar patterns that indicate that 6 microdevices are fabricated on a single wafer. At the next steps, the deposition and removal of metals are repeated but with different patterns to form the RTDs and the vias, Fig. 10b. Each layer is a stack of 3 metals, 7 nm thick titanium, 30 nm thick platinum and 1 mm thick aluminum. The titanium is used as an adhesive, the platinum is the heater or the RTDs and aluminum is used for the vias. The metals change their resistance as a function of temperature $R = \rho(T) \cdot \frac{A}{l}$ where R is the electrical resistance, ρ is the metal resistivity, A is the heater cross section in the flow direction of the current, and l is the distance the current travels through the metal. Joule heating is facilitated through the layer according to $p = \frac{V^2}{R}$ where p is the power [W], V is the voltage [V] and R is the heater layer electrical resistance. The relative thickness of aluminum reduces vias electric resistance and make it tolerant to scratches that are caused by the probe tips, which come in intimate contact with the vias. The metallic layers are insulated and covered by a silicon oxide layer; the upper silicone oxide deposition is polished using CMP process to enable sealing of the microchannel. At the next step the insulating silicon oxide is etched from edges of the vias to enable electrical contact between the microfluidic device and the experimental setup. Finally, the bottom pieces are cutout from the wafer. During the post fabrication inspection, the preheater and heater resistance yields electrical resistance of 67 Ω each, while the RTDs' resistance is about 2.5 kΩ. The surface roughness measured with a profilometer [133] was 150-500 nm. Detailed fabrication sequence is located in appendix A.

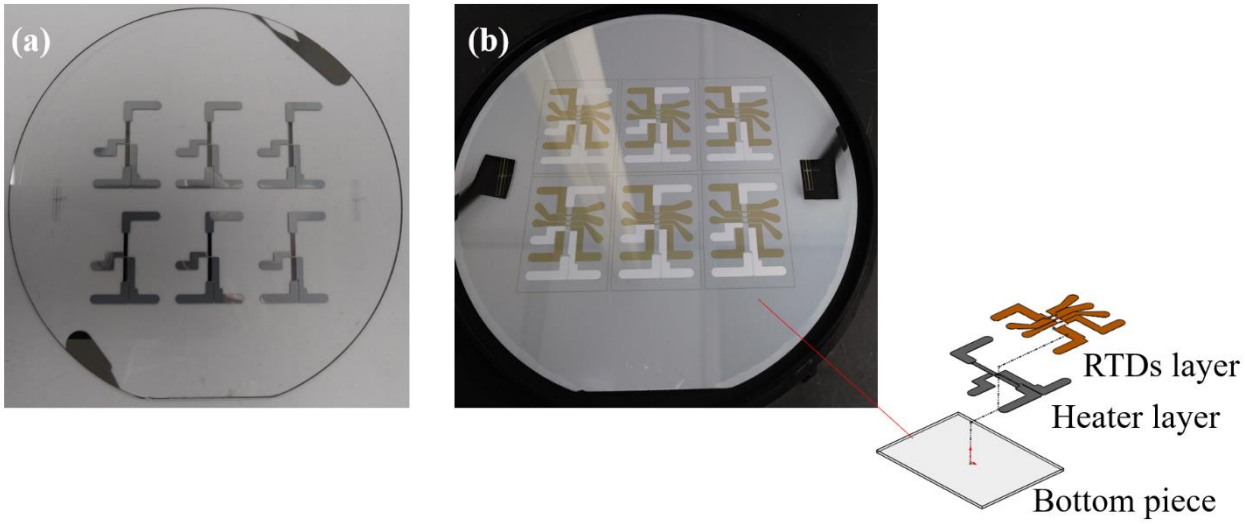

Figure 10- a-Preheater and heater layer with its vias, b- RTD layer on top of the preheater and heater layer before the aluminum etching

3.4. Materials selection and structural Analysis

The considered materials had to be compatible with microfabrication processes, to have low thermal conductivity coefficient, to be optically transparent and to withstand the required operational pressure, Table 2. Silicon is the most common and suitable for a variety of microfabrication processes, and it is also bondable to borosilicate glass in a process that leads to a sealed microfluidic channel. Due to the metallic layers deposited on the bottom piece there is no viable option to seal the microchannel using anodic bonding process. Another disadvantage of silicon for our application was its high thermal conductivity that would lead to averaged temperature readings due to substantial heat conduction through the silicon. Alternative material is sapphire; it has moderate thermal conductivity and superior mechanical strength; however, it is extremely expensive and relatively rare compared to borosilicate glass and fused silica which are more prospective candidates to be used as a structural material for the microfluidic device. Finally, the specific material was chosen after detailed structural analysis, which is discussed in the following section.

Table 2- Considered materials for microfluidic device construction

Mechanical Properties	**Silicon**	**Borosilicate glass**	**Fused Silica (Quartz)**	**Sapphire**	**Stainless steel 316L**	**Delrin**
Density [kg/mm^3]	2,328	2,200	2,648	3,980	8,000	1,420
Yield stress σ_y [MPa]	340	25	48	275	205	69
Youngs modulus E [GPa]	168	64	72	345	193	3.1
Poisson's ratio υ [1]	0.278	0.2	0.18	0.29	0.26	0.35
Thermal conductivity κ [W/m^{2}K]	148	1.4	1.4	34.6	14.7	0.37
Mohs Hardness	7	5	7	9	5	1

Since the typical operational pressure of the microdevice was about 7.4 MPa, a structural analysis was performed to make sure that the microdevice will tolerate the required pressure. The influence of pressure on the top and bottom pieces were analyzed and eventually guidelines for package design were deduced (The package is described in detailed in the next section).

In the structural model the required operational pressure of 7.4 MPa was applied in the designated microchannel areas, inlet and outlet bores, Fig 11a. The supported area was theoretically assigned at the outer bend of the external surfaces, Fig 11b. The mesh contained 28,000 nodes and 15,600 elements, which is the largest allowable grid size for the academic version of Ansys Workbench® software, while the assigned material was borosilicate glass which was the preferred structural material at the initial stage. Because the microchannel will function as micro pressure vessel, safety factor of at least 3.3-3.5 should be maintained for the required operational pressure, as recommended by ASME® pressure vessel design standard [134]. The analysis produced maximal Von-mises stress of 10.5 MPa and strain of 0.01 % in the top piece and 446 MPa and 84 % in the bottom piece.

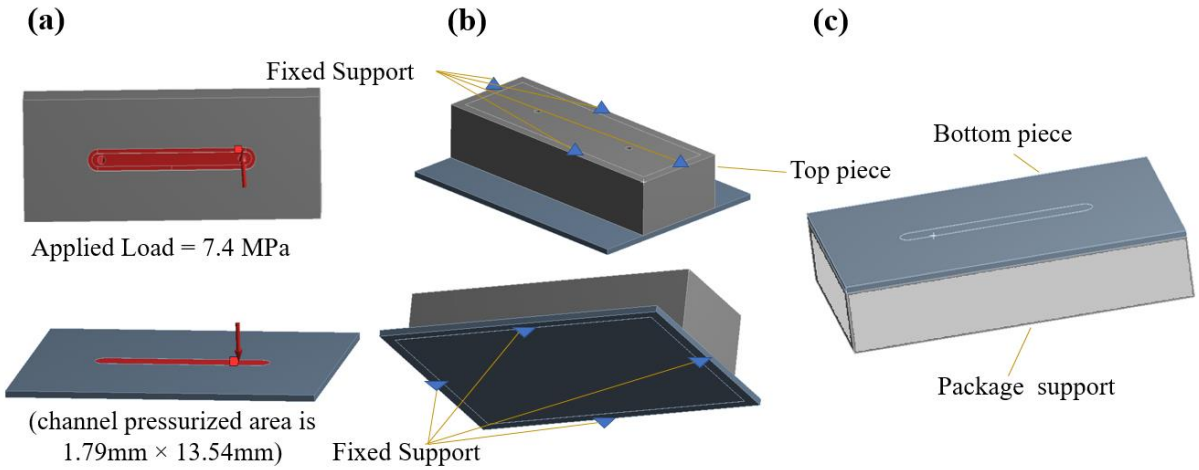

Figure 11- loads and supports for the structural analysis of the microfluidic device

The results lead to the conclusion that the top piece can withstand the required conditions and therefore this design is feasible. However, if the top piece was made of borosilicate glass, it would not fulfill the safety factor requirement. For the bottom piece there was a geometrical restriction on its thickness, as part of its microfabrication process the bottom piece must undergo Chemical Mechanical Polishing (CMP). The available machine for such process could process only 0.5 mm thickness wafers, therefore the piece thickness was fixed to 0.5 mm. This restriction led to the conclusion that the bottom piece must be fully supported by the package, therefore, the package as also integrated into the analysis, Fig. 11c. The potential materials for the package were stainless steel 316L and Delrin Acetal that is a relatively strong plastic.

Analysis outcomes are explained using the following parameters: maximal stresses (σ_{max}) strain (ε) and displacement (δ), table 3. The developed stresses and strains within the package were within the acceptable range. Resemblance in the mechanical properties of borosilicate glass and fused silica leads to a similarity in the strain and stress that developed in the bottom piece, the obtained stresses are 2 MPa and 20 MPa when supported by steel and Delrin consistently. The developed strains are $2.8e^{-3}$ and $2.5e^{-3}$ for borosilicate glass and fused silica supported by steel respectively and the strains are $3.4e^{-2}$ and $3.3e^{-2}$ for borosilicate glass and fused silica supported by Delrin respectively. Since Delrin has lower Young modulus the developed stresses in the bottom piece combined with it were significantly higher, the same hold true for

the strain levels, that reach the maximal allowable value of 0.04 % [135]. Therefore, stainless steel was chosen to be a structural material which kept the strain and stress values of the bottom piece in an acceptable range.

Table 3-Structural analysis results

	Borosilicate glass			**Fused silica**		
	σ_{max} MPa	ε %	$\delta\ \mu m$	σ_{max} MPa	ε %	$\delta\ \mu m$
Bottom piece with steel support	2	$2.8e^{-3}$	0.13	2	$2.5e^{-3}$	0.12
Steel Package	-6	$1.8e^{-3}$	0.082	-5.9	$1.7e^{-3}$	0.082
Bottom piece with Delrin support	20	$3.4e^{-2}$	3.8	20	$3.3e^{-2}$	3.8
Delrin Package	-1.4	$5.2e^{-2}$	3.8	-1.4	$5.1e^{-2}$	3.8

Material surface hardness is an issue that also must be considered. Mohs hardness of stainless steel is 5, Table 3, and in a contact with softer material can promote a failure, therefore, the reasonable way of action is to choose fused silica as structural material for the microdevice because its superior hardness 7 in Mohs scale. Moreover, fused silica has higher yield stress which lead to a safety factor of 4.57 compared to 2.38 for borosilicate glass for the top piece. To conclude, following structural analysis, the microfluidic device was made of fused silica and the package out of stainless steel 316L.

4. EXPERIMENTAL SETUP

4.1. Pneumatic setup

The required performance of the experimental setup were pressure range of 4.8-14 MPa, inlet temperature of 295-350 K, and mass flow rate up to 1 gr/sec, which corresponds to mass fluxes of up to 7400 kg/m^{2}sec (Eventually the highest mass flux used in the current research was about 3000 kg/m^{2}sec).

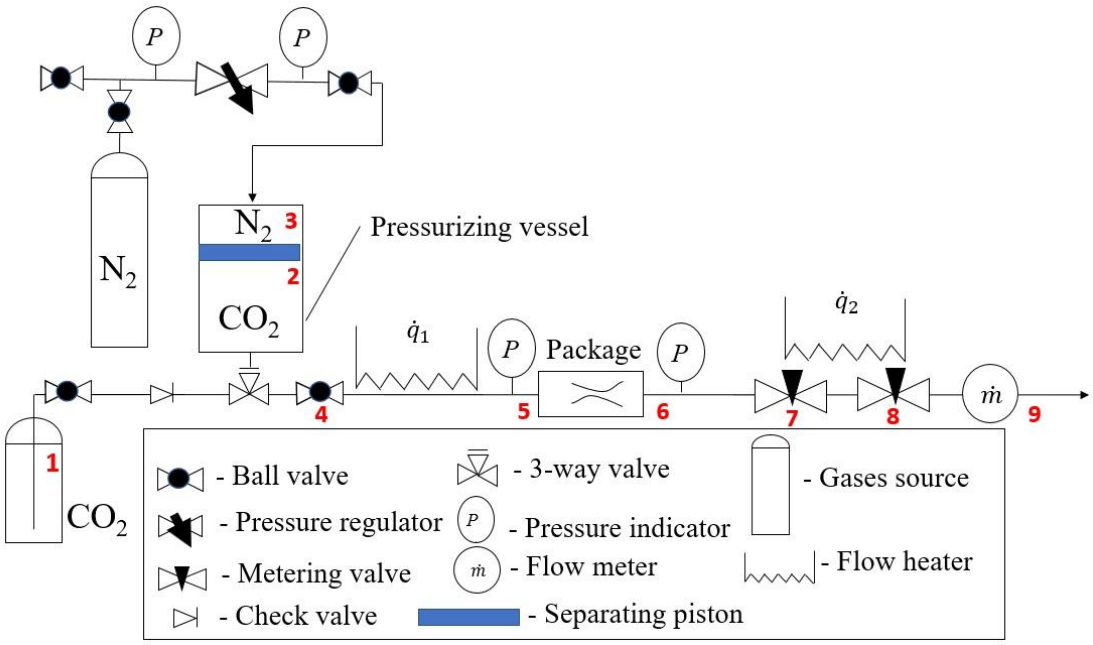

Figure 12-Sketch of the pneumatic setup of the experimental rig [64]

Portions of this chapter previously appeared in:

A. Parahovnik, M. Asadzadeh, S. S. Vasu, and Y. Peles, "Subcooled Flow Boiling of Carbon Dioxide Near the Critical Point Inside a Microchannel," *Phys. Rev. Appl.*, vol. 14, no. 5, p. 054050, Nov. 2020.

Anatoly Parahovnik, Yoav Peles, 2022, "High pressure saturated flow boiling of CO2 at the micro scale", *International Journal of Heat and Mass Transfer*, Vol. 186.

Anatoly Parahovnik, Yoav Peles, 2022, "Bubble dynamics in a subcooled flow boiling of near-critical carbon dioxide", *International Journal of Heat and Mass Transfer*, Vol. 183, Part C.

Anatoly Parahovnik, Yoav Peles, 2022, "Heat transfer mode shift to adiabatic thermalization in near-critical carbon dioxide with flow boiling in a microchannel", *International Journal of Heat and Mass Transfer*, Vol. TBD.

A. Parahovnik, P. Ahmed, Y. Peles, "Pressure drop and Joule-Thomson effect in a micro orifice with trans critical carbon dioxide flow", *Journal of supercritical fluids*, under review.

Both close and open loop configurations were considered, however, we couldn't locate a pump or compressor that will be able to circulate such low flow rate at a reasonable price. Therefore, an open loop experimental setup was constructed, Fig 12. CO_2 was delivered from a high-pressure tank at state 1 to a pressurizing vessel at state 2 through a filter, a check valve, and a 3-way valve. This vessel with a separating piston allowed to control the CO_2 pressure before it entered the microchannel. The pressure was regulated using nitrogen gas that resided on the piston's other side (State 3), Fig. 13. When the CO_2 at state 3 reached the desired pressure, the 3-way valve and the ball valve (State 4) were opened to allow flow through a preheater ($\dot{q}_1$) before entering the microchannel through the package. Pressures at states 5 and 6 were measured using inlet and exit transducers made by Omega Engineering® (Model PX309-5KG5V). The exit pressure and the mass flow rate were controlled by two metering values (states 7 and 8). The metering valves had heating elements to prevent the solidification of CO_2 due to the Joule Thomson (JT) effect. Before leaving the experimental setup into the atmospheric air, the flow rate was measured using a mass flow meter (state 9) made by Alicat® (Model M-20SLPM-D®), Fig. 14.

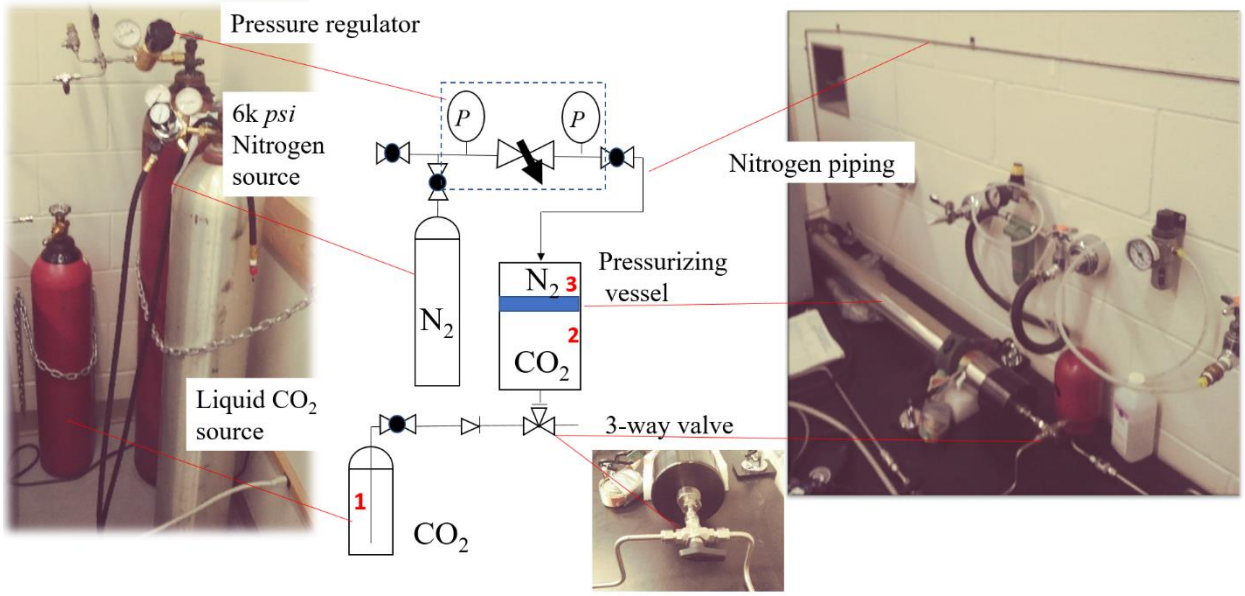

Figure 13-realization of the pressurizing principle of the experimental rig.

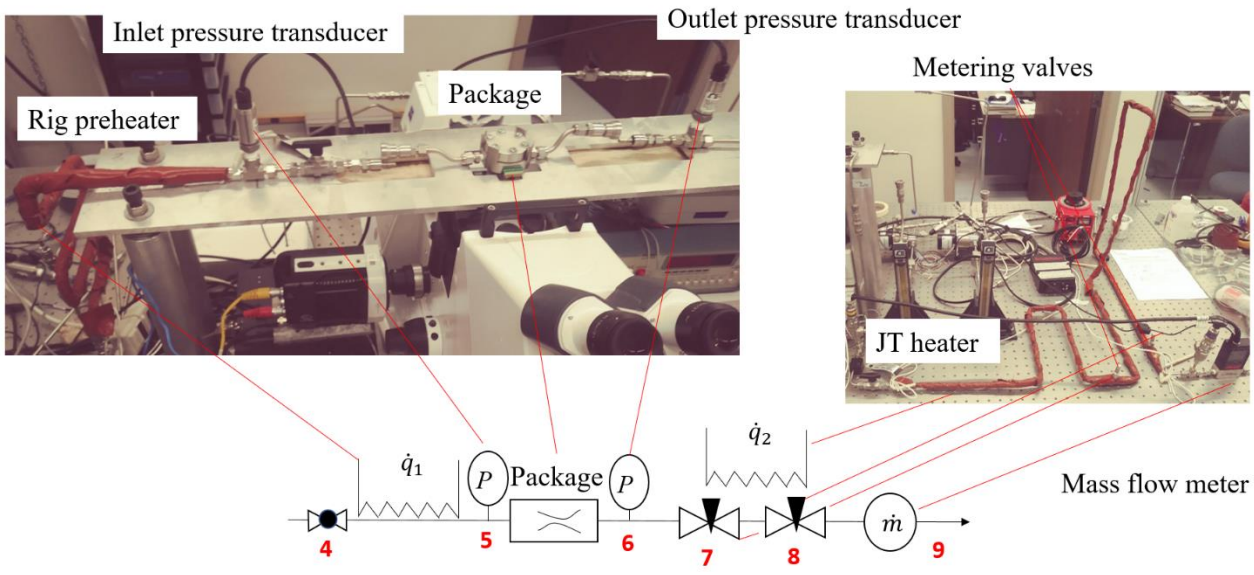

Figure 14- Experimental rig with package metering valves and JT heater

4.2. Package

As was presented in the mechanical analysis, the package must support the bottom piece and to connect the microdevice to the experimental setup.

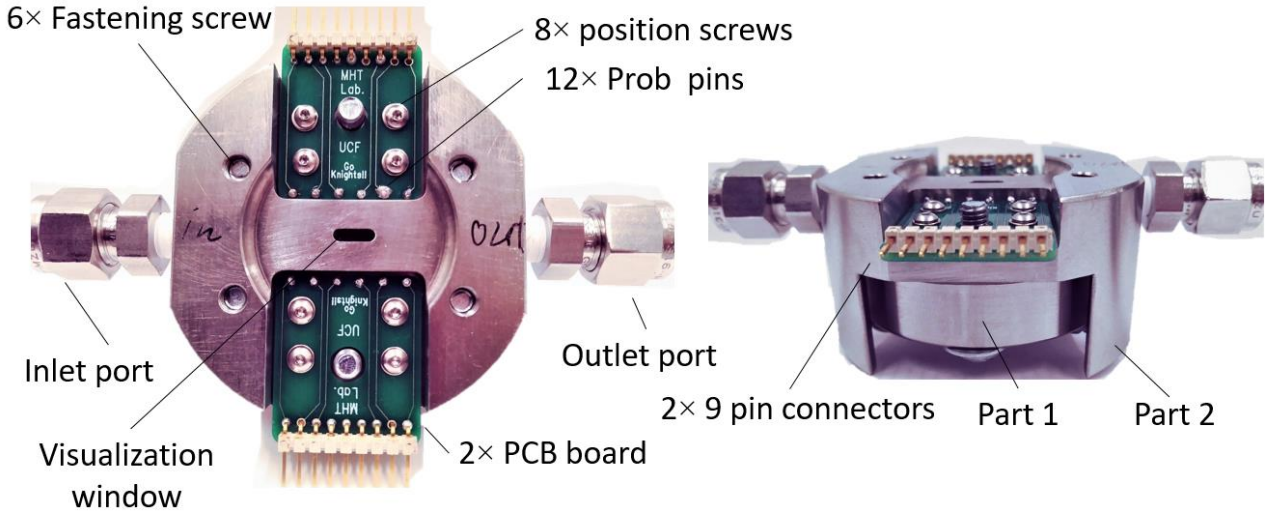

Figure 15- top and side view of the microfluidic device package [64]

The package consists of two main parts, part one is a mechanical support for the bottom piece and a relatively simple thick cylinder that is fastened with six screws to part two and presses the top and bottom pieces together. The roles of part two are more complicated, Fig 15. Part two has a flow inlet and flow outlet, an optical window for visualization, and it houses two PCB boards that contain probe pins that apply the heat flux and samples the temperatures. Following the guidelines that were described in 'Materials selection and structural Analysis' section, a mechanical simulation of the package was performed to evaluate whether package deformation due to screw fastening can fracture the microfluidic device. Following the analysis, part 1 was thickened to minimize the bending strains that were expected due to the elevated operational pressure, Fig. 15

4.3. Sampling setup

The sampling setup consisted of a microscope, a high-speed camera (Phantom® MIRO 310M®), a power supply (Kysight®, E3645A®), multimeters (Agilent®, 34410A®), a breakout board, and sampling hardware (National Instruments®, SCXI 1000®, and DAQ 9178®), which were connected to a computer (see Figure 2 Right). The sampling setup recorded synchronized images of the flow with temperature readings within the microchannel and applied the needed heat load to the microfluidic device, Figure 16.

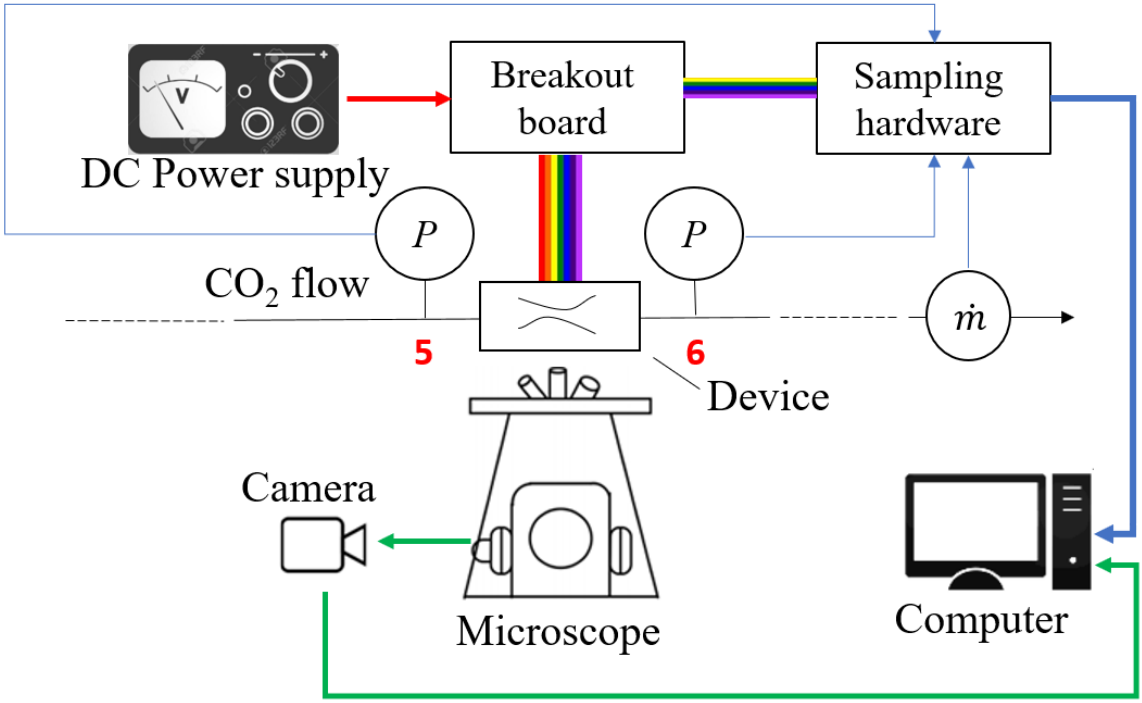

Figure 16- Sampling setup of the experimental rig

4.4. Uncertainty evaluation of the experimental setup

The excess temperature, ΔT_{sat}, and the associated heat transfer coefficient:

$$\Delta T_{sat} = T_w - T_{sat} \tag{2a}$$

$$HTC = \frac{q - q_{loss}}{\Delta T_{sat}} \tag{2b}$$

Where q and q_{loss} were the heat load and heat loss, respectively; And T_w and T_{sat} were the wall and saturation temperatures, correspondingly.

Before conducting experiments, all RTDs were placed in an oven and calibrated in a temperature range of 297 K to 373 K. A T-type thermocouple was used to measure the device temperature during the calibration process to relate the RTDs electrical resistance to their respective temperatures. A linear curve fit (of R^2 of about 0.9999) between the resistances and temperatures was established and used during data processing.

The channel was vacuumed to assess the heat losses. The heat was then applied to the heater, and the heat losses were estimated using a thermal resistance method according to:

$$q_{loss} = (T_w - T_\infty)/R_{thermal} \quad (3)$$

Where T_w -T_∞ is the temperature difference between the wall (T_w) and the ambient temperature (T_∞). A thermal resistance, $R_{thermal}$, of 3.45 K/W, was found to predict the heat losses best. For each experimental data point, the heat loss was calculated and subtracted from the heat load.

Experimental uncertainties were estimated using the propagation of uncertainty analysis [136]. The temperature uncertainty was estimated to be ±0.33 K, and the pressure uncertainty was estimated to be ±0.017 MPa. The mass flow rate's uncertainty was estimated to be ±0.1 slpm, leading to uncertainty of ±10 kg/m^{2}s in the mass flux. For the subcooled and saturated flow boiling experiments the uncertainty, the uncertainty of the Boiling number was estimated to be ±10 %.

For the bubble dynamics section, the velocities and the bubbles' sizes were measured with analysis tools embedded in the camera's operational software (Phantom® CV 3.4). The diameter of the bubbles was measured using a ruler function in the camera's software with an accuracy of 1.9 μm/pixel and a time difference, Δt, between frames of 135.12 μs. The diameter of the surveyed bubbles was manually measured and recorded. Concurrently, the bubble position was also recorded. The accumulation of the uncertainties over the bubble position resulted in a total uncertainty of ±23% of the nominal velocity. After the measurement, the velocity was derived through the distance the bubble traveled for a given number of frames (i.e., $\Delta x/\Delta t$). The data reduction process yielded the diameter and velocity of the bubble as a function of time and location. The shadowed bubbles were sampled at the inception line and were traced until leaving the optical window.

For the micro-orifice analysis, the pressure drop over the ball-valve and the quick connectors were evaluated using the discharge coefficient provided by the manufacturer (Swagelok®), and the pressure drops in the tubing, package, and the microchannel were evaluated using established pressure drop

equations [137], where the friction factor was evaluated by the Colebrook equation [138], [139]. It was found that the average mean loss of all components excluding the orifice was 3.5% of the total measured pressure drop, which was subtracted from the measured values.

5. THEORETICAL MODELS

5.1. The onset of nucleate boiling

The following three established models were considered to supplement the experiments: Hsu's model [44], Davis and Anderson's model [45] with and without adjustments, and an experimentally based correlation proposed by Lienhard [46].

Two adjustments to Davis and Anderson's model were introduced, a generalized gas equation of state, Pv=ZRT, was used instead of the ideal gas law. The Kelvin equation [13] and the Clausius-Clapeyron equation were used to reformulate the original model. As a result, the following two constants were altered to:

$$a = a_{GEOS} = \frac{2\cdot\sigma}{P_l}\cdot\left(1-\frac{z_l}{z_g}\right) \text{ and } c_4 = c_{4_{GEOS}} = \frac{R_{CO_2}\cdot(z_l-z_g)\cdot T_{sat}}{h_{fg}} \quad (4)$$

Where Z_l and Z_g are the compressibility factors of the liquid and gas phases, respectively, σ is the surface tension, P_l is the liquid pressure, and h_{fg} is the latent heat of vaporization. The second change included the integration of the boundary layer theory [140], which resulted in a modified temperature profile that produced the following equations:

$$\frac{T_w-T_l}{T_w-T_\infty} = \left(\frac{y}{2\cdot\delta_T}\right)\cdot\left(3-\left(\frac{y}{\delta_T}\right)^2\right) \quad (5)$$

Portions of this chapter previously appeared in:

A. Parahovnik, M. Asadzadeh, S. S. Vasu, and Y. Peles, "Subcooled Flow Boiling of Carbon Dioxide Near the Critical Point Inside a Microchannel," *Phys. Rev. Appl.*, vol. 14, no. 5, p. 054050, Nov. 2020.

Anatoly Parahovnik, Yoav Peles, 2022, "High pressure saturated flow boiling of CO2 at the micro scale", *International Journal of Heat and Mass Transfer*, Vol. 186.

Anatoly Parahovnik, Yoav Peles, 2022, "Bubble dynamics in a subcooled flow boiling of near-critical carbon dioxide", *International Journal of Heat and Mass Transfer*, Vol. 183, Part C.

Anatoly Parahovnik, Yoav Peles, 2022, "Heat transfer mode shift to adiabatic thermalization in near-critical carbon dioxide with flow boiling in a microchannel", *International Journal of Heat and Mass Transfer*, Vol. TBD.

A. Parahovnik, P. Ahmed, Y. Peles, "Pressure drop and Joule-Thomson effect in a micro orifice with trans critical carbon dioxide flow", *Journal of supercritical fluids*, under review.

Where for the calculation of the thermal boundary layer, δ_T, Equations 6-8 were used.

$$\delta_{hyd} = 4.92 \cdot x \cdot R_{e_x}^{-\frac{1}{2}} \tag{6}$$

$$\delta_{hyd} = 0.37 \cdot x \cdot R_{e_x}^{-\frac{1}{5}} \tag{7}$$

$$\Delta = 0.976 \cdot P_r^{-\frac{1}{3}} \cdot \left[1 - \left(1 - \frac{x_0}{x}\right)^{\frac{3}{4}}\right]^{\frac{1}{3}} \tag{8a}$$

$$\delta_T = \Delta \cdot \delta_{hyd} \tag{8b}$$

Where δ_{hyd} is the hydrodynamic boundary layer thickness, x is the distance from the inlet, Re_x is the local Reynolds number, x_0 is the unheated distance from the entrance, y is the perpendicular distance from the wall, and Δ is the ratio between the thermal and the hydrodynamic boundary layers.

5.2. Heat transfer coefficient of subcooled flow boiling

The heat transfer correlations for subcooled flow are in some form a simplified version of saturated flow boiling correlations, where in subcooled case there is a single boiling pattern (i.e., nucleate boiling) and the physical potential that drives the heat is the subcooled degree of the fluid (i.e., T_{sat}-T_b).

The Shah's correlation [47] for low subcooled conditions (i.e., $(T_{sat}-T_b)/(T_w-T_{sat}) < 2$) is divided into two dimensionless parameters:

$$\psi = 230 \cdot B_o^{0.5} \quad , B_o > 0.3 \times 10^{-4} \tag{9a}$$

$$\psi = 1 + 46 \cdot B_o^{0.5} \quad , B_o < 0.3 \times 10^{-4} \tag{9b}$$

$$\psi = \frac{q}{(T_w - T_{sat}) \cdot h_L}, B_o = \frac{q}{G \cdot h_{fg}}$$

Where B_o is the boiling number and ψ is a dimensionless heat transfer coefficient ratio that is normalized using the Dittus-Boelter correlation [141] for single-phase heat transfer coefficient, h_L, and T_b is the fluid bulk temperature. For large subcooled temperatures (i.e., $(T_{sat}-T_b)/(T_w-T_{sat}) \geq 2$), $(T_{sat}-T_b)/(T_w-T_{sat})$ is added to Equations 9a and 9b as follows:

$$\psi = 230 \cdot B_o^{0.5} + \frac{T_{sat}-T_b}{T_w-T_{sat}} \quad , B_o > 0.3 \times 10^{-4} \tag{9c}$$

$$\psi = 1 + 46 \cdot B_o^{0.5} + \frac{T_{sat}-T_b}{T_w-T_{sat}} \quad , B_o < 0.3 \times 10^{-4} \tag{9d}$$

The Kandlikar's correlation [142] for subcooled flow boiling is as follows:

$$\psi = 1058 \cdot B_o^{0.7} \cdot F_{fl} \tag{10}$$

The Gnilinski [143] correlation is used to calculate the single-phase heat transfer coefficient, and the Bo number is defined in the same manner as in the Shah's correlation. The coefficient, F_{fl}, depends on the type of fluid, and for CO_2, Ducoulombier [144] stated that a value of 2.1 should be used.

Finally, the Cheng's correlation [145] relates the heat transfer coefficient to the reduced pressure, the molar mass, and the heat flux according to:

$$h_{nbc} = 131 \cdot P_r^{-0.0063}(-\log_{10} P_r)^{-0.55} \cdot M^{-0.55} \cdot q''^{0.58} \tag{11}$$

$$\psi = \frac{h_{nbC}}{h_L} \tag{12}$$

Where P_r is the reduced pressure, and M is the molar mass.

5.3. Heat transfer coefficient for saturated flow boiling

Convective heat transfer coefficient for saturated flow boiling is a complicated physical phenomenon, in this study three correlations (the extended forms of the correlations used in subcooled section) were compared with the experimental results, the correlations are summarized in table 4.

Table 4- Established correlations for HTC and associate mean average errors [146]

Correlation	Fluid	Conditions	Formula	MAE
Kandlikar [147]	Water R-11, R-12, R-13B1 R-22, R-113, R-114, R-152, Neon, Nitrogen	Vertical and horizontal tubes *D*=4-25 mm *G*=13 - 8179 kg/m^{2}s *P*= 0.06 - 6.42 MPa *x*=0 - 0.987 q''=3e^{-4} – 2.28 W/m^2	$\frac{h_{TP}}{h_l} = C_1 \cdot Co^{C_2} \cdot (25 \cdot Fr_{lo})^{C_5} + C_3 \cdot Bo^{C_4} \cdot F_{fl}$ $h_l = 0.023 \cdot Re_l^{0.8} \cdot \mathrm{Pr}_l^{0.4} \cdot \left(\frac{\kappa_l}{D}\right)$ $F_{fl} = 2.1$, for CO_2 Co< 0.65 Co> 0.65 C_1 1.136 0.6683 C_2 -0.9 -0.2 C_3 667.2 1058 C_4 0.7 0.7 C_5 0.3 0.3 For Fr_{lo} > 0.04 C_5=0. Where: $Co = \left(\frac{1}{\mathbf{x}} - 1\right)^{0.8} \cdot \left(\frac{\rho_v}{\rho_l}\right)^{0.5}$, $Bo = \frac{q''}{G \cdot h_{fg}}$, $\mathrm{Re_l} = \frac{G \cdot D \cdot (1-x)}{\mu_l}$, and $Fr_{lo} = \frac{G^2}{\rho_l^2 \cdot g \cdot D}$	15.9% for water 18.8% for other refrigerants
Shah. [148], [149]	Water, R-11,R12, R-22, R-113, and Cyclo-hexan	Vertical and horizontal D=6-25.4 mm G=12.2 – 868 kg/m^{2}s P= 0 – 17.2 MPa x=0 - 1 q″=1300 – 790,000 W/m^2	For Fr_{lo} >= 0.04 N=Co For Fr_{lo} < 0.04 N=$0.38 \cdot Fr_{lo}^{-0.3} \cdot Co$ For N>1 $\frac{h_{TP}}{h_{l\ \mathrm{nb}}} = 230 \cdot Bo^{0.5}, Bo > 0.3e^{-4}$ $\frac{h_{TP}}{h_{l\ \mathrm{nb}}} = 1 + 46 \cdot Bo^{0.5}, Bo < 0.3e^{-4}$ For 0.1<N<= 1 $\frac{h_{TP}}{h_{l\ \mathrm{bs}}} = \mathrm{F} \cdot Bo^{0.5} \cdot e^{2.74 \cdot N^{-0.1}}$ For N< 0.1 $\frac{h_{TP}}{h_{l\ \mathrm{bs}}} = \mathrm{F} \cdot Bo^{0.5} \cdot e^{2.47 \cdot N^{-0.15}}$ For Bo>= 11e^{-4}, F=14.7 For Bo< 11e^{-4}, F=15.43 For all N $\frac{h_{TP}}{h_{l\ \mathrm{cb}}} = 1.8/N^{0.8}$ Finally: $\frac{h_{TP}}{h_l} = \max\{\frac{h_{TP}}{h_{l\ \mathrm{nb}}}, \frac{h_{TP}}{h_{l\ \mathrm{cb}}}, \frac{h_{TP}}{h_{l\ \mathrm{bs}}}\}$ Where h_l, Co, Bo, and Fr_{lo} are the same to Kandlikar's correlation	14%
Cheng et al. [1], [40], [43]	CO_2	Horizontal tubes *D*=0.6 - 10 mm *G*=50 – 1500 kg/m^{2}s *P*= 1.43 – 6.33 MPa *x*=0 - 1	**<u>For bubbly flow regime (x < 0.18)</u>** $\varepsilon = (x/\rho_v)\left[\left(1 + 0.12 \cdot (1-x)\right) \cdot \left(\frac{x}{\rho_v} + \left(\frac{1-x}{\rho_l}\right)\right)\right.$	71.4% of the database were within ±30% margin

Correlation	Fluid	Conditions	Formula	MAE
		q''=1800 – 46000 W/m^2	$+\frac{1.18\cdot(1-x)\cdot[g\cdot\sigma\cdot(\rho_l-\rho_v)]^{\frac{1}{4}}}{G\cdot\rho_l^{\frac{1}{2}}}]^{-1}$	
			$A_L = A\cdot(1-\varepsilon)$	
			$\delta = \frac{D}{2} - \sqrt{\left(\frac{D}{2}\right)^2 - (2\cdot A_L)/(2\cdot\pi-\theta_{dry})}$ where θ_{dry} is 0 for bubbly flow regime.	
			$Re_\delta = \frac{4\cdot G\cdot(1-x)\cdot\delta}{\mu_l\cdot(1-\varepsilon)}$	
			$h_{nb} = 131\cdot P_r^{-0.0063}\cdot(-\log_{10}P_r)^{-0.55}\cdot M^{-0.5}\cdot q''^{0.58}$	
			$h_{cb} = 0.0133\cdot Re_\delta^{0.69}\cdot Pr_l^{0.4}\cdot\frac{\kappa_l}{\delta}$	
			$h_{wet} = ((S\cdot h_{nb})^3 + h_{cb}^3)^{\frac{1}{3}}$	
			$h_{TP} = \frac{\theta_{dry}\cdot h_v + (2\pi-\theta_{dry})\cdot h_{wet}}{2\pi}$	
			$h_v = 0.023\cdot Re_v^{0.8}\cdot Pr_v^{0.4}\cdot\frac{\kappa_v}{D}$	
			$Re_v = \frac{G\cdot x\cdot D}{\mu_v\cdot\varepsilon}$	
			<u>For annular flow regime (0.35> x > 0.18)</u>	
			$\varepsilon = (x/\rho_v)[(1+0.12\cdot(1-x))\cdot\left(\frac{x}{\rho_v}+\left(\frac{(1-x)}{\rho_l}\right)\right)$ $+\frac{1.18\cdot(1-x)\cdot[g\cdot\sigma\cdot(\rho_l-\rho_v)]^{\frac{1}{4}}}{G\cdot\rho_l^{\frac{1}{2}}}]^{-1}$	
			$A_L = A\cdot(1-\varepsilon)$	
			$\delta = \frac{D}{2} - \sqrt{\left(\frac{D}{2}\right)^2 - (2\cdot A_L)/(2\cdot\pi-\theta_{dry})}$ where θ_{dry} is 0 for bubbly flow regime.	
			$Re_\delta = \frac{4\cdot G\cdot(1-x)\cdot\delta}{\mu_l\cdot(1-\varepsilon)}$	

Correlation	Fluid	Conditions	Formula	MAE
			$h_{nb} = 131 \cdot P_r^{-0.0063} \cdot (-\log_{10} P_r)^{-0.55} \cdot M^{-0.5} \cdot q''^{0.58}$ $h_{cb} = 0.0133 \cdot Re_{\delta}^{0.69} \cdot Pr_l^{0.4} \cdot \frac{\kappa_l}{\delta}$ Then calculate the following quantities $\varepsilon_{0.18} = \varepsilon(x{=}0.18)$ $A_{L_{0.18}} = A_L(x{=}0.18)$ $\delta_{0.18} = \delta(x{=}0.18)$ $S = 1 - 1.14 \cdot (D/0.00753)^2 \cdot (1 - \delta/\delta_{0.18})^{2.2}$ $h_{wet} = ((S \cdot h_{nb})^3 + h_{cb}^3)^{\frac{1}{3}}$ $h_{TP} = \frac{\theta_{dry} \cdot h_v + (2\pi - \theta_{dry}) \cdot h_{wet}}{2\pi}$ **<u>For mist flow regime (x >=0.46)</u>** $Re_{\mathrm{H}} = \frac{G \cdot D}{\mu_v} \cdot [x + \frac{\rho_v}{\rho_l}(1 - x)]$ $Y = 1 - 0.1 \cdot \left[\left(\frac{\rho_v}{\rho_l} - x\right) \cdot (1 - x)\right]^{0.4}$ $h_{TP} = \mathrm{h_M} = 2 \cdot 10^{-8} \cdot Re_H^{1.97} \cdot \mathrm{Pr}_v^{1.06} \cdot Y^{-1.83} \cdot \frac{\kappa_v}{D}$ **<u>For dry out regime (0.46> x > 0.35)</u>** $h_{TP} = h_{TP(x=0.35)} - \frac{x-0.35}{0.46-0.35} \cdot [h_{TP}(x = 0.35) - h_M(x = 0.46)]$	

5.4. Heat transfer coefficient for film boiling, and critical heat flux correlations

Additionally, to the subcooled and saturated heat transfer coefficients, rudimentary models for film boiling heat transfer coefficient (table 5) and critical heat flux (table 6) were compared with the experimental results.

Table 5 -Film boiling models and correlation [146]

Models/Correlation	**Fluid**	**Conditions / Assumptions**	**Equation**
Laminar film boiling [119]	----	Laminar film formation with zero interfacial stresses	$h_f=0.707\cdot(\kappa_v^3\cdot\rho_v\cdot(\rho_l-\rho_v)\cdot g\cdot h_{fg}'/(L\cdot\mu_v\cdot\Delta T_{sat}))^{(1/4)}$ $h_{fg}'=h_{fg}\cdot(1+0.68\cdot C_{pv}\cdot\Delta T_{sat}/h_{fg})$
Turbulent Film Boiling [119]	---	Turbulent film boiling	$h_f=0.056\cdot Re^{0.2}\cdot(Pr_v\cdot Gr^*)^{(1/3)}\cdot\kappa_v/L$ $Gr^*=L^3\cdot g\cdot\rho_v\cdot(\rho_l-\rho_v)/\mu_v^2$ $Re=G\cdot D/\mu_v$
Bromley et al. [150]	Benzen, Carbon Tetrachloride, Ethyl alcohol, n-hexane	$G/(\rho_v\cdot(g\cdot D)^{0.5})>2$	$h_f=h_{co}+7/8\cdot h_r$ $h_r=\sigma_{SB}\cdot(T_{RTD}^4-T_{sat}^4)/(T_{RTD}-T_{sat})$ $h_{co}=2.7\cdot(G\cdot\kappa_v\cdot h_{fg}'/D/\Delta T_{sat})^{0.5}$

Table 6 - Critical heat flux correlations [146]

Equation source	Fluids	Conditions	Correlation	MAE
Katto [151], [152]	Water, R-12, R-21; R-114, Nitrogen, Para-hydrogen, Liquid helium I	Vertical tubes D=10 mm L=1000 mm P=1.96 – 3.44 MPa (pressures corresponding to $\frac{\rho_v}{\rho_l}$=0.109-0.306) G= 120 - 2100 kg/m^{2}s ΔH_{sub}= 0.4– 39.9 kJ/kg (subcooled enthalpy)	$q''_{CHF} = [0.234 \cdot \left(\frac{\rho_v}{\rho_l}\right)^{0.513} \cdot (We_{L,l})^{-0.433} \cdot \frac{\left(\frac{L}{D}\right)^{0.27}}{1 + 0.0031 \cdot (\frac{L}{D})}] \cdot G \cdot h_{fg}$ where $We_{L,l} = \frac{G^2 \cdot L}{\sigma \cdot \rho_l}$	25%
Song et al. [153]	Water, R-12, and CO_2	P=2.9-21.5 MPa G=121 kg/m^{2}s – 10,440 kg/m^{2}s D=1.9 mm – 24.7 mm X = subcooled – 0.955	$q''_{CHF} = G \cdot h_{fg} \cdot F_1 \cdot F_2$ $A_1 = 7.796 \times 10^{-2} \cdot We_{D,v}^{-0.4388}$ $A_2 = 1.53 \times 10^{-3} \cdot We_{D,v}^{-0.08032}$ $B_1 = 2.156 \cdot (1 - \mathrm{x})^{0.6884}$ $B_2 = 1.841 \cdot (1 - \mathrm{x})^{2.137}$ $B_3 = 0.6715 \cdot (1 - \mathrm{x})^{0.2198}$ $F_1 = \max(A_1, A_2)$ $F_2 = (B_1 + B_2 + B_3) - \max(B_1, B_2, B_3) - \min(B_1, B_2, B_3)$ $We_{D,v} = (G^2 \cdot D)/(\rho_v \cdot \sigma)$	30%
Kutateladze [154]	Water, Ethanol, Heptane, Propane, Pentane, Benzene	Pool boiling with natural convection	$q''_{CHF} = 0.131 \cdot \rho_v^{0.5} \cdot h_{fg} \cdot (g \cdot (\rho_l - \rho_v) \cdot \sigma)^{0.25}$	---

Kandlikar [155]	Water, R-123, R-22, R-134a, R-245fa, R-12, and R-236fa	Rectangular and circular channels, L/D= 10- 481, D=0.2 mm – 3.36 mm, G=23 kg/m2s - 20,000 kg/m2s, x = 0.0025 – 1, P = 0.1 MPa – 1.55 MPa	$q''_{CHF} = \sqrt{K_{2,CHF} \cdot \frac{\rho_v \cdot \sigma}{D}} \cdot h_{fg}$
			For ($We_{D.m}$ < 900, and $\frac{L}{D}$ <=140), or ($We_{D.m}$ >= 900, and $\frac{L}{D}$ <=60)
			$K_{2,CHF} = a_1 \cdot (1 + cos\theta_R) + a_2 \cdot We_{D,m} \cdot (1 - \mathrm{x}) + a_3 \cdot Ca \cdot (1 - \mathrm{x})$
			For ($We_{D.m}$ < 900, and $\frac{L}{D}$ >=230),
			$K_{2,CHF} = a_4[a_1 \cdot (1 + cos\theta_R) + a_2 \cdot We_{D,m} \cdot (1 - \mathrm{x}) + a_3 \cdot Ca \cdot (1 - \mathrm{x})]$
			For $We_{D,m}$ >= 900, and $\frac{L}{D}$ >=100
				19.7%

Equation source	Fluids	Conditions	Correlation	MAE
			$K_{2,CHF} = a_5 \cdot \left(\frac{1}{We_{d,m} \cdot Ca}\right)^n \cdot [a_1 \cdot (1 + cos\theta_R) + a_2 \cdot We_{D,m} \cdot (1 - \mathrm{x}) + a_3 \cdot Ca \cdot (1 - \mathrm{x})]$ Where $We_{D.m} = \frac{G^2 \cdot D}{\rho_m \cdot \sigma}$; $\frac{1}{\rho_m} = \frac{\mathrm{x}}{\rho_v} + \frac{1-\mathrm{x}}{\rho_l}$; $Ca = \frac{\mu_l \cdot G}{\rho_l \cdot \sigma}$, and $cos\theta_R = \frac{G^2 \cdot (1-\mathrm{x}) \cdot D}{\rho_m \cdot \sigma}$ And the constants are: a_1=1.03×10^{-4}; a_2=5.78×10^{-5}; a_3=0.783; a_4=0.125; a_5=0.14; n=0.07	
M.B. Bowers et al. [156]	R-113	Micro and mini heat sinks. D=0.51 mm, and 2.54 mm L=10 mm ΔTsub= 10 °C – 32 °C G= up to 95 ml/min.	$q^{''}_{CHF} = 0.16 \cdot We_{L,l}^{-0.19} \cdot \left(\frac{L}{D}\right)^{-0.54} \cdot G \cdot h_{fg}$ $We_{L,l} = \frac{G^2 \cdot L}{\sigma \cdot \rho_l}$, the Weber number	30%
A.E Bergles et al. [53]	Water, and R-113	Rectangular microchannel block with 21-0.215×0.821 mm. G=86 kg/m2s – 368 kg/m2s . Tin=30 ℃ , or 60 ℃ P=1.13 bar	$q^{''}_{CHF} = 33.43 \cdot \left(\frac{\rho_v}{\rho_l}\right)^{1.11} \cdot We_{L,l}^{-0.21} \cdot \left(\frac{L}{D}\right)^{-0.36} \cdot G \cdot h_{fg}$	30%

5.5. Bubble dynamics model of subcooled, near critical CO2

The models presented in this section are intended to verify and predict the experimental observations. Thermally driven bubble growth was derived by Mikic et al. [65], the model was chosen due to its rudimentary nature as it uses asymptotic assumptions to predict thermally driven and inertia driven bubble growth:

$$D(t) = \frac{4 \cdot \Delta T_{sat} \cdot k_l}{h_{fg} \cdot \rho_g} \cdot \sqrt{\left(\frac{3 \cdot t}{\pi \cdot \alpha_l}\right)} \quad (13)$$

Where D is the bubble diameter, t is the time since bubble nucleation, ΔT_{sat} is the superheat temperature (i.e., the difference between the wall temperature and the saturation temperature), k_l is the thermal conductivity of the liquid at the inlet temperature, h_{fg} is the latent heat of vaporization, ρ_g is the density of

the vapor, and αl is the thermal diffusivity of the liquid. The superheat temperatures required for the bubble inception were well within the RTD uncertainty range, therefore the superheat temperature was calculated according to [74] (i.e., Stepanoff coefficient), the coefficient was used since within the applied heat flux range, the difference in the superheat temperature was within the RTDs' uncertainty range.

$$\Delta T_{sat} = \frac{h_{fg} \cdot \rho_g}{\rho_l \cdot C_{P_l}} \tag{14}$$

Where ρ_l is the liquid's density and C_{pl} is the liquid's specific heat.

The bubble velocity, (i.e., v), was calculated relative to the apparent liquid velocity, u, at the position of the bubble center. For that, the Poiseuille velocity profile was used to describe the liquid's local speed, which was fully developed due to adequate distance from the inlet to the heater's leading edge. The relative velocity ratio (i.e., w_m=(v-u)/u) was then derived by averaging 92 measurements from a fully developed subcooled flow boiling experiments, and an average value of 0.74 with a standard deviation of ±0.12 was obtained. Since the bubbles had a spherical shape for reduced pressures below 0.95 and maintained a contact point with the heater, the fluid velocity driving the bubble was predicted by the Poiseuille equation at a position corresponding to the bubble's center. Subsequently, the bubble's velocity was expressed as function of its radius:

$$v = (1 - w_m) \cdot \frac{6 \cdot G \cdot A}{\rho_l \cdot h^3 \cdot w} \cdot \frac{D(t)}{2} \cdot (h - \frac{D(t)}{2}) \tag{15}$$

Following the velocity profile, the bubble location was calculated by integrating the bubble velocity according to [157]:

$$x_b = \int_0^t v \, dt + x_n \tag{16}$$

Where x_b, and x_n are the bubble position and its nucleation site relative to the heater's leading edge.

The experimentally obtained bubble radii were compared with Mikic et al. asymptotic solution [65], combined with stepanoff coefficient [74], Eqs. 13 and 14. The bubble location was calculated by inserting its diameter into Eq. 15 and integrating until the bubble drifted outside the optical window, Eq. 16.

Equations 13 thru 16 provided the bubble diameter and velocity as a function of time and location. The theoretical values were compared with the corresponding experimentally measured values.

A mean diameter error (MDE) was defined to quantify the deviation between experiments and the model according to:

$$MDE = \frac{\sum_1^n |D_{calc} - D_{exp}|}{n} \tag{17}$$

5.6. Pressure drop and Joule-Thomson effect

Because the inlet and the exit thermodynamic states varied (i.e., liquid, pressurized liquid, supercritical, and vapor), the states along the orifice needed to be deciphered. For this, the length of the orifice was divided into 100 subsections where the properties in each section were evaluated using the inlet conditions. The division was done similar to Garcia-Valladares [158] to achieve better partition towards the orifice's exit (smaller steps towards the exit where the pressure drop and the thermodynamic changes are usually the most significant):

$$\Delta x_i = \frac{L_o}{\tanh(k)} \cdot [\tanh\left(k \cdot \frac{i}{n}\right) - \tanh\left(k \cdot \frac{i-1}{n}\right)] \tag{18}$$

For the homogeneous flow model [1], [119], [137], [159] and the separated flow model [137], [159], [160], the enthalpy across the orifice was assumed to be constant. For the capillary tube model [120]–[122], the enthalpy varied, and therefore, was calculated for each subsection. All the other properties (e.g., temperature, density, and quality) were obtained using the Span and Wagner equation of state [11] from NIST REFPROP database [161]. Contrary to the two-phase flow, the single-phase portion in the homogeneous and separated flow models were calculated similarly [137], [159]. The nature of the flow used to develop the capillary tube flow [120]–[122] holds true for all flow conditions, however, different assumptions for the partial derivatives were used for the single-phase and two-phase segments (i.e., $(\partial\upsilon/\partial h)_p$ and $(\partial\upsilon/\partial p)_h$). For the single-phase flow the derivatives equaled zero since the properties were relatively constant, and for the two-phase flow the derivatives were obtained assuming linear relations (i.e., $(\partial\upsilon/\partial h)_p = (\upsilon_v - \upsilon_l)/(h_l - h_v)$ and $(\partial\upsilon/\partial p)_h = (\upsilon_i - \upsilon_{i,dp})/dp$ where dp equaled 100 kPa). For all the models, the mass

quality, x, determined the phase of the flow (i.e., single-phase or two-phase flow). The friction factors, f, significantly affected the accuracy of the models, and consequently, the ones that best fitted to the experiments were integrated into the models. Table 7 list the correlations and models that were examined in this study.

Table 7- Pressure drop examined models

Model	Equations
Homogeneous [1], [119], [137], [159]	Single-phase portion[137]: $$U_m = \frac{\dot{m}}{\rho \cdot A_o}$$ $$A_o = \frac{\pi}{4} \cdot D_{ho}^2$$ friction factor, Wang et al. correlation [159]: $$Re = \frac{\rho \cdot U_m}{D_{ho} \cdot \mu}$$ $$Re < 2300$$ $$f = 64/Re$$ $$2300 \leq Re \leq 3400$$ $$f = 0.06539 \cdot e^{-\left(\frac{Re-3516}{1248}\right)^2}$$ $$Re > 3400$$ $$f = [-2.34 \cdot \ln\left(\left(\frac{\varepsilon}{1.72}\right) - \frac{9.26}{Re} \cdot \ln\left(\left(\frac{\varepsilon}{29.36}\right)^{0.95} + \left(\frac{18.35}{Re}\right)^{1.108}\right)\right)]^{-2}$$ $$\Delta P_{i_{sp}} = (f \cdot \rho \cdot U_m^2)/2D_{ho} \cdot \Delta x_i$$ Tow-phase portion: Cheng et al. friction pressure drop correlation [1]: $x \leq 0.35$ (annular flow) $$\varepsilon_m = \frac{x}{\rho_v} \cdot \left(\left(1 + 0.12 \cdot (1-x)\right) \cdot \left(\frac{x}{\rho_v} + \frac{1-x}{\rho_l}\right) + \frac{1.18 \cdot (1-x) \cdot [g \cdot \sigma \cdot (\rho_l - \rho_v)]^{\frac{1}{4}}}{G \cdot \rho_l^{\frac{1}{2}}} \right)^{-1}$$ $$U_l = \frac{G \cdot (1-x)}{\rho_l \cdot (1-\varepsilon_m)}$$

Model	Equations

$$U_v = \frac{G \cdot x}{\rho_v \cdot \varepsilon_m}$$

$$We_l = \rho_l \cdot U_l^2 \cdot \frac{D_{ho}}{\sigma}$$

$$\mu_m = x \cdot \mu_v + (1 - x) \cdot \mu_l$$

$$Re_m = \frac{G \cdot x \cdot D_{ho}}{\mu_v \cdot \varepsilon_m}$$

$$f = 3.128 \cdot Re_m^{-0.454} \cdot We_l^{-0.0308}$$

$$\Delta P_{fi} = \frac{2 \cdot f \cdot \rho_v \cdot U_v^2}{D_{ho}} \cdot \Delta x_i$$

if $0.18 \leq x$, additional portion is added

$$Re_{Lo} = \frac{G \cdot D_{ho}}{\mu_l}$$

$$f_{Lo} = \frac{0.079}{Re_{Lo}^{0.25}}$$

$$\Delta P_{fi} = [\frac{2 \cdot f_{Lo} \cdot G^2}{D_{ho} \cdot \rho_l} \cdot \left(1 - \frac{\varepsilon_m}{\varepsilon_{m@x=0.18}}\right) + \frac{2 \cdot f \cdot \rho_v \cdot U_v^2}{D_{ho}} \cdot \frac{\varepsilon_m}{\varepsilon_{m@x=0.18}}]\Delta x_i$$

$x \geq 0.46$ (Mist flow)

$$\varepsilon_m = \left(1 + \frac{(1 - x)}{x} \cdot \frac{\rho_v}{\rho_l}\right)^{-1}$$

$$\rho_m = \varepsilon_m \cdot \rho_v + (1 - \varepsilon_m) \cdot \rho_l$$

$$\mu_m = x \cdot \mu_v + (1 - x) \cdot \mu_l$$

$$Re_m = G \cdot D_{ho} / \mu_m$$

$$f = \frac{91.2}{Re_m^{0.832}}$$

Model	Equations
	$$\Delta P_{fi} = \frac{2 \cdot f \cdot G^2}{D_{ho} \cdot \rho_m} \cdot \Delta x_i$$
	$0.35 < x < 0.46$
	$$\Delta P_{fi} = \Delta P_{fi@x=0.35} - \frac{x-0.35}{0.46-0.35} \cdot (\Delta P_{fi@x=0.35} - \Delta P_{fi@x=0.46})$$
	contribution of acceleration on a pressure drop [119]:
	$$\varepsilon_m = \frac{x}{\rho_v} \cdot \rho_m$$
	$$\rho_m = \left(\frac{x}{\rho_v} + \frac{(1-x)}{\rho_l}\right)^{-1}$$
	$$\Delta P_{ai} = G^2 \cdot (\frac{x^2}{\varepsilon_m} \cdot \nu_v + \frac{(1-x)^2}{1-\varepsilon_m} \cdot \nu_l) \cdot \Delta x_i$$
	$$\Delta P_{i_{tp}} = \Delta P_{ai} + \Delta P_{fi}$$
Separated [137], [159], [160]	Single-phase portion [137], [159]:
	Like the single phase in the Homogeneous model.
	Two-phase portion [160]:
	$$Re_l = G \cdot D_{ho}/\mu_l$$
	$$Re_v = G \cdot D_{ho}/\mu_v$$
	for Re_l and Re_v, f_l and f_v defined respectively according to:
	$Re < 1055$
	$f = 64/Re$
	$Re \geq 1055$

Model	Equations
	$$f = \left(0.86859 \cdot \ln\left(\frac{Re}{1.964 \cdot \ln(Re) - 3.8215}\right)\right)^{-2}$$
	$$E = (1-x)^2 + x^2 \cdot \rho_l/\rho_v \cdot f_v/f_l$$
	$$F = x^{0.78} \cdot (1-x)^{0.224}$$
	$$H = \left(\frac{\rho_l}{\rho_v}\right)^{0.91} \cdot \left(\frac{\mu_v}{\mu_l}\right)^{0.19} \cdot \left(1 - \frac{\mu_v}{\mu_l}\right)^{0.7}$$
	$$\rho_m = \left(\frac{x}{\rho_v} + \frac{(1-x)}{\rho_l}\right)^{-1}$$
	$$We = \frac{G^2 \cdot D_{ho}}{\sigma \cdot \rho_m}$$
	$$Fr = \frac{G^2}{g \cdot D_{ho} \cdot \rho_m^2}$$
	$$\phi^2 = E + \frac{3.24 \cdot F \cdot H}{Fr^{0.045} \cdot We^{0.035}}$$
	$$\Delta P_{fi} = \frac{2 \cdot f_l \cdot (G \cdot (1-x))^2}{D_{ho} \cdot \rho_l} \cdot \phi^2 \cdot \Delta x_i$$
	acceleration pressures drop (i.e., ΔP_{ai}) is calculated as in the homogeneous model.
	$$\Delta P_i = \Delta P_{ai} + \Delta P_{fi}$$
Adiabatic capillary flow [120]–[122], [159]	Physics based equations [120], [121]:
	$$\Delta P_i = \frac{\left(\frac{f \cdot G^2}{2 \cdot D_{ho} \cdot \rho}\right) \cdot \left[1 + \frac{G^2}{\rho} \cdot \left(\frac{\partial v}{\partial h}\right)_p\right]}{1 + G^2 \cdot \left[\frac{1}{\rho} \cdot \left(\frac{\partial v}{\partial h}\right)_p + \left(\frac{\partial v}{\partial p}\right)_h\right]} \cdot \Delta x_i \quad ; \quad \frac{\Delta h_i}{\Delta P_i} = \frac{\frac{G^2}{\rho} \cdot \left(\frac{\partial v}{\partial p}\right)_h}{1 + G^2 \cdot \frac{1}{\rho} \left(\frac{\partial v}{\partial h}\right)_p}$$
	For single phase:
	f – Calculated using Wang et al. correlation [159].
	$\left(\frac{\partial v}{\partial h}\right)_p = 0$, and $\left(\frac{\partial v}{\partial p}\right)_h = 0$ [122]
	For two-phase:

Model	Equations
	$\rho_m = \left(\frac{x}{\rho_v} + \frac{1-x}{\rho_l}\right)^{-1}$
	$U_m = G/\rho_m$
	$\mu_m = \frac{\left(\frac{x \cdot \mu_v}{\rho_v} + \frac{(1-x)\cdot\mu_l}{\rho_l}\right)}{\frac{x}{\rho_v} + \frac{1-x}{\rho_l}}$
	$Re = \rho_m \cdot U_m \cdot D_{ho}/\mu_m$
	f – Churchill's correlation [159].
	$A_{Ch} = \left(-2 \cdot \ln\left(\left(\frac{\varepsilon}{3.7}\right) + \left(\frac{7}{Re}\right)^{0.9}\right)\right)^{16}$; $B = \left(\frac{37530}{Re}\right)^{16}$
	$f = 8 \cdot \left(\left(\frac{8}{Re}\right)^{12} + (A_{Ch} + B)^{-\frac{3}{2}}\right)^{\frac{1}{12}}$
	$\left(\frac{\partial v}{\partial h}\right)_p = \left(\frac{1}{\rho_v} - \frac{1}{\rho_l}\right)/(h_v - h_l)$ [122]
	and $\left(\frac{\partial v}{\partial p}\right)_h = \left(\frac{1}{\rho(p_i, h_i)} - \frac{1}{\rho(p_i - dp, h_i)}\right)/dp$
	where dp=100 KPa
Short-tube orifice [128]	$C = 233.9 + 3.67 \cdot P_r^{0.6247} - 235.6 \cdot e^{0.03489 \cdot T_r}$
	$P_r = \frac{P_1}{P_c}$; $T_r = \frac{T_1 - T_c}{T_c}$
	$\Delta P = G^2 \cdot \frac{1 - \left(\frac{D_{ho}}{D_{hc}}\right)^4}{2 \cdot \rho_1 \cdot C}$

The experimental results of the Joule-Thomson coefficient were compared with the Span and Wagner [11] and the Wang et al. [162] models. The values produced from the Span and Wagner [11] model were obtained using NIST, REFPROP database [161].

6. RESULTS

6.1. Onset and subcooled flow boiling of near critical liquid carbon dioxide

For inception of bubble growth and the subcooled flow boiling study, twenty-six experimental conditions were studied consisting of about 17 sample points for each run — a total of 442 data points. Independent variables included pressure, mass flux, heat flux, and channel orientation (i.e., the heated surface either faced up or down, but mostly faced down); dependent variables included local surface temperatures, flow patterns, heat transfer coefficients, and onset of nucleate boiling (ONB). Pressure ranged from 6 MPa to 6.91 MPa gauge (i.e., reduce pressures ranging from 0.82 to 0.95); mass flux varied between 148.1 kg/m^{2}s and 1703.7 kg/m^{2}s, whereas most of the data points were concentrated around 160, 550 and 1550 kg/m^{2}s; and a heat flux of up to 55 W/cm^2 was applied.

6.1.1. Boiling curves

Figure 17 depicts boiling curves at three different pressures. At low heat fluxes, single-phase liquid flow was observed in which the temperature difference was a function of the location — as expected for constant heat flux boundary condition. Following the onset of nucleate boiling, the local surface temperatures gradually converged, suggesting a transition to fully developed nucleate flow boiling.

Portions of this chapter previously appeared in:

A. Parahovnik, M. Asadzadeh, S. S. Vasu, and Y. Peles, "Subcooled Flow Boiling of Carbon Dioxide Near the Critical Point Inside a Microchannel," *Phys. Rev. Appl.*, vol. 14, no. 5, p. 054050, Nov. 2020.

Anatoly Parahovnik, Yoav Peles, 2022, "High pressure saturated flow boiling of CO2 at the micro scale", *International Journal of Heat and Mass Transfer*, Vol. 186.

Anatoly Parahovnik, Yoav Peles, 2022, "Bubble dynamics in a subcooled flow boiling of near-critical carbon dioxide", *International Journal of Heat and Mass Transfer*, Vol. 183, Part C.

Anatoly Parahovnik, Yoav Peles, 2022, "Heat transfer mode shift to adiabatic thermalization in near-critical carbon dioxide with flow boiling in a microchannel", *International Journal of Heat and Mass Transfer*, Vol. TBD.

A. Parahovnik, P. Ahmed, Y. Peles, "Pressure drop and Joule-Thomson effect in a micro orifice with trans critical carbon dioxide flow", *Journal of supercritical fluids*, under review.

In fully developed nucleate flow boiling, the heat transfer process is dominated by the generation of bubbles and the associated latent heat transfer, rather than by forced convective processes. As a result, it is less dependent on mass flux. Thus, curves for different mass fluxes tend to converge. The onset of nucleate boiling was recorded at superheat temperatures (ΔT_{ONB}) of 1.2 K, 0.82 K, and 0.64 K for pressures of 6.24 MPa, 6.41 MPa, and 6.55 MPa, respectively.

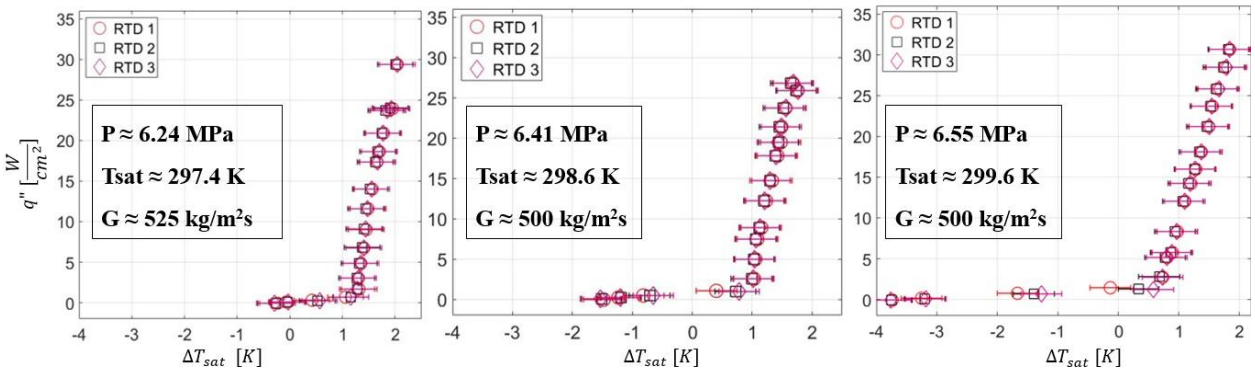

Figure 17- Boiling curves for pressures of 6.24, 6.41, and 6.55 MPa. Low superheat temperatures at ONB of 1.2 K, 0.82 K, and 0.64 K, respectively, were observed. All curves are steep for post-ONB conditions, indicating high heat transfer coefficients during flow [64]

6.1.2. Onset of nucleate boiling

The superheat temperature at the onset of nucleate boiling was determined through the intersection of two linearly fitted curves — one for the single-phase liquid data and one for the flow boiling data. The superheat temperatures at the local onset of nucleate boiling (i.e., once boiling was initiated at a particular location) were inferred for each RTD separately. It was found that the deviations were about one-fourth of the measurement uncertainty. Thus, it was concluded that the local onset of nucleate boiling was independent of position, at least under the conditions considered in this study.

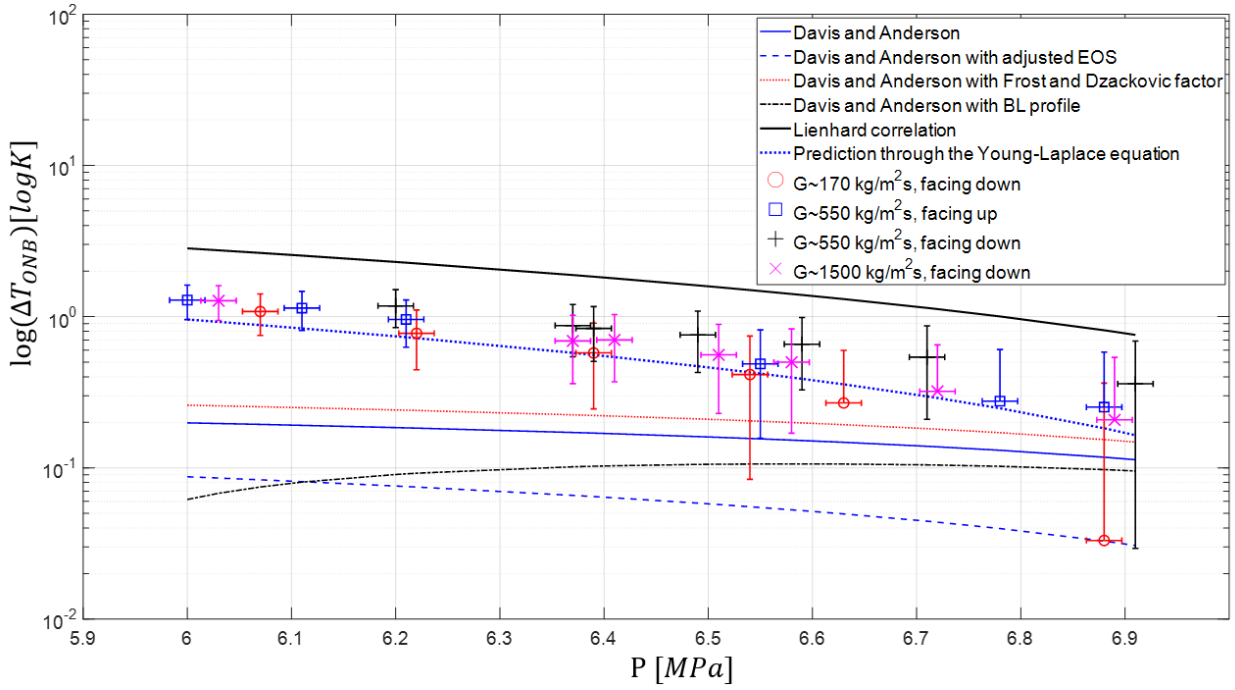

Figure 18- The experimentally obtained excess temperature at the onset of nucleate boiling along with predictions of several models. The ΔT_{ONB} values are much lower than those typically reported at low reduced pressures, and they tend to diminish with pressure [64].

As shown in Figure 18, a peak value of ΔT_{ONB} =1.6 K was observed at the lowest pressure, which gradually diminished as the pressure approached the critical condition. The dependencies of pressure and mass flux on ΔT_{ONB} was evaluated using a Pearson correlation coefficient [163], which identified dependencies between the superheat temperature and the mass flux and between the superheat temperature and pressure. Values of 0.06 and -0.94 were obtained for the relation of ΔT_{ONB}-G and ΔT_{ONB}-P, respectively. (A value of one suggests perfect linear dependency, a value of zero means no dependence, and a negative value corresponds to an inverse dependency). Thus, ΔT_{ONB} strongly depended on the pressure, but not on the mass flux. The effect of the orientation was within the uncertainty level, and therefore, was indistinguishable.

The Lienhard correlation [9] assumes homogenous bubble nucleation, as opposed to heterogeneous nucleation. Under this assumption, the onset of nucleate boiling only occurs at the molecular level when

the fluid attains a temperature higher than the corresponding metastable state. Therefore, the correlation provides an upper bound for the superheat temperature required for boiling inception. In engineered systems, homogenous nucleation cannot be practically implemented, and the boiling is initiated by heterogeneous nucleation, corresponding to lower superheated temperature, as observed in the current experimental study.

On the other hand, the Davis and Anderson's model assumes a wide range of active cavity sizes, thus, providing a lower bound for the onset of nucleate boiling. The heated surface used in the experiments was polished. Therefore, it had a limited range of cavities to initiate bubble nucleation, leading to higher superheat temperatures than those predicted by Davis and Anderson's model.

Figure 18 also shows that most of the theoretical calculations were unable to predict the experimental results, whether it is an empirical correlation (i.e., Lienhard's correlation) or theoretically derived models (i.e., Hsu's and Davis and Anderson's). The Lienhard's correlation overpredicted all the experimental results with a mean average error (MAE) of 259% but captured the observed trend. MAEs of 83.2%, 88.1%, 80%, 85% were calculated for the Davis and Anderson's model [45] and along with the adjusted equation of state (EOS) (i.e., pv=zRT), with the Frost and Dzackovic coefficient [164], and with a boundary layer integrated profile, respectively. The Davis and Anderson's model with adjusted EOS, best captured the physical phenomena and should be examined in the future for heated surfaces with a broad range of cavity sizes.

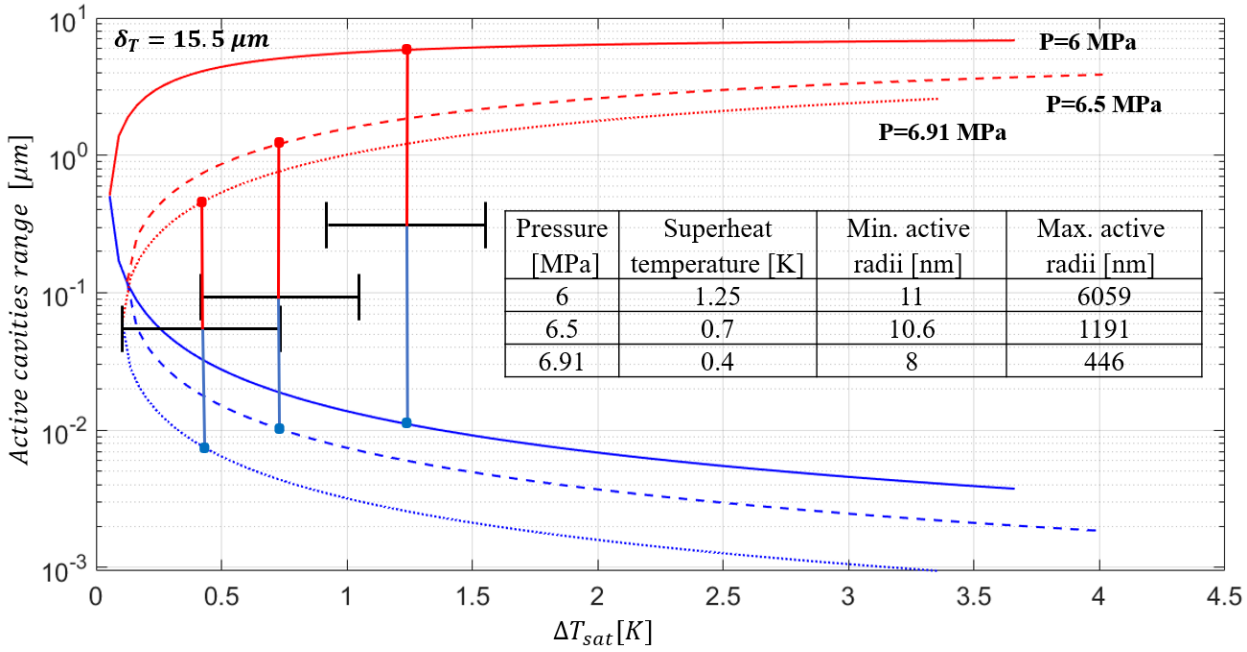

Pressure [MPa]	Superheat temperature [K]	Min. active radii [nm]	Max. active radii [nm]
6	1.25	11	6059
6.5	0.7	10.6	1191
6.91	0.4	8	446

Figure 19- The range of active nucleation sites for the three pressures studied based on Hsu's model. The three experimental results with their error bars, depicted as horizontal black lines, are superimposed on the corresponding curves generated based on ' 'Hsu's model. Vertical lines were sketched from these data points, and the intersection with the curves, marked with dots, provided the lower range and upper range of active nucleation sites. (Note that these data points' vertical positions were placed arbitrarily in the middle between the upper and lower curves.) The size of the active cavities reduces with pressure. Thus, the surface excess temperature at ONB is expected to decrease at higher pressures for smooth surfaces with only nanoscale cavities [64].

Hsu's model predicts the onset of nucleate boiling on a heated surface based on the presence of cavities within a specific size range. The hyperbolic curves in Figure 19 represent the calculated active cavities range for pressures of 6 MPa, 6.51 MPa, and 6.91 MPa. The upper branch, marked with a red line, sets the upper limit of the active cavity sizes, and the lower branch, marked with a blue line, sets the lower limit. When the surface has cavities between these two curves, bubble nucleation occurs. The crosses inside the hyperbolic curves are the measured ΔT_{ONB} for the three corresponding pressures. The limiting values for

the upper and lower intersection points, marked with large dots on the hyperbolic curves, are explicitly mentioned in the figure.

According to Hsu's model, the effect of the pressure on ΔT_{ONB} is better understood when considering the size range of active nucleation sites shown in Figure 19. The size of the active cavities decreases with pressure as apparent from the three curves' downward shift. Thus, the excess temperature at the onset of nucleate boiling on surfaces with only large cavities (larger than several microns) increases with pressure. Simultaneously, it decreases for smooth surfaces with only cavities at the nanoscale or smaller. In other words, for rough surfaces, ΔT_{ONB} is expected to increase with pressure, and on smooth surfaces, such as the one in the current study, it is expected to decrease.

For the experimentally obtained ΔT_{ONB} values, the Hsu's model predicted active radii range of 11 nm - 6059 nm, 10.6 nm - 1191 nm, and 8.0 nm - 446 nm for 6 MPa, 6.5 MPa, and 6.91 MPa, respectively, which are marked by the six dots on the three curves. Since bubble nucleation will only occur if the surface has cavities in that range, it is interesting to determine if the onset of nucleate boiling is triggered by the larger cavities or the smaller ones. To answer this question, one needs to estimate the size and type of surface cavities.

The microfluidic device's surface roughness was measured to be 150 nm, so it is evident that large cavities did not trigger the onset of nucleate boiling. Furthermore, due to the low surface tension of CO_2, these cavities were partially flooded, and therefore, produced much smaller effective nucleation sites [165]. Thus, it can be concluded that cavities initiated the onset of nucleate boiling were at the lower spectrum of the active cavity sizes corresponding to the lower three curves in Figure 19. Furthermore, the effective cavity size in the current heated surface was estimated to be about 10 nm, corresponding to the smallest active cavities calculated by Hsu's model, shown in Figure 19. If the cavities had the same geometry as discussed by Hsu, the cavity size had a nominal bubble radius of 12.5 nm. The excess temperature at the onset of nucleate boiling can now be independently estimated from the Young-Laplace equation [166].

$$P_{eff} = P_f + \frac{2 \cdot \sigma}{r_{bubble}} \quad (19)$$

And compared to the corresponding values obtained experimentally. (P_{eff} is the pressure inside the bubble, P_f is the surrounding pressure, and r_{bubble} is the bubble radius of curvature.). The lowest active cavity size predicted by Hsu's model was substituted into the Young-Laplace equation as the corresponding radius of curvature. With a known radius and a known surface tension, the pressure difference between the vapor inside the bubble and the liquid outside was directly obtained. Since the liquid pressure was known, the pressure inside the bubble was inferred. Subsequently, the saturation temperature was obtained from the thermodynamic equation of state [11] based on the calculated vapor pressure. The difference between the saturated vapor temperature inside the bubble and the surrounding liquid saturation temperature provided the superheat temperature required for the onset of nucleate boiling. Once the surface temperature is determined, the superheat temperature corresponding to P_f can be obtained and used to compare to experimental results (i.e., the excess temperature is the difference between the saturation temperature at P_{eff} and the saturation temperature at P_f). As shown in Figure 18 by the curve termed 'predictions from the Young-Laplace equation', the results are within the uncertainty measurement of the surface temperature. The Young-Laplace equation is a simplified version of the Davis and Anderson's model, where the fluid adjoined to the wall is assumed to have a uniform temperature equal to the surface temperature. This assumption holds for the current study due to the small nuclei bubbles produced on top of the polished surface.

To Conclude, the lowest active cavity size predicted by Hsu's model was used in combination with the Young-Laplace equation to predict best the superheat temperatures required for the onset of nucleate boiling on a polished surface inside a microchannel.

6.1.3. Heat transfer coefficient for subcooled boiling flow

Figure 20 shows that the local heat transfer coefficient for RTD_3 had values of 51.2-204.5 kW/m^2K. It appears that the heat transfer coefficient was proportional to the heat flux and inversely proportional to the mass flux. This conclusion agrees with the flow boiling heat transfer coefficient correlations as the boiling number is proportional to the heat flux.

The Boiling number in this study reached a value of 5×10-3, while the Shah's correlation was developed based on experimental data with Boiling numbers of ~10-3. The heat transfer coefficients were normalized using the single-phase Dittus-Boelter correlation to examine the fit of the correlations to the experimental data [141]. This normalization allowed to directly compare the experimentally obtained HTCs to Shah's dimensionless heat transfer coefficient ratio, ψ. For a pressure of 6.0 MPa with a maximum Boiling number of 2.5×10-3, the results agreed with the correlation within a margin of ±30% (see Figure 21). However, with increasing the pressure, Shah's correlation gradually under-predicted the experimental results. Likewise, experimental measurements progressively diverged from the correlation with increasing the Boiling number. Thus, the Shah's correlation was unable to predict experiments outside its original boiling number range.

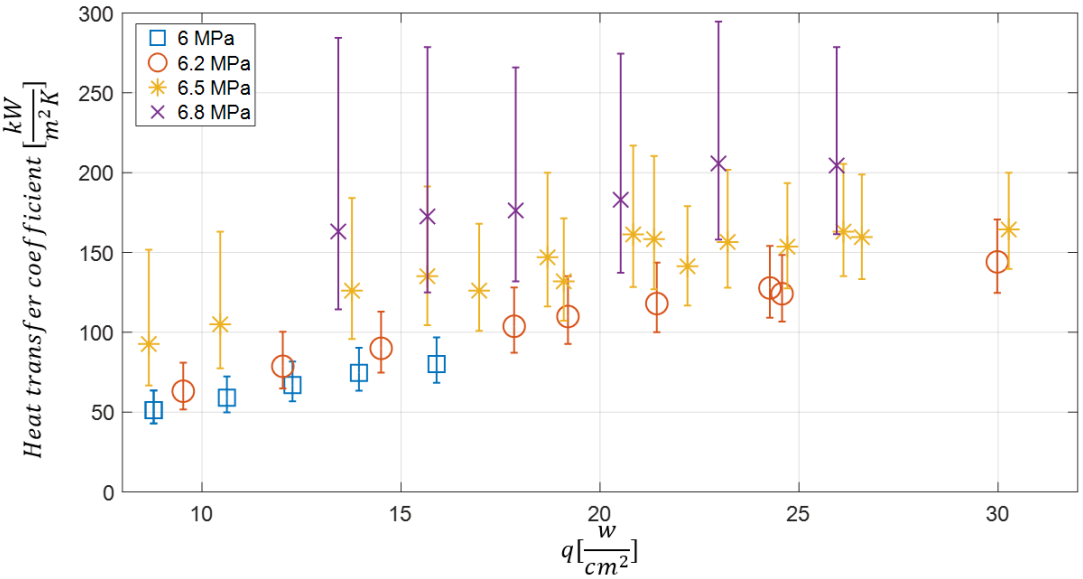

Figure 20- Heat transfer coefficient for the mass flux of 420 - 600 kg/m^{2}s at RTD$_3$. The averaged value ranged from 51.2 kW/m^{2}K to 204.5 kW/m^{2}K and was mainly dependent on the pressure. The excess temperature during boiling ranged from 0.4 K to 3 K, while the surface temperature uncertainty was ±0.33 K, leading to large uncertainties in the heat transfer coefficients [64].

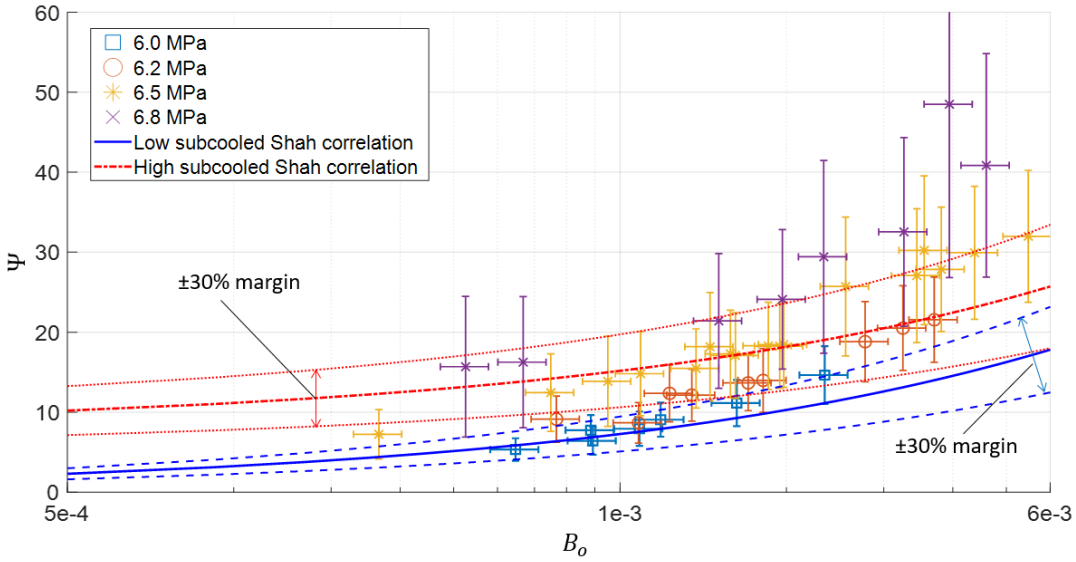

Figure 21- Comparison of the experimentally obtained dimensionless two-phase heat transfer coefficient with the Shah's correlation. The correlation reasonably predicted the heat transfer coefficient at the low pressure of 6 MPa, corresponding to relatively low Boiling numbers, but under-predicted experiments at higher pressures, corresponding to higher Boiling numbers [64].

Figure 22 compares the experimental data to the Kandlikar's correlation [48] with a correction coefficient, F_{fl}, of 1.984. The coefficient was obtained by a curve fitting process that minimized the MAE between experiments and the correlation. Regardless, it was in good agreement with the coefficient of 2.1 suggested by Ducoulombier [144]. As a general rule, the correlation predicted higher ψ compared to those of Shah's correlation. Both the Shah's correlation and the Kandlikar's correlation show a similar trend due to the Boiling number power-law used to predict ψ (0.5 and 0.7, respectively). Kandlikar's correlation best predicted the data for 6.5 MPa, whereas it over-predicted the results for the lower pressures of 6 MPa and 6.2 MPa; the highest pressure was 6.8 MPa under-predicted. Regardless, the entire data falls within a ± 70% band with an MAE of 24.3%.

If each experiment at a specific pressure was curve fitted independently, F_{fl} coefficients of 0.9457, 1.51, 1.936, and 2.686 for 6 MPa, 6.2 MPa, 6.5 MPa, and 6.8 MPa were produced, respectively. Appling F_{fl}

coefficients resulted in an MAE of 15% and encompassed the data for each pressure within a ±30% margin band.

For minimal MAE, the coefficient was linearly fitted to the reduced pressure according to Equation 15 with an R^2 of 0.986:

$$F_{fl} = 15.35 \times P_r - 11.5, \tag{20}$$

At the critical pressure, Equation 20 provides a value of 3.85, which is within the expected range reported by Kandlikar. For low reduced pressures, the equation leads to negative values, and therefore, this linear approximation should be limited to reduced pressure larger than 0.8.

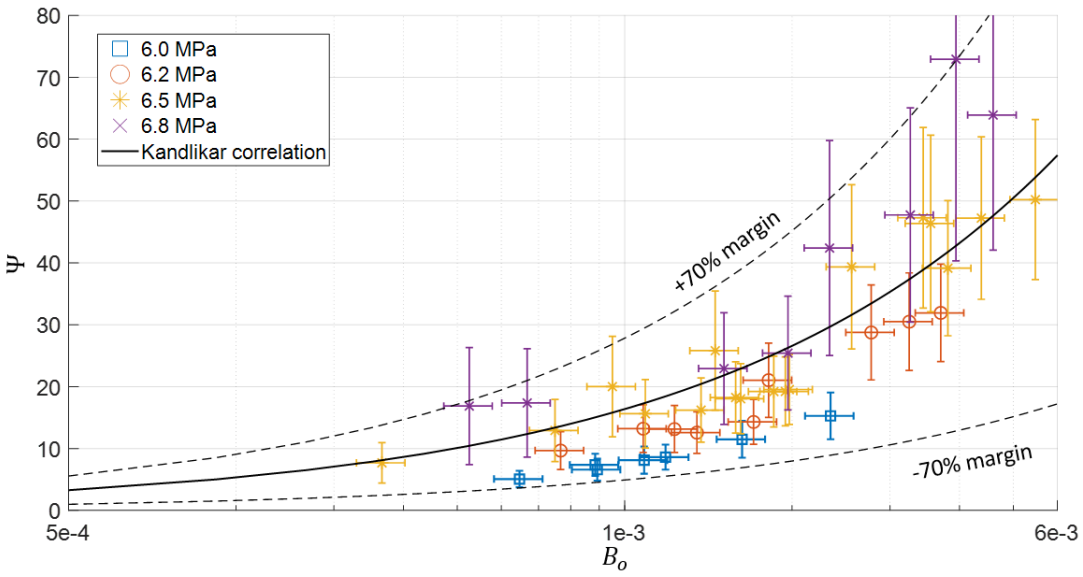

Figure 22– Comparison of the experimentally obtained dimensionless two-phase heat transfer coefficient with the Kandlikar's correlation. The correlation reasonably predicted the experimental data with an overall MAE of 24.3% [64].

The Cheng's correlation matched the experimental results with an MAE of 19.2% for the entire data. For the 6.0 MPa experiments (reduced pressure of 0.81), the correlation with its margins (±30%) coincided with the experimental data (see Figure 23). For 6.8 MPa (reduced pressure of 0.93), due to small temperature differences, the uncertainty of the experimental data was considerably larger and still within the correlated

results. However, the correlation gradually deviated from the experimental results as the critical pressure approached unity such that MAEs of 7.9%, 15.4%, 23.4%, and 29.8% for 6 MPa, 6.2 MPa, 6.5 MPa, and 6.8 MPa were recorded, respectively.

To conclude, the Shah's and Kandlikar's correlations were formulated using experimental data for a wide range of fluids. Since the Cheng's correlation was derived based on conditions closest to those used in the current study, it is not entirely surprising that it best predicted the experimental results. Nevertheless, at reduced pressures above 0.87, Chang's correlation presented significant discrepancies to experimental results.

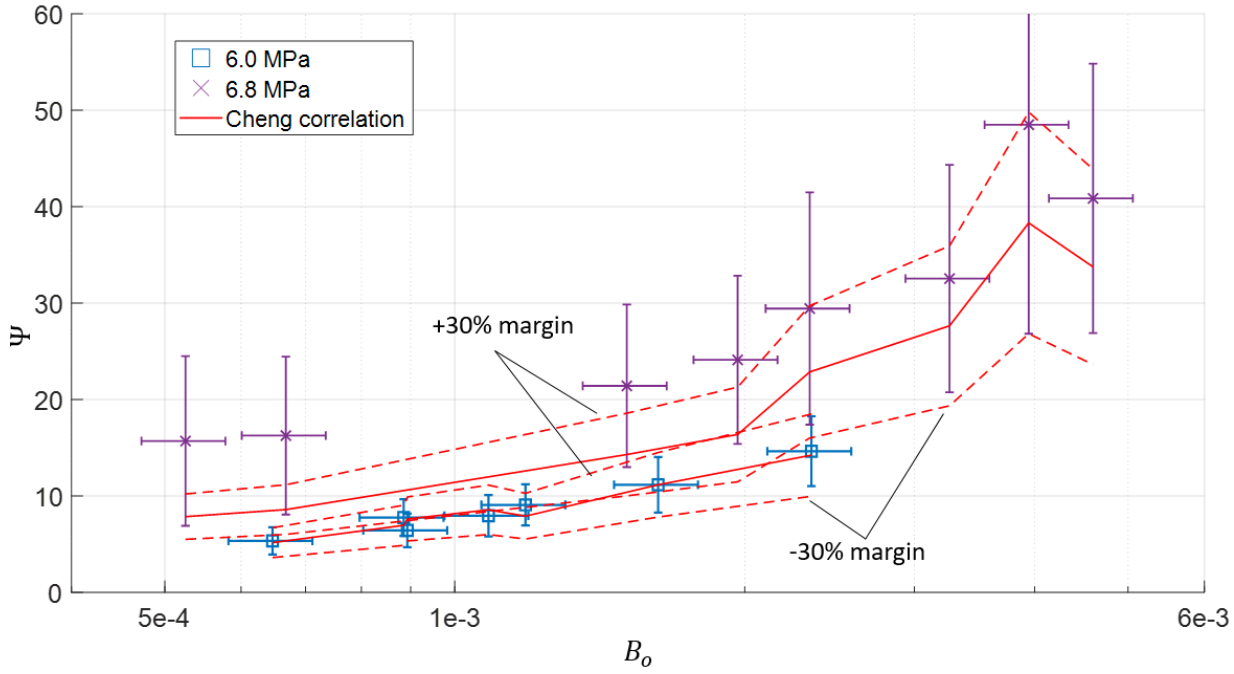

Figure 23– Comparison of the experimentally obtained dimensionless two-phase heat transfer coefficient with the Cheng's correlation. The correlation predicted the experimental data well with an MAE of 19.2% [64].

6.2. Saturated flow boiling, film flow boiling and critical heat flux of carbon dioxide

In this section, fourteen experiments were conducted with mass qualities ranging from 0 to 0.94, mass fluxes ranging from 1199 kg/m^{2}s to 2428 kg/m^{2}s, and pressures ranging from 2.36 MPa to 5.96 MPa,

corresponding to saturation temperatures of 260.6 K to 295.4 K (Table 8). The heat flux (q'') varied from 0 to about 270 W/cm^2, which was the highest possible heat flux for the current setup.

Table 8- Experimental conditions [146]

Exp.	**Flow pattern based on Cheng et al. [43].**	***x***	***P* (MPa)**	T_{sat} **(K)**	***G* (kg/m^{2}s)**	***Δx* (%)**	***ΔP* (%)**	***ΔG* (%)**
1	Bubbly	0	6.0	295.5	2428	31.1	13.9	2.6
2	Bubbly	0.05	5.6	293.0	2068	19.5	3.1	7.4
3	Bubbly	0.05	5.5	292.5	2374	48.9	8.4	0.8
4	Bubbly	0.08	5.3	290.9	1199	25.3	35.7	6.2
5	Bubbly	0.08	5.4	291.3	2162	23.7	9.7	1.6
6	Bubbly	0.13	5.1	289.4	1988	17.9	8.5	3.2
7	Bubbly	0.14	4.8	286.6	2143	5.1	2.9	4.4
8	Bubbly	0.15	5.0	287.9	2215	6.1	4.8	5.7
9	Annular	0.28	3.6	275.2	2187	11.2	10.4	9.7
10	Dry out	0.36	4.0	279.0	2256	5.0	2.6	1.3
11	Dry out	0.45	2.4	260.7	2116	0.5	1.4	3.8
12	Dry out	0.48	5.9	295.2	1791	48.6	13.5	14
13	Mist	0.83	3.7	276.7	1865	28.5	19.5	7.3
14	Mist	0.94	3.6	275.7	1699	0.6	5.0	7.4

6.2.1. Boiling curves for saturated flow boiling

Figure 24 depicts the boiling curves for experiments with average mass qualities of 0.15, 0.28, 0.36, 0.45. and 0.94. All mass qualities had a distinct fully developed boiling region (nucleate or convective boiling), and in some cases a distinct film boiling region (i.e., post-CHF conditions). The mass quality of 0.15 with nucleate boiling had the steepest q″- ΔT_{sat} slope between 49 W/cm^2 and 200 W/cm^2, and it also had a flow boiling developing region. For low qualities the transition to film boiling was distinct and was characterized by a rapid increase in ΔT_{sat} with an incremental increase in the heat flux. For higher mass qualities of x>0.28 the transition to film boiling was more gradual.

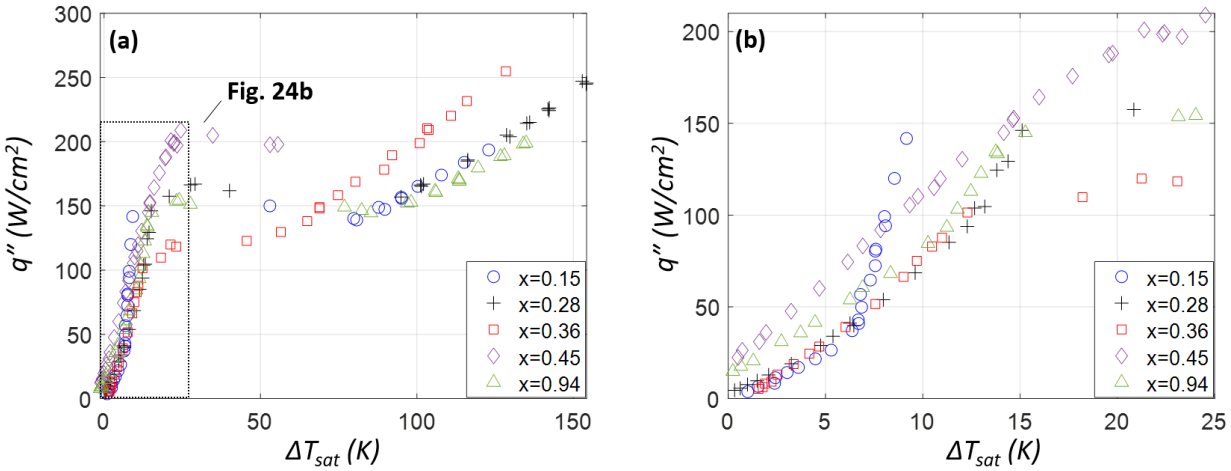

Figure 24- Boiling curves for five representative cases (Cases 8, 9, 10, 11, and 14 given in Table 9). a) Zoom out; b) Zoom-in [146].

6.2.2. Heat transfer coefficients for saturated flow, and film boiling

As shown in Fig. 25, Pre-CHF heat transfer coefficient ranged between about 50 kW/m^{2}K and about 150 kW/m^{2}K and was generally the highest for the mass quality of 0.45 (Case 11) and was most dependent on the heat flux for the mass quality of 0.15 (Case 8). The HTC for the mass quality of 0.94 (Case 14) was comparable to the lower qualities. Post-CHF heat transfer coefficient ranged between about 12 kW/m^{2}K to 21 kW/m^{2}K and was independent of the heat flux. For the mass quality of 0.45, a steady post-CHF heat transfer coefficient was not reached.

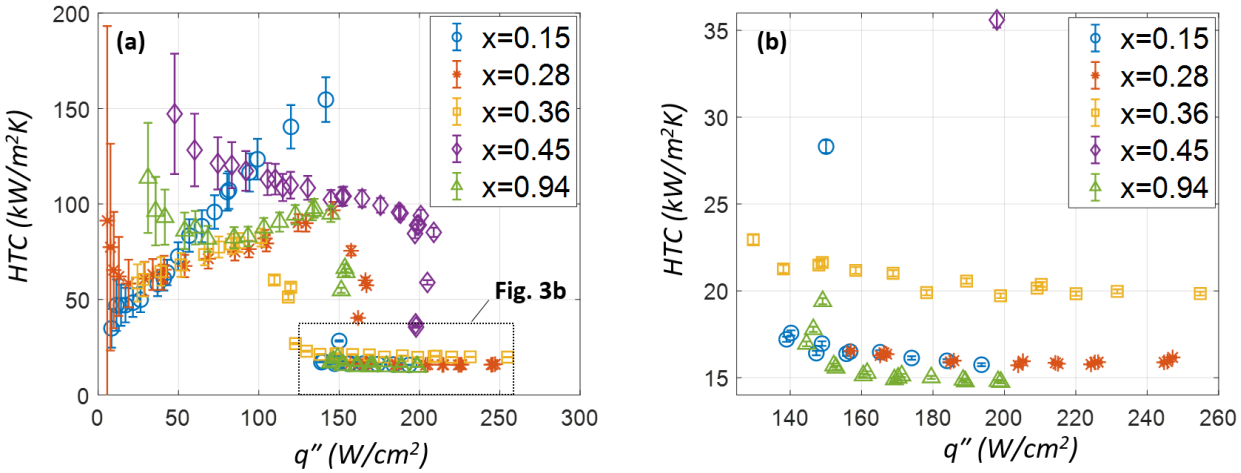

Figure 25-Two-phase heat transfer coefficients for five mass qualities for Cases 8, 9, 10, 11, and 14 given in Table 8 [146].

Figure 26 shows the two-phase heat transfer coefficients normalized by the liquid-portion-of-the-flow heat transfer coefficient (i.e., $\Psi=h_{TP}/h_{lo}$), which was evaluated at the saturated liquid conditions.

For low mass qualities the HTC was about linearly proportional to the heat flux; for intermediate mass qualities it was moderately inversely proportional to the heat flux; and for mass qualities close to unity the HTC was independent of heat flux. Established knowledge about two-phase heat transfer coefficient suggests that for nucleate flow boiling, associated with low mass qualities, the HTC is a function of the

heat flux, but not for convective boiling, associated with higher mass qualities [119]. The dependency on the heat flux of the experimental results at low mass qualities clearly follows this trend. The slight decrease of the HTC with heat flux for the mid-range mass qualities of 0.45 is probably indicative of periodic local dry-outs.

Upon reaching the CHF conditions, Ψ dropped from 9.6, 7.5, 5.7, 6.9, and 8.4 to 1.07, 1.3, 1.5, 2.7, and 1.5 for qualities of 0.15, 0.28, 0.36, 0.45, and 0.94, respectively. Note that the experiment with a mass quality of 0.45 and saturation temperature of 260.7 K (Case 11) had not reached a stable post CHF mode.

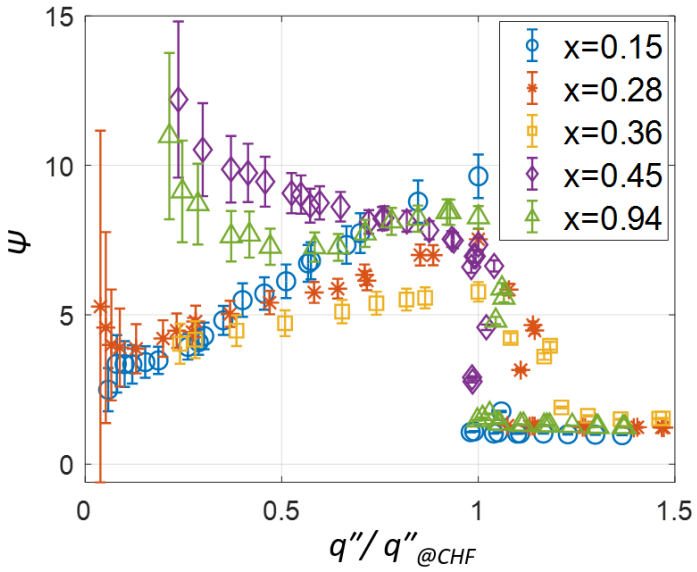

Figure 26 – Two-phase heat transfer coefficient normalized by the liquid-portion-of-the-flow heat transfer coefficient (i.e., $\Psi=h_{TP}/h_{lo}$), as a function of normalized heat flux [146].

Figure 27 presents the HTC normalized by the HTC at the CHF conditions as a function of dimensionless heat flux for a range of mass qualities. The pressure and mass fluxes were within a 11.2% margin (Table 9), allowing to independently examine reasonably well the effect of the heat flux.

For mass quality of x=0.15 an increase in the heat flux resulted in a more rigorous bubble ebullition process, which in turn led to a higher HTC. For mass quality of x=0.28, with annular flow, a liquid film formed on the heated surface and transferred the heat through evaporation to the vapor core. For convective boiling,

associated with annular flow, the heat transfer coefficient is inversely proportional to the liquid film thickness, therefore, with increasing heat flux the liquid film might have become thinner leading to higher HTC until the film ruptured, advancing the arrival of the CHF condition. Based on Cheng et al. map [43], experiments with mass qualities of x=0.36 and x=0.45 should have been under dry-out conditions where local temporal dry-out areas were formed. For x=0.36 with mass quality close to the annular to dry-out transition quality, the rupture of the liquid film, if occurred, was insignificant, which led to an increase of HTC with heat flux. On the other hand, for x=0.45, the periodic and partial rupture of the liquid film led to degradation of the HTC with heat flux.

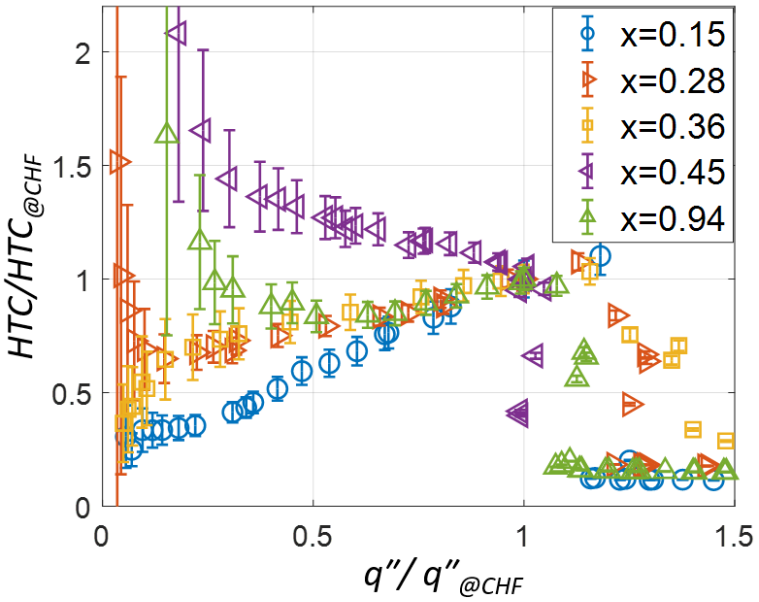

Figure 27- Normalized HTC by HTC at CHF, and q″ by q″ at CHF [146].

The experimental results were compared with Kandlikar [147], Shah [6, 7], and Cheng et al. [1, 8, 9] correlations (Table 4). The first two were developed based on multi-fluid databases, which didn't include carbon dioxide, and the latter was developed specifically for CO_2. Cheng et al. linked the correlation to flow boiling patterns and proposed a piecewise correlation that captures the different regions [1]. However, a segment of the mass flux in the current study was higher than the upper limit of the Cheng et al. correlation, and the expression for mass qualities that corresponded to the transitions between flow patterns yielded nonphysical values as the calculated mass qualities for annular to dry-out and dry-out to mist transitions

were lower than for the transition from bubbly to annular flow. Therefore, in the current study, the transition mass qualities were inferred through the flow pattern map of Cheng et al. at the highest mass flux (i.e., 1600 kg/m^2s). Based on Cheng et al. map [43], the transition mass qualities from bubbly to annular, from annular to dry-out, and from dry-out to mist were x=0.18, x=0.35, and x=0.46, respectively.

The highest HTC that was obtained for a mass quality of 0.45, is believed to be associated with the lower saturation temperature of T_{sat}= 260.7 K considered in this study. The low temperature led to a higher liquid thermal conductivity (i.e., 0.127 W/mK, compared to ~0.1 W/mK for the rest) and a higher latent heat of vaporization (i.e., 260 kJ/kg, compared to ~183 kJ/kg for the rest) that made the heat transfer process more efficient with a higher HTC. The mass quality of 0.94 presented a rapid transition to post CHF and a sharp decrease in the HTC that is attributed to a depletion of droplets at the vicinity of the heater.

Figure 28 compares the experimental results with the correlations, and Table 9 provides the mean average errors (MAEs) calculated for these correlations for each mass quality. For a mass quality of 0.15, Shah's and Cheng et al. correlations predicted well the experimental results with MAEs of 34%, and 33%, respectively, while the Kandlikar's correlation [147] overpredicted the results with an MAE of 248%. For a mass quality of 0.28, Shah's correlation [148], [149] fitted well the experiments with an MAE of 16 %; the Cheng et al. correlation [1], [40], [43] slightly overpredicted the results with an MAE of 30%, and the Kandlikar's correlation [147] overpredicted the results with an MAE of 141%. Also for the latter quality, the Kandlikar's correlation [147] had a discontinuity due to a shift between the fitted regions of the correlation. For a mass quality of 0.36 both Shah's [148], [149] and Cheng et al. [1], [40], [43] predicted the results well with MAEs of 8% and 15%, respectively. The Kandlikar's correlation [147] overpredicted the experimental results with an MAE of 104%. Regardless of the accuracy, in all correlations the HTC was dependent on the heat flux for x=0.15, x=0.28, and x=0.36, which suggests that the HTC increased with heat flux, similar to the experimentally measured HTC. For a mass quality of 0.45, Shah's correlation [6, 7] best predicted the results with an MAE of 24%; Kandlikar's correlation [147] had an MAE of 80%; and Cheng et al. [1], [40], [43] underpredicted the experiments with an MAE of 98%. For x=0.94, all

correlations underpredicted the experimental results with MAEs of 54%, 54%, and 96% for Shah's [148], [149], Kandlikar [147], and Cheng et al. [1], [40], [43] correlations, respectively. Moreover, the correlations didn't follow the experimental trend for mass qualities of 0.45 and 0.94, suggesting that the HTC increased with heat flux, contrary to the measured HTC.

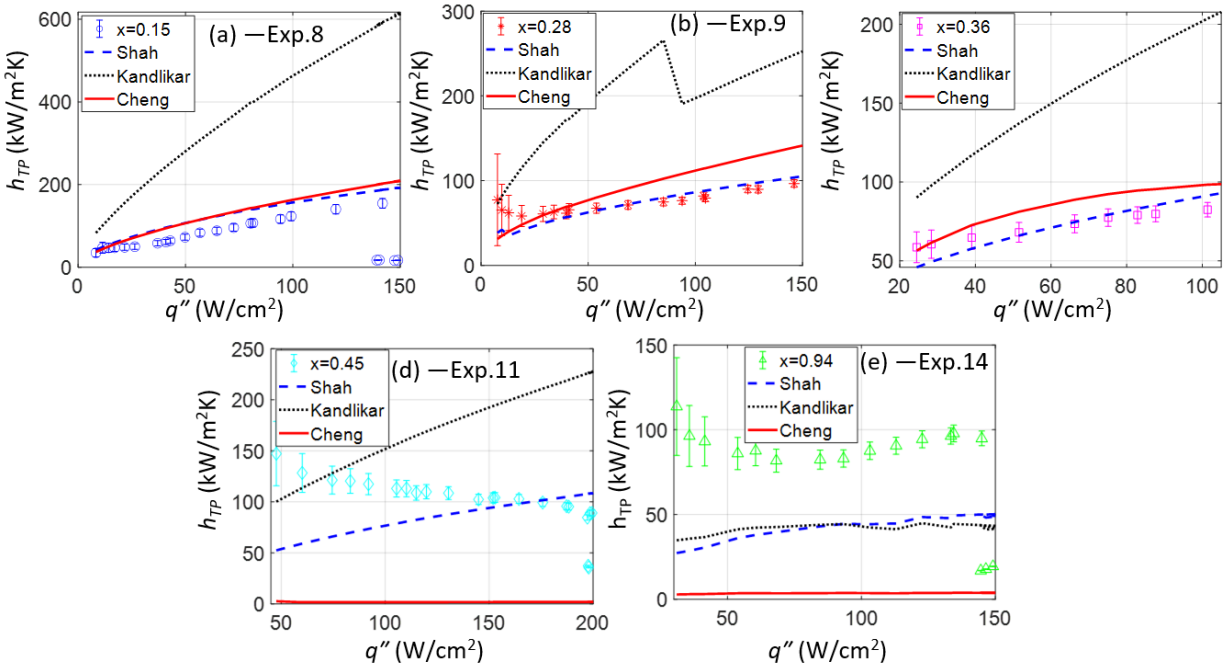

Figure 28- Comparison of the experimental results with Kandlikar [147], Shah [148], [149], and Cheng et al. [1], [40], [43] correlations [146].

Table 9- MAE for the examined correlations compared to experimental results [146].

MAEs between experiments and correlations [%] for the heat transfer coefficient				
Exp.	*x*	Kandlikar [147]	Shah [148], [149]	Cheng et al. [1], [40], [43]
8	0.15	248	34	33
9	0.28	141	16	30
10	0.36	104	8	15
11	0.45	80	24	98
14	0.94	54	54	96

As shown in Fig. 29, for film boiling, post-CHF condition, the HTC ranged from about 12 kW/m^2K to 21 kW/m^2K, which was compared with theoretical models for laminar and turbulent vapor films and with the Bromley et al. correlation [150] (Table 5). The Bromley et al. correlation was developed for flow perpendicular to a heated tube, and therefore, in the current study the heaters width was used as a diameter (i.e., D=W).

Both the laminar and turbulent models underpredicted the experimental results, while the Bromley et al. correlation overpredicted them, with average MAEs of 95%, 84%, and 237%, respectively (Table 10). The Reynolds number for film boiling is defined according to $Re= G \cdot D/\mu v$, and for the current set of experiments it ranged between 19,636 and 42,837, suggesting that the turbulent model for the film boiling should yield more accurate results, which is the case for un-adjusted models. However, from the experimental data, no clear dependency between the Reynolds number and film boiling heat transfer coefficient was observed.

The radiative contribution to the HTC in the Bromley et al. correlation was insignificant in relation to the total HTC, and therefore, can be neglected. By adjusting the coefficients (i.e., 0.707, 0.056, and 2.7 for the laminar model, the turbulent model, and the Bromley et al. correlation, respectively) the MAE was significantly reduced compared to the original values (i.e., from 95% to 27%, from 84% to 33%, and from 237% to 32%, for the laminar model, the turbulent model, and the Bromley et al. correlation, respectively). Finally, the adjusted laminar model best predicted the experimental data following the coefficient adjustment.

Table 10- Film boiling HTC — comparison to correlations [146].

Model	The constant	MAE (%)
Laminar model [119]	0.707	95
Turbulent model [119]	0.056	84
Bromley et al. [150]	2.7	237
Adjusted laminar model	15.3±4.9	27
Adjusted turbulent model	0.39±0.15	33
Adjusted Bromley et al.	0.9±0.3	32

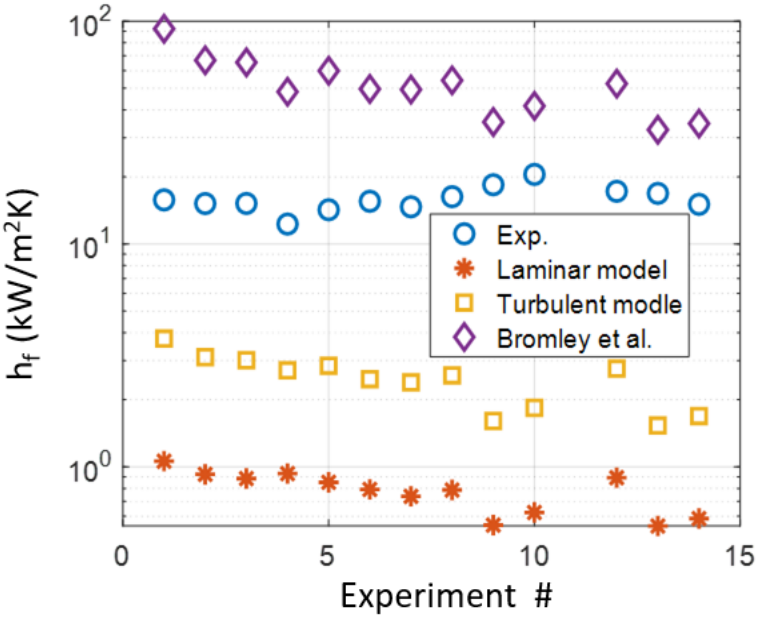

Figure 29-Film boiling heat transfer coefficient [146].

6.2.3. Critical heat flux

For a mass quality of 0.15 the departure from nucleate boiling was accompanied by a rapid increase in the superheat surface temperature and consequently led to the formation of a stable film boiling heat transfer regime. The CHF occurred at 141.7 W/cm^2 where the HTC dropped by a factor of 10. For a mass quality of 0.28, dry-out occurred abruptly, like the departure from nucleate boiling that is typical of bubbly flow. However, for a mass quality of 0.36, the flow gradually transitioned to film boiling, suggesting the steady growth of interfacial waves that progressively expanded the extent of the rupture of the liquid film. For a mass quality of 0.45, a steady post-CHF was not observed, however, a drop in the HTC was noted that could be attributed to an onset of partial dry-out.

The higher CHF at x=0.45 could also be associated with other variables, such as pressure and surface tension, that might enhance the stability of the thin liquid film on the surface. (Note that the pressure for Case 11 had the lowest pressure studied.) However, this study was unable to confirm this hypothesis, and a careful stability analysis is merited.

Several critical heat flux correlations (Table 6) were compared to the experimental results including the semi-empirical correlation of Katto et al. [151], [152] for vertical tubes at high reduced pressures, the Song et al. [153] correlation developed based on experiments for CO_2, and the Kutateladze [154] correlation for pool boiling. Correlations developed for microchannels were also evaluated including the Kandlikar [155], the Bowers et al. [156], and the Bergles et al. [53] correlations.

The Kutateladze correlation was combined with the Zuber coefficient [167], [168] of 0.131 that is suitable for large, heated plates where the nuclei bubble diameters are significantly smaller than the heated surface. Such condition was consistent with the experimental observations of bubble formation of near critical CO_2 [64]. Due to the simplicity of the Kutateladze correlation and its linkage to basic principles, it was evaluated both as is (i.e., with a Zuber constant of 0.131), and after a fitting process of the coefficient.

Prediction using the Katto et al. correlation [151] resulted in the lowest MAE despite being developed for vertical tubes, which is in-line with the assumption that gravitational effects are negligible at the micro scale, followed by the Song et al. correlation [153]. Expression that was derived by Kutateladze [154] combined with the Zuber's coefficient [167] resulted in an MAE of 56%. Kandlikar [155] correlation resulted in an MAE of 100%, and the Bowers et al. and Bergels et al. [53] correlations resulted in MAEs above 100% (Table 11). A modified Kutateladze [154] expression, with a coefficient of 0.3571±0.077, resulted in an MAE of 23%. Using the optimized value for the Kutateladze [154] expression yielded an MAE similar to Katto's correlation [151] (Figure. 30).

Table 11- Mean average errors for CHF correlations [146].

Correlation	***MAE* [%]**
Katto et al. [151], [152]	23
Song et al. [153]	47
Kutateladze [154]	56
Kandlikar [155]	100
Bowers et al. [156]	130
Bergels et al. [53]	86

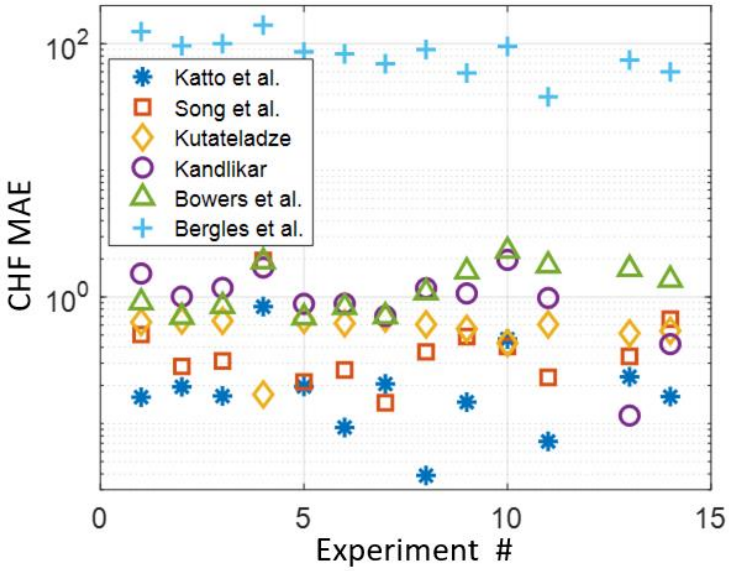

Figure 30- MAE of between correlations and experiments for CHF [146].

6.3. Bubble dynamics in a subcooled flow

The first set of experiments, given in Table 12, was used to reveal the boiling patterns, bubble-to-bubble interaction, and to examine established theoretical models for bubble speed and diameter. The second group of experiments, given in Table 12b, maintained approximately constant pressure, temperature, and mass flux to study the effect of heat flux, and to compare to established models. The results presented a classification and evolution of subcooled flow boiling from the inception of bubbles up to fully developed flow boiling. The theoretical model of Mikic et al. [65] for bubble dynamics was evaluated and compared with experiments. Interactions between bubbles, which were not considered in the original model, were presented and discussed along with the effect of pressure on the bubble formation. Subsequently, a modified model was proposed to account for bubble-bubble interactions.

Table 12- Experimental conditions for bubble dynamic study [157].

Table 12a – variable pressure, mass flux, and heat flux						
No.	P [MPa]	P_r	T_∞ [K]	ΔT_{sub} [K]	G [kg/m^{2}s]	q'' [W/cm^2]
1	6.52	0.88	296.1	2.7	475.90	1.20
2	6.59	0.89	296.1	3.1	367.44	3.13
3	7.19	0.97	296.1	6.9	469.25	5.19
4	6.51	0.88	296.1	2.6	469.00	12.20
5	6.32	0.86	295.2	2.2	523.00	7.14
6	6.71	0.91	295.8	4.2	547.51	6.66
7	6.70	0.91	296.0	3.9	413.00	5.13
8	6.61	0.9	295.7	3.6	484.30	6.88
9	6.51	0.88	296.2	2.4	280.00	4.20
10	7.02	0.95	295.4	6.5	712.00	12.50
11	7.29	0.99	296.2	7.4	464.88	6.75
12	7.20	0.98	296.4	6.7	474.00	9.20
13	6.6	0.89	296.0	3.2	304.9	4

6.3.1. Bubbly flow patterns

The flow was classified into three distinct patterns, shown in Fig. 31, that included intermittent nucleation of bubbles, individual bubble propagation, and fully developed subcooled boiling.

Intermittent nucleation of bubbles was observed at the lowest heat flux, but sufficient to activate small number of nucleation sites. The nucleated bubbles at the active sites gained their pre-departure sizes within a single frame. The bubble frequency was inconsistent, and the bubbles tended to follow a distinct streamline due to the fully developed Poiseuille profile formed inside the channel. Once the bubbles departed, they maintained their diameters and did not interact with other bubbles. Occasionally, the bubbles were stirred by liquid's spatial and temporal fluctuation that usually shifted them to another parallel streamline inside the microchannel (Fig. 31a).

At sufficiently high heat flux, a new pattern emerged, termed the individual bubble propagation, in which the number of active nucleation sites significantly increased, and the bubbles propagated slower downstream. They were larger and bubble-to-bubble interaction was occasionally observed. Additionally, the presence of bubbles suppressed the liquid phase fluctuations and occasions when bubbles moved between streamlines were rare (see Fig. 31b).

At the highest heat flux, under the fully developed flow pattern, a distinct boiling inception line perpendicular to the flow was formed close to the heater's leading edge. Liquid fluctuations were completely suppressed by a large presence of 3-μm to 5-μm bubbles that were evenly spread throughout the heater. The nuclei bubbles grew and merged downstream their nucleation sites, and the void fraction increased significantly. The void fraction at inception of intermittent bubble nucleation, individual bubble propagation, and fully developed bubbly flow was measured to be 0.2%, 1%, and 5%, respectively. Where the maximum values were 0.6%, 2%, and 8%, respectively, and the minimum values were 0.07%, 0.5%, and 4%, respectively. The void fraction was sampled by summing the volume of the bubbles assuming the bubbles were spherical, for reduced pressures below 0.95, and dividing it by the entire sampled volume.

The bubble frequency was mainly controlled by the heat flux that influenced bubble coalescence (Fig. 31c). Generally, the flow patterns had similar features regardless of the mass flux and pressure. The fully developed flow was consistent with an isolated bubble flow and confined bubbles as defined by Kandikar [169]. However, due to the small aspect ratio of the channel of 0.1, bubbles were only confined in the vertically direction. Nevertheless, for reduced pressures below 0.95, the bubbles maintained a relatively spherical shape (Fig. 31) and for reduced pressure above 0.95, the bubbles had a stream-like shape (Fig. 36).

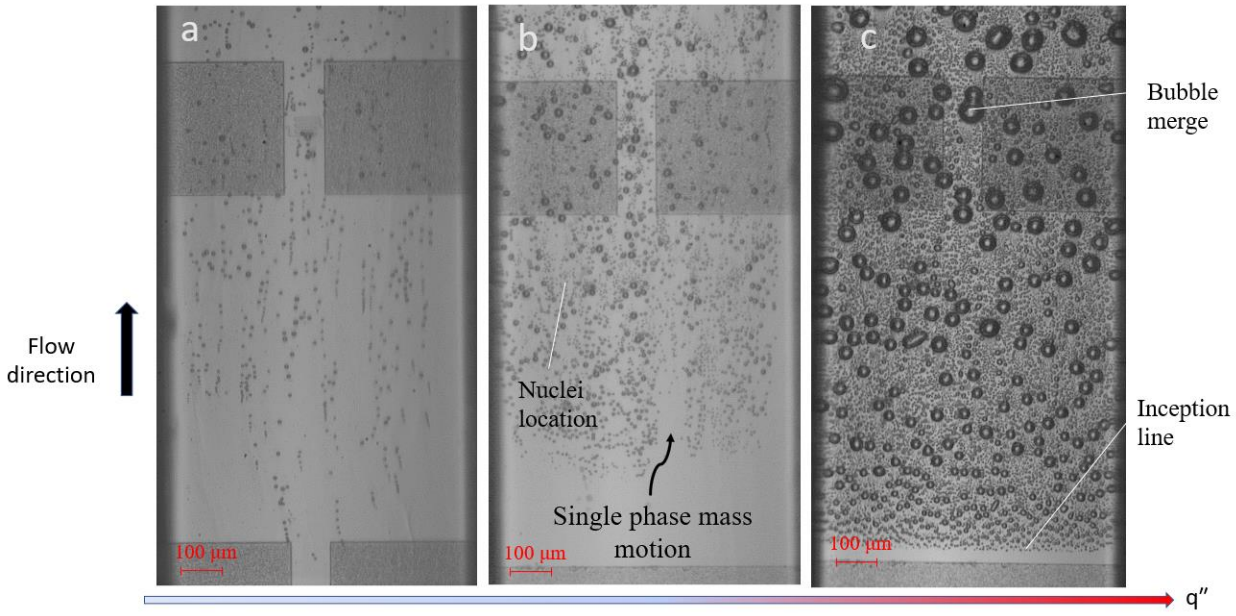

Figure 31—a) intermittent bubble nucleation, Experiment 1 (P=6.52 MPa, ΔT_{sub}=2.7 K, G=475.9 kg/m^{2}s, and q″=1.27 W/cm^2). b) single phase local oscillations that were present in the development boiling flow, Experiment 2 (P=6.59 MPa, ΔT_{sub}=3.1 K G=367 kg/m^{2}s, and q″=3.13 W/cm^2). c) Fully developed subcooled flow boiling, Experiment 6 (P=6.71 MPa, ΔT_{sub}=4.2 K, G=547.5 kg/m^{2}s, and q″=6.66 W/cm^2) .

6.3.2. Bubble growth in fully developed bubbly flow

The experimentally obtained bubble velocity as a function of time is shown in Fig. 32. The bubbles were selected to include only isolated bubbles with no bubble-to-bubble interactions. For Experiment 5 (Table 12), the bubbles were larger than for Experiment 12 (40 μm compared to 20 μm), despite a lower heat flux in Experiment 5 (7.14 W/cm^2) compared to Experiment 12 (9.2 W/cm^2). Moreover, the mass flux in Experiment 12 was lower than for Experiment 5, which resulted in slower bubble propagation that should have allowed more time for the bubble to grow. Nevertheless, the bubble in Experiment 12 were smaller. The bubbles dynamics suggests that the bubble diameter had a stronger influence on the bubble velocity than the mass flux. This is also apparent from Equation 15 in which the bubble velocity is proportional to the second power of its diameter ($D^2(t)$) and to the first power of the mass flux (G). Consequently, it could be concluded that bubble growth and movement was highly sensitive to the physical conditions, which for experiment 5 resulted in bubbles double the size compared to experiment 12. A possible explanation for the inferior fitting accuracy for Experiment 5 compared to Experiment 12 could originate from a larger density difference between the vapor and the liquid phases. This in turn, influenced the time it took for the forces to equilibrate around the bubble. The equilibration period, therefore, altered the relative velocity ratio (i.e., w_m), while for Experiment 12, the bubble velocity developed more steadily. It also can be seen that the measurements of the velocity for Experiment 5 were noisier compared to Experiment 12, further suggesting that a potential velocity change occurred due to the influence of liquid forces.

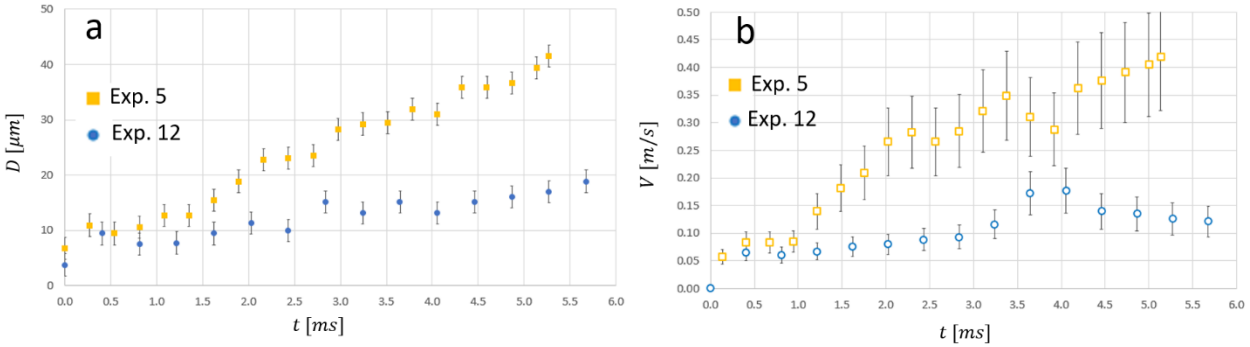

Figure 32 — Bubble's diameter (a) and velocity (b) for experiments 5 (P=6.32 MPa, ΔT_{sub}=2.2 K, G=523 kg/m^{2}s, and q″=7.14 W/cm^2 —Yellow squares) and 12 (P=7.2 MPa, ΔT_{sub}=6.7 K, G=474 kg/m^{2}s, and q″=9.2 W/cm^2 —blue circles) for bubbles that had limited bubble-to-bubble interactions [157].

The largest bubble diameter for different positions, shown in Fig. 33, had the largest number of bubble-to-bubble interactions, bubbles of such size were observed in about three different occasions through the recorded data. The reduced pressures of Experiments 9, 10, and 11 were 0.88, 0.95, and 0.99, respectively, and despite the lower heat flux for Experiment 9, the bubble was the largest. In Experiment 4 (Fig. 33b), the optical window was moved downstream between RTD_1 and RTD_2, corresponding to 1 mm to 2.5 mm from the heater's leading edge. At that range the measured bubble reached the channels height suggesting that the evaporation and bubble-to-bubble growth rate overwhelmed condensation in the subcooled temperature region and resulted in bubbles that extend outside the thermal boundary layer.

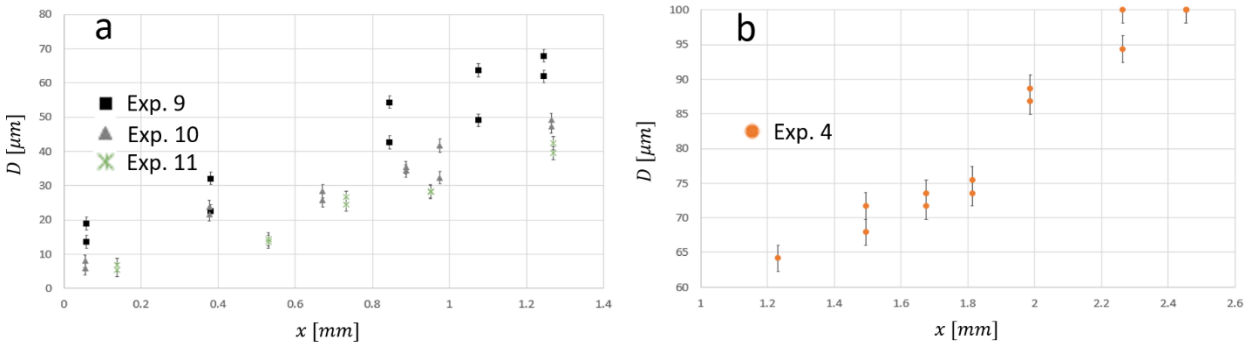

Figure 33-Bubbles' diameter as function of location (a) Experiments 9 (P=6.51 MPa, ΔT_{sub}=2.4 K, G=280 kg/m^{2}s, and q″=4.2 W/cm^2), 10 (P=7.02 MPa, ΔT_{sub}=6.5 K, G=712 kg/m^{2}s, and q″=12.5 W/cm^2), and 11 (P=7.29 MPa, ΔT_{sub}=7.4 K, G=464.88 kg/m^{2}s, and q″=6.75 W/cm^2); **(a)** divergence in resulted bubble sizes can be observed. **(b)** bubble size for Experiment 3 (P=6.51 MPa, ΔT_{sub}=2.6 K, G=469 kg/m^{2}s, and q″=12.2 W/cm^2); the data was sampled downstream compared to all other experiments and measured bubble diameter equal to channel's high [157].

6.3.3. Bubble growth and translation

Both inertial and thermal governed solutions of the Rayleigh-Plesset equation for bubble diameter [119] were examined. With the timescale pertinent to the experimental data (i.e., up to 6 ms) the inertia driven equation overpredicted the measured bubble diameter by an order of magnitude, and therefore, was rejected as a possible process controlling the bubble growth. On the other hand, the measured diameters indicated that the growth was thermally driven.

Figure 34 shows that the thermally driven model predicted well the experimentally obtained bubble diameter for isolated bubbles (i.e., bubbles that had no interaction with other bubbles—Eqs. 13 and 14) and its velocities (Eq. 15). However, isolated bubbles included only a limited subset of cases.

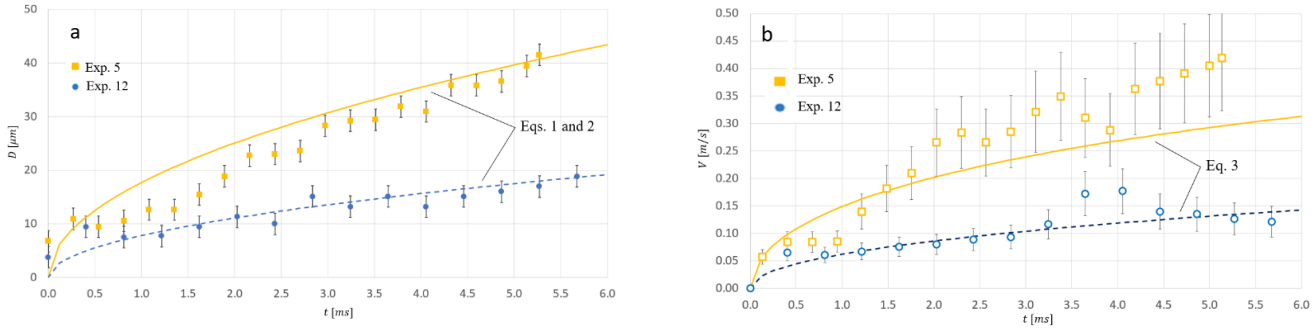

Figure 34- Bubble's diameter (a) and velocity (b) compared to the thermally driven asymptotic solutions [65], [67]. The diameter compared to Eq. 13 and the velocity compared to Eq. 15 for case 5 (P=6.32 MPa, ΔT_{sub}=2.2 K, G=523 kg/m^{2}s, and q″=7.14 W/cm^2 —Yellow square [157].

6.3.4. External identified bubble growth mechanisms

With increasing heat flux, bubble-to-bubble interaction became prevalent, which affected the bubble dynamics. Figure 35 depicts large bubbles that were formed on the preheater upstream of the optical window. While the heat flux was sufficient to maintain their diameter, it was insufficient to further grow them in the main channel due to evaporation. However, other growth mechanisms were observed.

Large bubbles that were formed upstream tended to move faster and swept smaller and slower bubbles near the heated surface along their trajectory, which resulted in bubble growth. Bubble interactions were classified into two categories — bubble aggregation (Fig. 35a) and bubble-to-bubble coalescence (Fig. 35b). Bubble aggregation refers to a large upstream bubble that passed through an area that was densely populated with small nuclei bubbles, which tended to decelerate the bubble (Fig. 35c). A bubble-to-bubble coalescence occurred when two bubbles of a similar size merged into a single larger bubble, which tended to accelerate the bubble (Fig. 35d). In both cases the bubble grew due to the interactions. At high heat fluxes, when significant amount of vapor was generated, these interactions occurred concurrently.

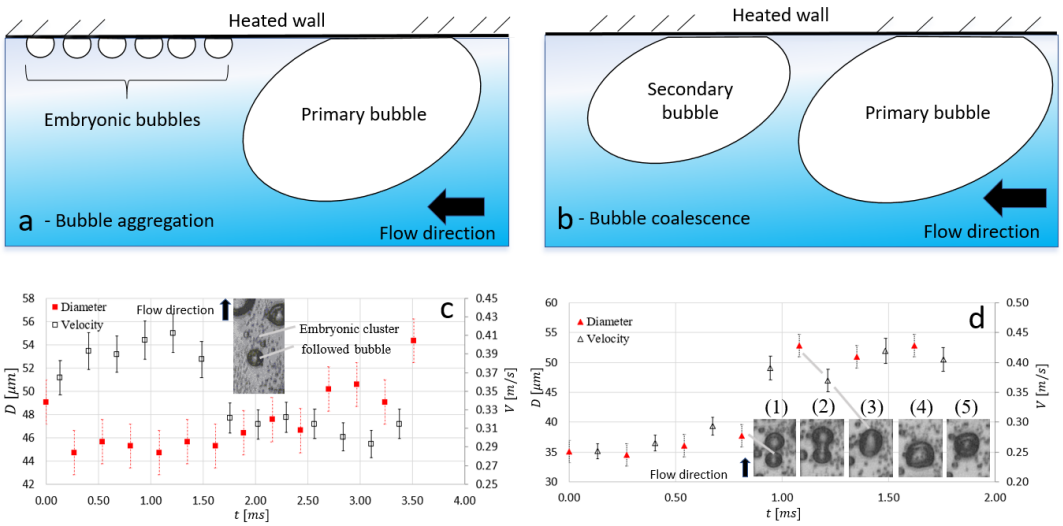

Figure 35 - Two types of bubble-to-bubble interaction. a) A large bubble swept through embryonic bubbles and generates a wake-less region on top of the heater; and b) Two large bubbles merged. c) Decelerating bubble due to presence of embryonic bubbles [157].

For reduced pressures below 0.95, the bubbles maintained their spherical shape, and for reduced pressures above 0.95 they became elongated along the flow direction. In addition, at reduced pressures above 0.95, the bubbles tended to move slower and were more sparsely populated. In some cases, the bubble separated into smaller bubbles and condensed — a phenomenon that was not observed for lower reduced pressures (Fig. 36).

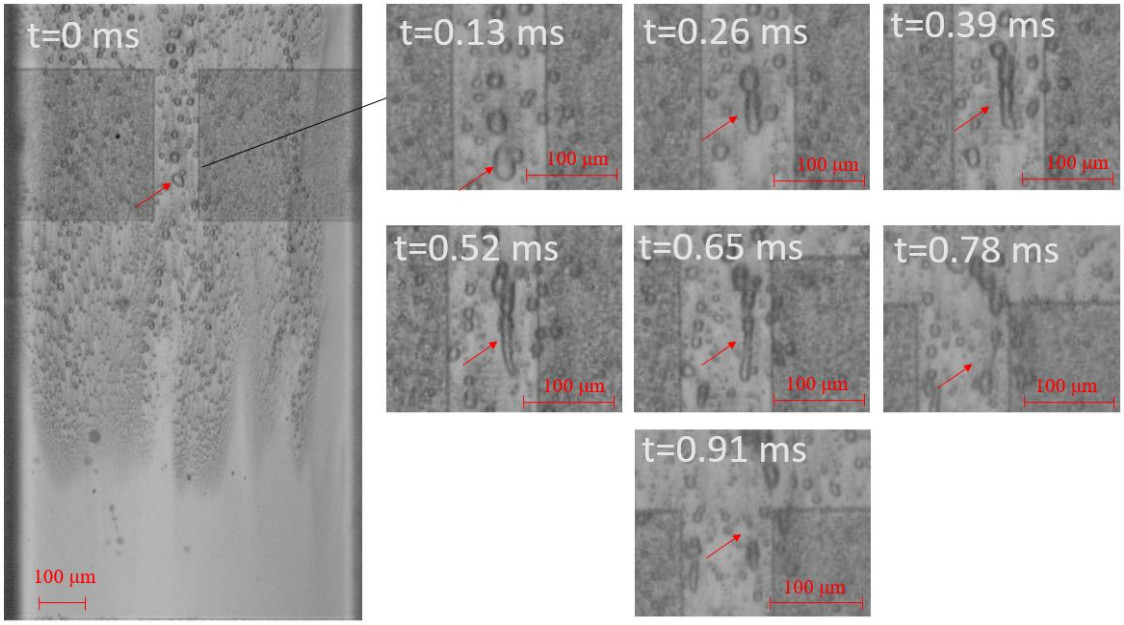

Figure 36 - At reduced pressures above 0.95, the bubbles became elongated and more readily condensed (P=7.19 MPa, ΔT_{sub}=6.9 K, G=469 kg/m^{2}s, and q″=5.2 W/cm^2) [157],

6.3.5. Proposed bubble growth model with bubble interactions

As shown in Fig. 37, the number of active sites increased with heat flux, which produced a slowly propagating nuclei-bubble-blanket that covered most of the heated surface. Measurement of the largest recorded bubble diameter farthest downstream within the optical window showed that the heat flux strongly influenced the bubble diameter. For heat fluxes of 1.4 W/cm^2, 3.3 W/cm^2, 6.6 W/cm^2, 14.2 W/cm^2, the largest bubble diameters were 28 µm, 57 µm, 76 µm, and 97 µm, respectively.

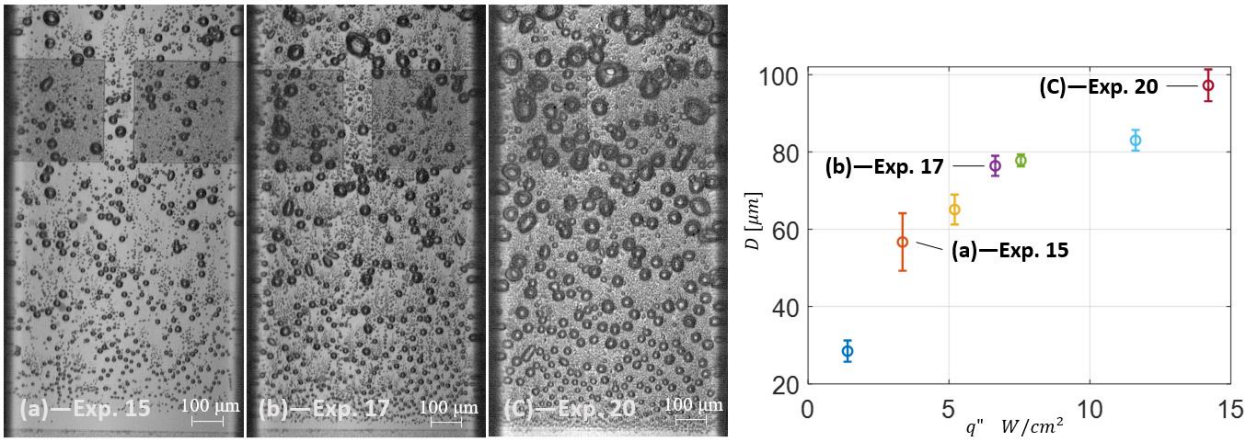

Figure 37- Left side-Images of the flow boiling patterns for Experiments 15, 17, and 20 at table 12. The increase in the heat flux led to higher density of active nuclei sites, which in turn, generated more vapor and larger bubbles. Right side- Vapor generation and the large [157].

Due to a large number of nucleation sites, the bubbles were generated in close proximity to each other, which led to a large number of bubble-to-bubble interactions. To account for the bubble-to-bubble interactions an additional term was added to the thermally controlled bubble growth equation, Eq. 21. Since the effect of bubble-to-bubble interaction was cumulative and was unrelated to phase change considerations, the term was added to Eq. 12 without alteration. The term was empirically correlated using experiments 15 through 20 and verified using experiments 4 thought 12. Several terms were considered and compared (e.g., terms proportional to √t, et, and ln(t)), and it was found that the term a·t best captured the experimental data of each experiment with R^2 fitting values ranging from 0.9 to 0.99 for Experiments 15 to 20, Table 12.

$$D(t) = \frac{4 \cdot \Delta T_{sat} \cdot k_l}{h_{fg} \cdot \rho_g} \cdot \sqrt{\frac{3 \cdot t}{\pi \cdot \alpha_l}} + a \cdot t \tag{21}$$

Table 13— the terms and fitting coefficient for each experiment [157]

Experiment No	$a\times10^{-3}$	$a_{min}\times10^{-3}$	$a_{max}\times10^{-3}$	R^2
15	1.502	0.164	2.840	0.9
16	3.520	1.456	5.583	0.91
17	4.211	2.605	5.817	0.95
18	4.058	2.545	5.57	0.95
19	5.471	4.215	6.727	0.97
20	11.37	9.820	12.902	0.99

Table 13 represents the numerical value of the fitting parameter (i.e., a) and its coefficient of determination (i.e., R^2). The accuracy of the fit was proportional to the heat flux, which suggests that as the interactions between bubbles becomes more rigorous the fitting accuracy improves. The a_{min} and a_{max} values provide the 95% confidence bend as reported by Matlab® curve fitting tool.

Then by trial-and-error, Eq. 21 was formulated. It was found that an exponential formulation of the coefficient had the best fit to the experimental results (i.e., $A_1 \cdot e^{A_2 \cdot \frac{B_O}{(\gamma-1)^2}}$), and since the heat flux influenced the bubble size, the coefficient a should have been a function of the dimensionless Boiling number. On the other hand, the term $(\gamma\text{-}1)^2$ represents the thermodynamic property changes near the critical conditions [90]. Finally, the fitting coefficients A_1 and A_2 were fitted with the Matlab® curve fitting tool and yielded the highest R^2 value (Table 14).

$$a = A_1 \cdot e^{A_2 \cdot \frac{B_O}{(\gamma-1)^2}} \tag{22}$$

where $Bo = q \cdot G/h_{fg}$ is the boiling number and γ is the specific heat ratio (Cp/Cv).

Table 14- Coefficients A_1 and A_2 in Eq. 22 that were fitted to obtain coefficient a in Eq 21.

	Nominal	Minimal	maximal	R^2
$A_1\times10^{-3}$	1.705	0.558	2.851	0.92
A_2	896.3	516.9	1276	

6.3.6. Verification of the proposed model

Verification was done through Experiments 4 to 12 (Table 12). For Experiment 4, the optical window was positioned between RTD_1 and RTD_2, which set it farthest downstream compared to remaining experiments, and therefore, the bubbles had more time to evolve compared to the other cases, Fig. 38. Since the bubbles were the largest identified at the specific cross-section, a reasonable assumption was that the bubbles originated at the heater's leading edge and propagated 2.5 mm downstream. The thermally driven model with Poiseuille flow profile (i.e., Eqs. 13 through 16) underpredicted the measured results with an MDE of 31.7 µm compared to an MDE of 6 µm for the model that accounts for bubble-to-bubble interactions. For Experiment 4, Eq. 21, which accounts for bubble-to-bubble interactions, presented significant improvement. This is believed to be because the experiment had significant heat flux (i.e., 12.2 W/cm^2), which led to considerable vapor generation and rigorous bubble-to-bubble interactions that contributed to the bubbles' growth, and because the measurements were taken farthest downstream giving them sufficient time to interact and grow.

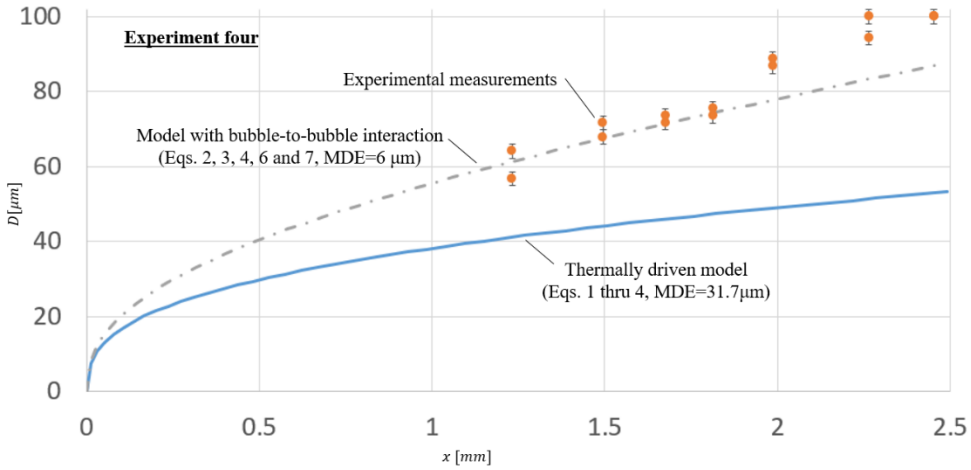

Figure 38- Thermally driven bubble growth with and without accounting for bubble-to-bubble interactions.

With the proposed model modification, the MDE was reduced from 31.7 µm to 6 µm, corresponding to a reduction of 81% [157].

Figure 39 presents the MDE for Experiments 4 through 12. For to the original thermally driven solution (Eqs. 1 through 4) the MDE was 13.5 μm, while for the model that accounted for the bubble-to-bubble interactions the MDE was reduced to 6.6 μm — a decrease of 51%. The lowest reduction was observed for Experiment 9 (i.e., from 7.6 μm to 5.9 μm), which is attributed to the relatively low heat flux (i.e., 4.2 W/cm^2), corresponding to limited bubble-to-bubble interactions.

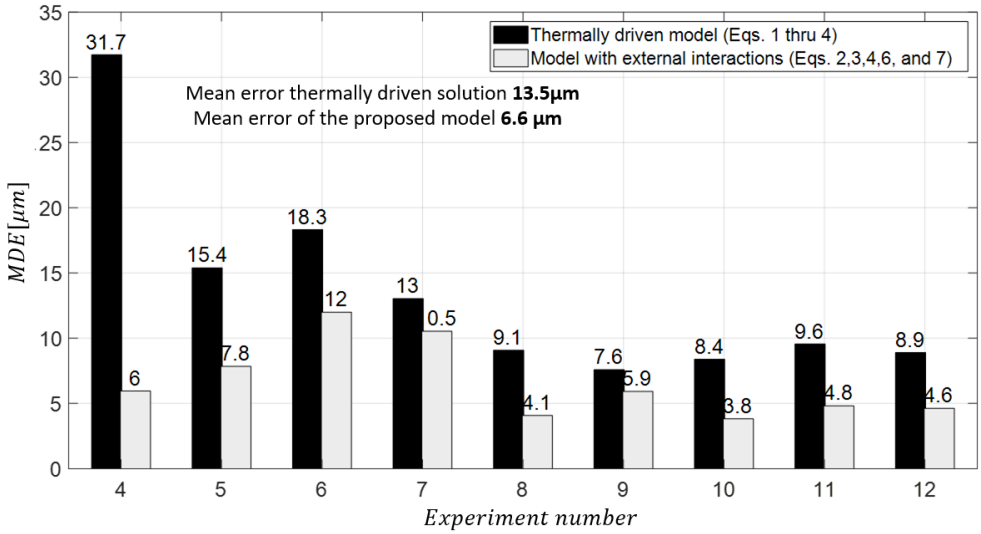

Figure 39- MDE for all experiments. The average MDE reduced from 13.5 μm to 6.6 μm — a reduction of 51% [157].

The critical point is characterized by a discontinuity in the derivatives of the thermodynamic properties [170]. Thus, the specific heat ratio, which is inversely proportional to the coefficient 'a', asymptotically diminished as the pressure approached the critical value. The experimental observation indicated that near the critical condition, the bubble size decreased, and the reduction in the coefficient 'a' was consistent with experimental observation.

6.4. Adiabatic Thermalization-The piston effect

Visual images, local surface temperature, and pressure of flow boiling of CO_2 at reduced pressures ($P_r=P/P_c$) between 0.86 and 0.99 were studied at this section of the research. The parameters for each

experiment are summarized in Table 15 and include: reduced pressure (P_r), inlet temperature (T_0), reduced inlet temperature ($T_r=T_0/T_c$), saturation temperature (T_{sat}), mass flux (G), heat flux (q''), and the returned light intensity ratio (I_{T_0}/I_T). The critical pressure, temperature, and density that were used in the current study were taken from Span and Wagner [171] and equaled to 7.3773 MPa, 304.13 K, and 467.6 kg/m$^{3.}$

Table 15- List of experiments and their conditions for the adiabatic thermalization study [172].

No.	P_r	T_0 (K)	T_r	T_{sat} (K)	G (kg·m^{-2}s^{-1})	q″ (W·cm^{-2})	I_{T_0}/I_T
1	0.86	296.2	0.978	297.42	523.00	7.14	1.32
2	0.88	296.24	0.982	298.69	280.00	4.20	1.33
3	0.90	295.67	0.984	299.28	484.30	6.88	1.26
4	0.91	295.73	0.986	300.01	547.51	6.66	1.62
5	0.91	296.0	0.986	299.90	413.00	5.13	1.51
6	0.95	296.6	0.993	301.9	712.00	12.50	1.62
7	0.98	296.36	0.997	303.1	474.00	9.20	1.64
8	0.99	296.46	0.998	303.57	464.88	6.75	1.5

6.4.1. Flow boiling patterns

Two distinct boiling patterns were observed, depending on the reduced pressure of the fluid. For reduced pressures below 0.95, a pattern of nuclei bubbles with diameters ranging from 2 μm to 5 μm formed on the heated surface. The bubbles propagated downstream and expanded up to a diameter of ~50 μm. The bubbles also maintained a spherical shape and formed a vapor-less region in their wake as they moved downstream with a distinct and well-defined vapor-liquid boundary, see Fig. 40a. For reduced pressures above 0.95, the nuclei sites produced bubbles smaller than 2 μm that were more densely populated and moved slower downstream forming a dusky blanket on the heated surface that eventually grew into elongated streaks. The

vapor-liquid boundary of the streaks was blur, and no discontinuity in the dusky blanket or presence of vapor-less area upstream were observed, see Fig. 40b. The blurring process of the vapor-liquid boundary layer and the deviation from a spherical shape was due to the reduction in the surface tension of the vapor-liquid interface, making the bubbles more deformable [157], [173]. Supplementary Fig. 1 presents the remaining flow pattern that were observed.

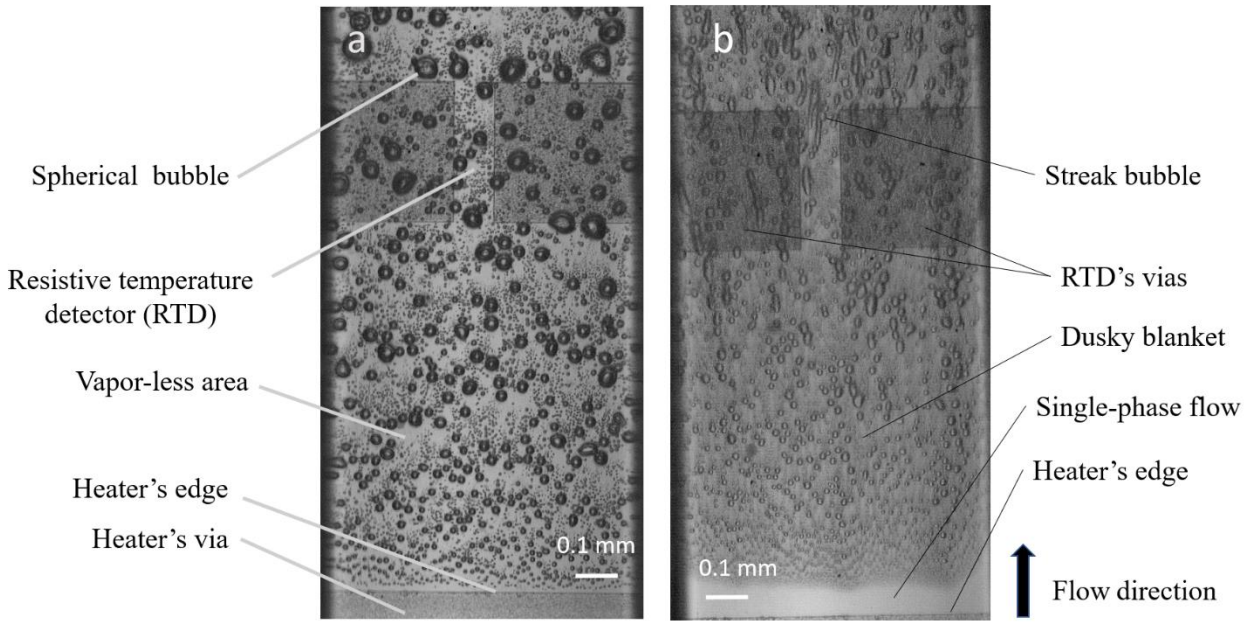

Figure 40 - Shift in flow pattern as the reduced pressure approaches unity: a) At reduced pressures below 0.95, nuclei bubbles with an initial diameter of 2 μm to 5 μm formed and gradually grew to diameter of ~50 μm (shown: Pr=0.86, G=523 kg/m^{2}s, and q″=7.14 W/cm^2) as they propagated downstream. As the bubble grew, they formed vapor-less regions in their wake. b) At reduced pressures above 0.95, a bi-pattern composed of vapor streaks above the heater and small ~2 μm nuclei bubbles, which formed inside a distinct dusky layer below the heater was observed (shown: Pr=0.98, G=474 kg/m^{2}s, and q″=9.2 W/cm^2). Vapor downstream propagation was considerably slower compared to lower pressures. The change in the bubble shape and pattern is clearly visible and is consistent with the theory of near-critical fluid [172], [173].

Liquid CO_2 reached the heater with subcooled temperatures ranging from 7.61 K to 1.37 K, depending on the operational pressure. As the system pressure approached the critical condition, the void fraction, i.e., the fraction of the channel cross-sectional area occupied by the gas phase, decreased, as shown in Fig. 41a. Since the bubble ebullition process is associated with vaporization, a process that requires a large amount of heat transfer for the liquid-to-vapor phase change process, and flow mixing, which brakes the boundary layer and drives the hot fluid away from the heated surface, a reduced void fraction leads to a lower heat transfer coefficient [119]. Furthermore, the latent heat of vaporization, h_{fg}, diminishes with increasing pressure [161], and thus, the potential to enhance heat transfer due to the liquid-to-vapor phase change is expected to diminish with pressure. As shown in Fig. 41b, the heat transfer coefficient (HTC), experimentally obtained by Parahovnik et al. [64] and by the correlation of Cheng et al. [1], suggest otherwise. Finally, the single-phase flow regime pertinent to the experimental conditions was laminar, and since all the bubbles translated solely along the main flow direction with no transverse movement, it was concluded that bubble formation did not steer the flow. Therefore, it was assumed that the bubble ebullition process contribution to heat transfer was mainly due to vaporization and not mixing. For further analysis, it was assumed that three heat transfer mechanisms (i.e., incompressible single-phase, vaporization, and adiabatic thermalization) can be decoupled and should be analyzed separately. In the following sections, it is shown that this increase is directly related to the piston effect.

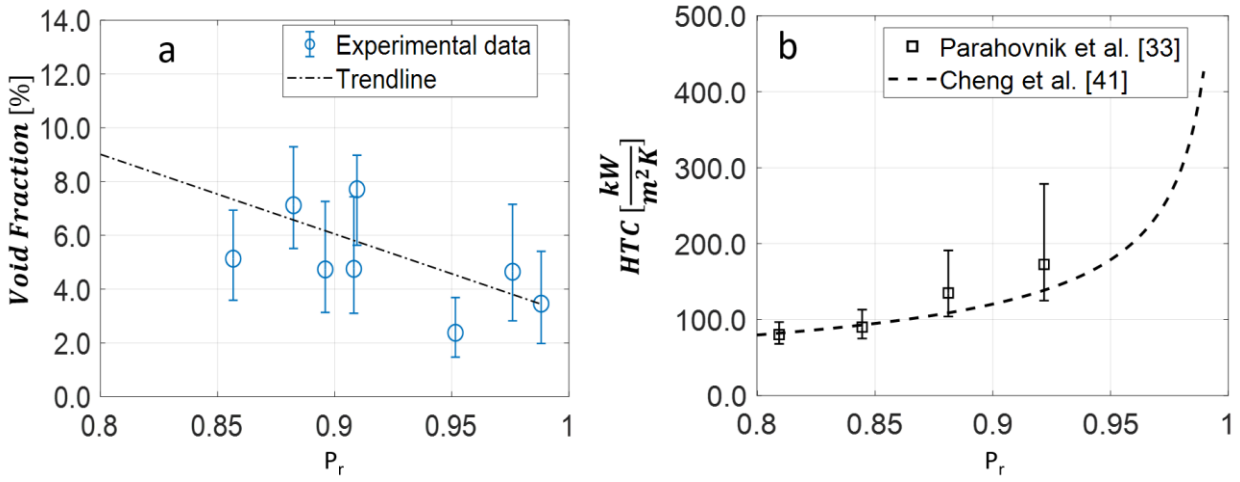

Figure 41 - Vapor fraction and heat transfer coefficient trends as the reduced pressure approached unity. a) The void fraction decreased with reduced pressure, while b) the heat transfer coefficient increased [172].

6.4.2. Opalescence measurements of the fluid.

The increase in the fluid's bulk temperature was quantified through critical opalescence measurements of the bulk liquid temperature [170], [174]–[179]. When the fluid's temperature approaches the critical condition, intermolecular fluctuations lead to higher light scattering, which promotes fluid's opaqueness [176]. During experiment, the microchannel was illuminated and the reflected light was captured and quantified by the camera. The ratio between the scattered to the light induced by the illuminator, and its relation to the fluid's state is quantified by Eq. 23 [178], [179].

$$R = \frac{I_i - I}{I_i} \tag{23a}$$

$$R = f \cdot T \cdot \beta \cdot \left(\rho \cdot \frac{\partial \varepsilon}{\partial \rho}\right)_T^2 \tag{23b}$$

Where R is the ratio of the scattered to the induced light, f is a multiplication factor encompassing the light wavelength and geometrical properties [178], [179], I_i is the induced light intensity, I is the reflected light

intensity , T is the fluid's temperature, β is the isothermal compressibility, ε is the dielectric constant, ρ is the density, and the term $(\rho \cdot \partial\varepsilon/\partial\rho)_{\mathrm{T}}^{2}$ is given by Einstein [180].

The scattering ratios due to critical opalescence are considerably lower than unity [181], and the expected temperature differences were low due to boiling inception. A relation between the fluid's temperature and the returned light intensity ratio was formulated according to Eq. 24. (For additional details see 'Derivation of the returned light intensity ratios and fluid temperature relation' in Appendix B.)

$$\frac{I_{T_0}}{I_T} = \frac{R_T}{R_{T_0}} = \frac{f \cdot T \cdot \beta_T \cdot \left(\rho \cdot \frac{\partial \varepsilon}{\partial \rho}\right)_T^2}{f \cdot T_0 \cdot \beta_{T_0} \cdot \left(\rho \cdot \frac{\partial \varepsilon}{\partial \rho}\right)_{T_0}^2} = \frac{T \cdot \beta_T \cdot \left(\rho \cdot \frac{\partial \varepsilon}{\partial \rho}\right)_T^2}{T_0 \cdot \beta_{T_0} \cdot \left(\rho \cdot \frac{\partial \varepsilon}{\partial \rho}\right)_0^2} \tag{24}$$

The coefficient f is required to obtain the absolute temperature based on CO2 turbidity measurements. However, the light source (non-coherent, white light), the experimental setup (the camera, the microscope, and the lens) and the microchannel were the same and the data was acquired simultaneously. Therefore, the factor f was canceled out, and through inlet temperature (T_0) measurements, the temperature T was calculated. The returned light intensity ratios were measured by converting the camera images to bitmap image files. (The stronger the returned light intensity is, the higher the pixel's numerical value at a specific location.) Subsequently, the returned light intensity profile was calculated by averaging its values perpendicular to the flow excluding the influence of the bubbles. The returned light intensity at the inlet temperature (i.e., I_{T_0} where T_0 is the inlet temperature) of the fluid was sampled close to the heater's edge before boiling inception. The downstream returned light intensity (i.e., I_T where the subscript T stands for the hotter temperature) was tested before the resistive temperature detector's (RTD's) vias at 0.9 mm from the heater's edge to avoid background interference, see Fig. 42. For reduced pressures below 0.95, the fluctuations of the returned light intensity data were considerable while for reduced pressures above 0.95, the blurring of bubble appeared to moderate the noise from the returned light signal. Intensity measurements

of all the discussed cases are provided in the supplementary materials in a section titled ‘Measurements of the returned light intensity ratio.

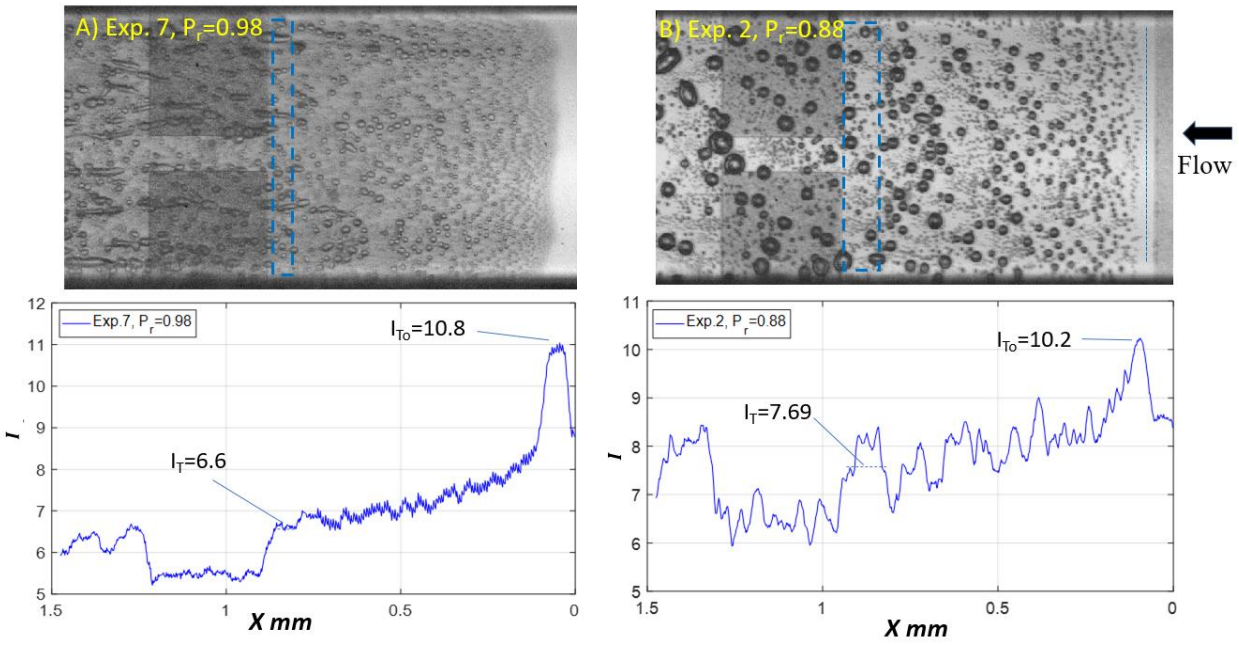

Figure 42 - Returned light intensity along the flow direction. The intensity of the returned light (I) was calculated as an average of the local intensities of the cross-section. The returned light intensity at the inlet temperature (I_{To}) was sampled as close as possible to the heaters via. The returned light intensity at the downstream temperature was sampled before the RTD’s vias to maintain similar background. The mean returned light intensity of the cross-section dropped as the flow was heated. The bubbles were expressed as variations from the mean returned light intensity value. As the reduced pressure approached unity, these variations were reduced to moderate signal noise [172].

The fluid inlet temperature, T_0, was measured using a thermocouple that was externally integrated into the experimental setup. Since no preheating was applied, the fluid was in thermal equilibrium with the thermocouple. The Span and Wagner equation of state [171] with the aid of NIST REFPROP® [161] software were used to calculate the isothermal compressibility, β_T and β_{T_0}. The two terms, $(\rho \cdot \partial\varepsilon/\partial\rho)_T^2$

and $(\rho \cdot \partial\varepsilon/\partial\rho)^2_{T_0}$, were calculated through the equation proposed by Eykman [182], which was an empirical relation that links the $(\rho \cdot \partial\varepsilon/\partial\rho)^2$ term to the fluid's refractive index, n, see Eq. 25.

$$\left(\rho \cdot \frac{\partial\varepsilon}{\partial\rho}\right)_T = \frac{2 \cdot n \cdot (n+0.4) \cdot (n^2-1)}{n^2+0.8 \cdot n+1} \tag{25}$$

Carbon dioxide's refractive index, n, was measured by Moriyoshi et al. [183], and it was found that it depends on both the temperature and the pressure. The reflective index was interpolated to the experimental pressure and temperature. Figure 43 is constructed using the following logic. Initially, the term $T_0 \cdot \beta_{T_0} \cdot \left(\rho \cdot \frac{\partial\varepsilon}{\partial\rho}\right)^2_{\mathrm{T0}}$ was calculated for inlet temperature (i.e., T_0) and operational pressure. The term $T \cdot \beta_T \cdot \left(\rho \cdot \frac{\partial\varepsilon}{\partial\rho}\right)^2_T$ was then calculated for steps of 0.01 K until the saturation temperature.

Figure 43 depicts the ratio of the light scattering ratio (i.e., R_T/R_{T_0}) as a function of temperature difference (i.e., $\Delta T_R = T - T_0$) from 0 K to 6 K for Case 8, see Table 15. By comparing the detected light intensity ratio (i.e., I_{T_0}/I_T) with the light scattering ratio (i.e., R_T/R_{T_0}), the temperature difference was inferred. This temperature difference corresponded to the increase in the fluid temperature that was measured through the critical opalescence effect.

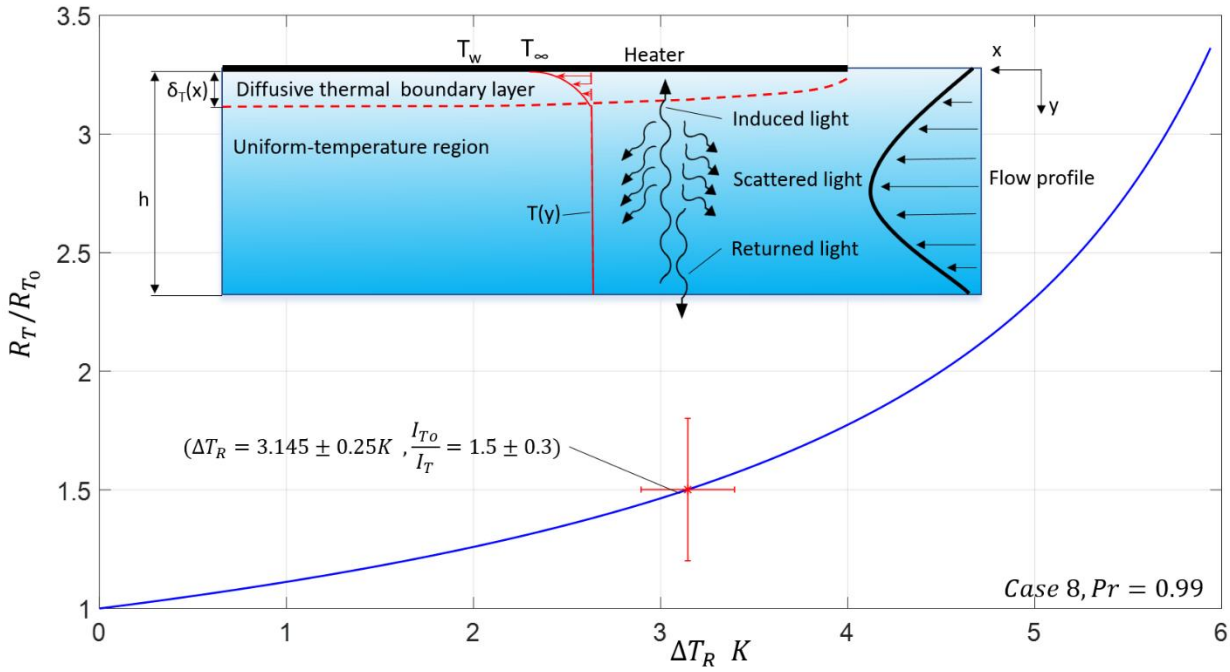

Figure 43 - Calculation of the increase in temperature according to returned light density measurements**.** The scattering ratio (R/R_{To}) as a function of the bulk temperature increase (ΔT_R) at a reduced pressure of 0.99. The theoretical curve obtained from Eq. 24 corresponds to a measured value of 1.5 at a temperature rise of 3.145 K [172].

The diffusive boundary layer theory [184], [185] proposed mathematical formulation for hydrodynamic and thermal boundary layers that are formed over a submerged body in a fully developed flow filed. The theory is also valid for boundary layers in fluids flowing inside channels. According to the theory, at the edge of the boundary layer (i.e., Eq. 28), the dimensionless temperature is within 1% of the fluid's inlet temperature (T_{wall}-T_{fluid})/(T_{wall}-T_{inlet})=0.99), which implies negligible heat transfer outside the boundary layer. The thermal boundary layer height was calculated using Eq. 28 and was predicted to range from 8.8 μm to 13.2 μm, see insert in Fig. 43. (See additional samples in Appendix B, 'Inferring the bulk fluid temperature.') Therefore, the region with uniform temperature (i.e., outside the thermal boundary layer) corresponded to 86.8%-91.2% of the channel's volume. Thus, about ~90% of the light scattering took place in a region of uniform temperature, suggesting that the optical signature that reached the camera mostly

reflected the changes in the fluid's bulk temperature. Hence, the fluid's bulk temperature, rather than the diffusive boundary layer temperature, was sampled.

6.4.3. Calculation of the downstream bulk temperature with the piston effect

The piston effect is a thermalization mode that transfers heat outside the diffusive boundary layer. The temperature increase (ΔT_p) outside the diffusive boundary layer due to the piston effect was formulated by Onuki et al. [113]:

$$\Delta T_p = (\gamma - 1) \cdot \frac{V_1}{V_1 + V_2} \cdot \Delta T_{diff} \tag{26}$$

Where ΔT_{diff} is the temperature difference between the diffusive thermal boundary layer temperature and the inlet temperature, γ is the ratio of the specific heat at constant pressure to specific heat at constant volume, V_1 is the volume of the diffusive boundary layer (i.e., a volume with a depth of $\delta_T(x)$), and V_2 is the remaining fluid volume (i.e., a volume with a depth of $h-\delta_T(x)$, where h is the channel height), see Fig. 43. Since the width and length of V_1 and V_2 were the same, they were canceled out, making the volume ratio equal to $\delta_T(x)/h$. For subcooled boiling, it is reasonable to assume that the temperature within the boundary layer corresponded to the fluid's saturation temperature (T_{sat}) [119], while the fluid temperature outside the boundary layer corresponds to the inlet temperature (T_0). Therefore, ΔT_{diff} in Eq. 26 was reformulated as the difference between the saturation temperature and the inlet temperature (i.e., $\Delta T_{diff} = \Delta T_{sub} = T_{sat} - T_0$). Consequently, the temperature increase due to the piston effect was determined by the following equation:

$$\Delta T_p = (\gamma - 1) \cdot \frac{\delta_T(x)}{h} \cdot \Delta T_{sub} \tag{27}$$

Since the flow was laminar, the temperature distribution was calculated through the boundary layer theory, and was a function of the Prandtl number, the Reynolds number, and the distance from the edge of the heater. The diffusive boundary layer theory [184], [185] suggests that heat is only transferred within the boundary layer. However, because of the piston effect it is postulated that heat was also being transferred outside the boundary layer. As such, the piston effect alleviates the heat load inside the boundary layer and was responsible for enhanced heat transfer of near-critical fluids. The thermal boundary layer thickness, $\delta_T(x)$, was determined according to [185]:

$$\delta_T(x) = x/\sqrt{(Cp_l \cdot D_h \cdot G/\kappa)} \quad (28),$$

where x is the distance from the leading edge of the heater (i.e., x=0.9 mm), Cp_l is the specific heat at constant pressure, D_h is the hydraulic diameter of the channel (i.e., D_h=0.31 mm), and k is the thermal conductivity of the fluid at the inlet temperature and pressure. The Span and Wagner equation of state [171] with the aid of NIST REFPROP® [161] software was used to calculate the specific heat and thermal conductivity.

Figure 44 depicts the experimentally measured increase in the bulk fluid temperature obtained through the returned light intensity ratio (i.e., ΔT_R) and the increase in the bulk fluid temperature due to the piston effect (i.e., ΔT_P). The uncertainties of ΔT_P originated from the pressure, mass flux, and temperature measurements described in the method section. Besides the uncertainty of ΔT_R, the uncertainty of the reflected light intensity ratio was also considered. The measured bulk temperature increase (i.e., ΔT_R), and the temperature raise due to the piston effect (i.e., ΔT_P) were lower than the maximum possible temperature increase, which was reached when the bulk fluid attained the saturation temperature (i.e., ΔT_{sub}), see fig. 44. Finally, the mean average error between ΔT_R and ΔT_P was calculated to be 35%, providing sufficient confidence that the fluid's bulk temperature outside the boundary layer increased mainly due to the piston effect.

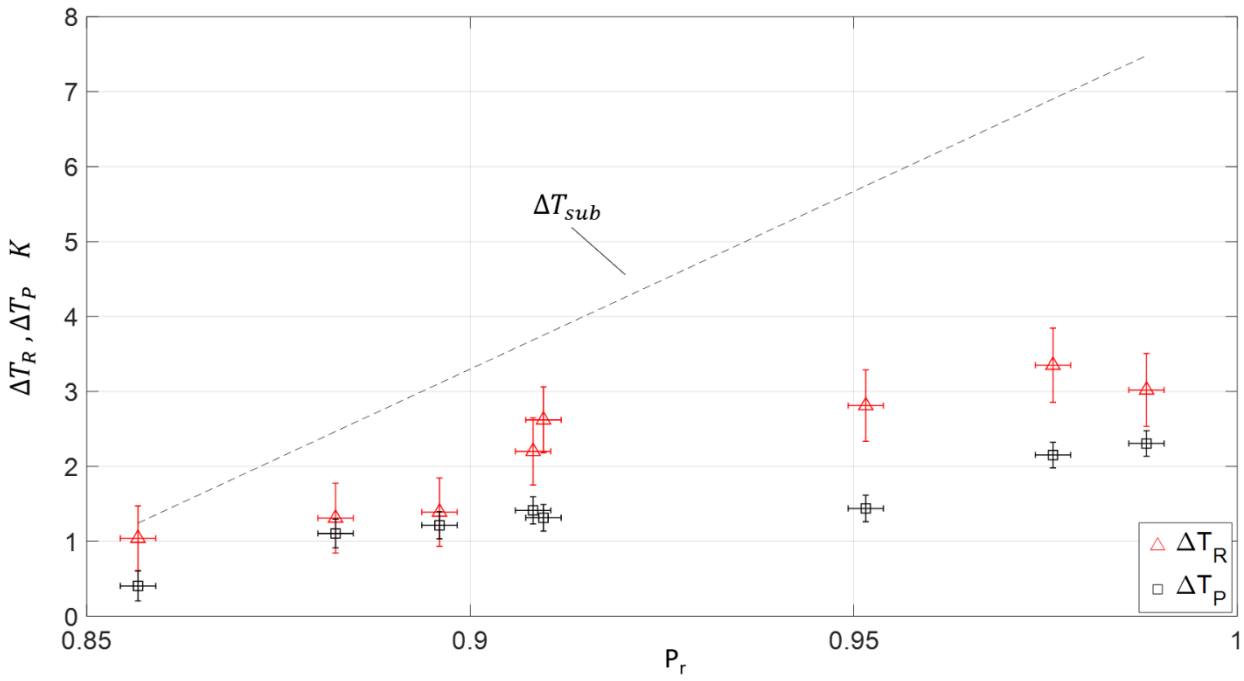

Figure 44 - Increase in bulk's fluid temperature through the piston effect analysis (ΔT_P) [113] and through critical opalescence measurements (ΔT_R). The mean average error between ΔT_R and ΔT_P was 35% provided sufficient confidence that the fluid's bulk temperature outside the boundary layer increased mainly due to the piston effect [172].

6.4.4. The relative importance of thermal transport due to the piston effect

For a near-critical fluid, heat transfer is a result of three main processes consisting of convective (E_c), vaporization (E_v), and adiabatic thermalization (E_p). To quantify the shift in the thermalization modes the heat transfer per unit mas (i.e., kJ/kg) was formulated according to:

$$E_T = E_c + E_v + E_p \tag{29}$$

Where E_T is the total heat transferred per unit mass. (Note that radiation heat transfer was neglected as the temperatures were sufficiently low.)

The piston effect is given by [113], [114], [186]:

$$E_p = Cp_l \cdot \Delta T_p \tag{29a}$$

The other modes were calculated according to:

$$E_c = C_{P_l} \cdot \Delta T_{sub} \tag{29b}$$

$$E_v = h_{fg} \tag{29c}$$

where ΔT_{sub} is the temperature difference between the saturation and inlet temperatures, h_{fg} is the latent heat of evaporation. While convective heat transfer and boiling heat transfer (i.e., vaporization) occur within the diffusive boundary layer adjacent to the heater, the piston effect transmits the thermal energy directly into the fluid's bulk, bypassing the diffusive boundary layer.

Figure. 45 shows the decomposition of the heat transfer components for CO_2 at an inlet temperature of 296 K and reduced pressures ranging from 0.86 up to 0.99. As the enthalpy of vaporization diminished as the fluid approached the critical conditions so did the contribution of vaporization to the total heat transfer. The increase in convective heat transfer with pressure was negligible relative to the change in the other heat transfer modes and occurred due to the rise of T_{sat} that in turn increased ΔT_{sub}. The heat transfer due to the piston effect increased significantly and had the strongest effect on the fluid's ability to carry heat with increasing pressure. The significant increase in the contribution of the piston effect was due to a very large growth of the specific heats ratio (γ) — a typical behavior of a second-order phase transition of fluids [170]. For reduced pressure of 0.86, the heat transfer rate per unit mass flow rate due to convective, vaporization, and the piston effects were equal to 7.6 kJ/kg, 123.4 kJ/kg, and 5.9 kJ/kg, corresponding to 5.6%, 90.1%, and 4.3% of the total heat, respectively. The relative importance of these effects changed drastically at a reduced pressure of 0.99, and were equal to 27.6 kJ/kg, 46 kJ/kg, and 254.4 kJ/kg, corresponding to 8.4%, 14%, and 77.6% of the total heat transfer, respectively. The increased total heat transfer was consistent with enhanced heat transfer coefficient at higher pressures shown in Fig. 41b.

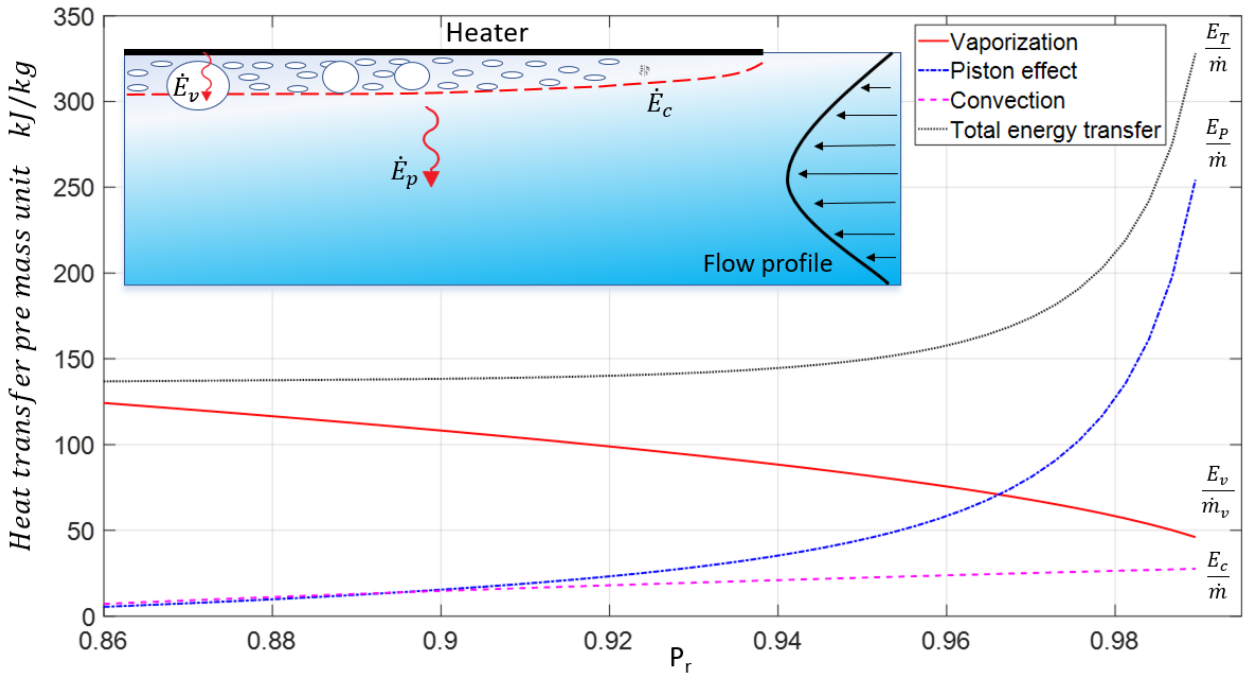

Figure 45 - Transition of heat transfer modes towards adiabatic thermalization (i.e., piston effect). The total heat transfer per mass unit ($\frac{E_T}{\dot{m}}$, dotted black curve), the vaporization heat transfer per mass unit ($\frac{E_v}{\dot{m}_v}$, bold red curve), the convective heat transfer per mass unit ($\frac{E_c}{\dot{m}}$, dashed blue curve), and the heat transfer due to the piston effect per mass unit ($\frac{E_P}{\dot{m}}$, pink dashed line). The heat transfer mechanism shifted from evaporation (90.1% to 14% for reduced pressure of 0.86 and 0.99, respectively) to the adiabatic thermalization (4.3% to 77.6% for reduced pressure of 0.86 and 0.99, respectively). While convective heat transfer maintained a relatively constant portion of the total heat transfer (5.6% to 8.4% for reduced pressure of 0.86 and 0.99, respectively). The increased total heat transfer was consistent with the enhanced heat transfer coefficient at higher pressures shown in Fig. 41b [172].

6.5. Pssure drop and Joule-Thomson effect

The pressure drop across the orifice and the associate JT effect were leveraged to conduct saturated flow boiling experiments at temperatures below room temperature without insulating the entire experimental setup. The orifice had a hydraulic diameter of 0.081 mm, and a length of 1.8 mm, see Fig. 46.

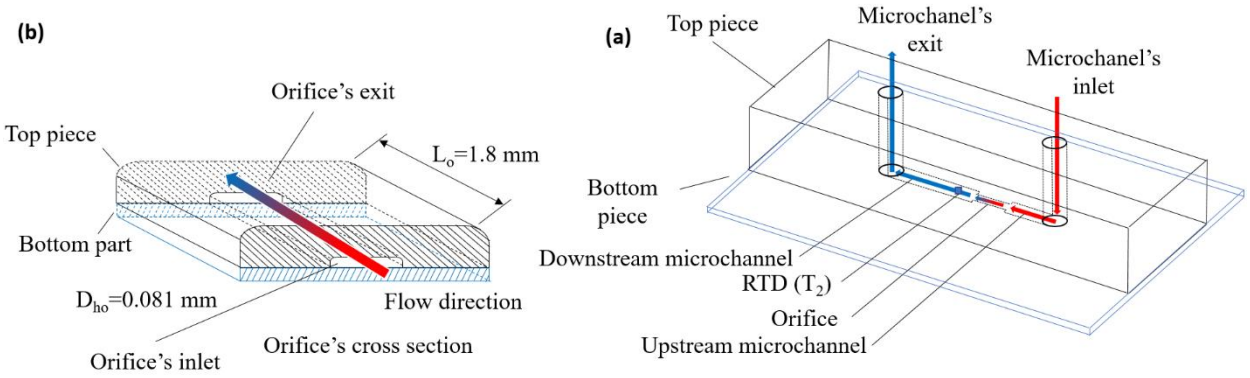

Figure 46 – micro-orifices sketch and terminology for this section [187].

Figure 47 depicts a *P-v* diagram and a *T-s* diagram along with the experimental data points. The pressure at the inlet was estimated through the pressure measured by the inlet transducer (i.e., P_{in}) minus the estimated losses of the components upstream the orifice. The pressure at the orifice exit (Fig. 46) was calculated by adding the predicted losses downstream the orifice exit to the reading from the exit pressure transducer. The inlet temperature was measured by the thermocouple attached to the inlet of the package, and the temperature at the exit was measured by the *RTD*, which was 921 µm downstream the orifice's exit. The experimental data consisted of 81 data points with an inlet pressure that ranged from 5.6 MPa to 10.2 MPa, an inlet temperature from 293 K to 314 K, and a mass flux from 47,277 to 162,101 kg/m^{2}s. The phases at the inlet varied and included liquid only, vapor only, and supercritical fluid. The liquid only inlet experiments were carried out at a temperature of about 293 K and are presented as a dense cluster of red

and blue dots on the *T-s* diagram. Some of the experiments with liquid only inlet, exited the orifice as a two-phase mixture. The majority of the supercritical inlet conditions produced significant pressure and temperature drops. The supercritical inlet condition presented the highest pressure drop with the lowest recorded exit pressure and temperature of 2.45 MPa and 262.3 K, respectively.

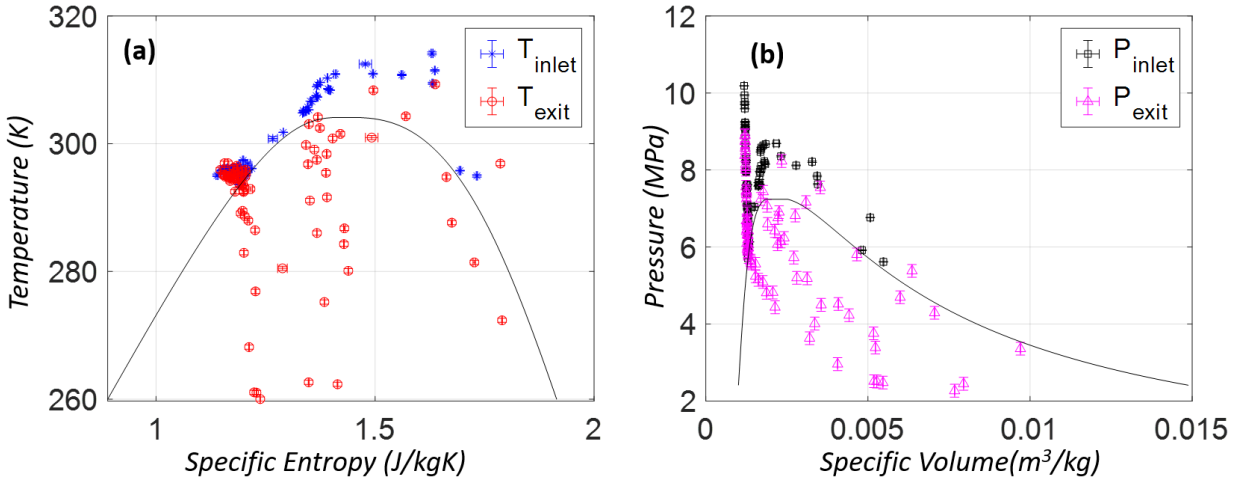

Figure 47-(a)T-s diagram with the inlet and exit temperatures (b) P-v diagram with the inlet and exit pressures. The liquid only inlet experiments were carried out at a temperature of about 293 K and are presented as a dense cluster of red and blue dots on the T-s diagram. The exit data points located inside the two-phase regions varied from saturated liquid to saturated vapor. Some experiments, which are located on the right side of the two-phase region correspond to superheated vapor [187].

6.5.1. Pressure drop

As shown in Fig. 48, the inlet pressure, inlet temperature, and mass flux affected the pressure drop. With increasing mass flux, the range of pressure drop increased because the flow changed states inside the orifice. For an inlet temperature below 301 K, the flow at the exit was mainly liquid or pressurized liquid, and the high density of the liquid resulted in low pressure drops. For an inlet temperature above 301 K, the flow was mainly at high mass quality vapor or supercritical state and most of the experiments resulted in liquid-vapor two-phase flow at the exit of the orifice, which prompted high pressure drops. To clarify this difference, Fig. 48c shows that for experiments with an inlet pressure between 7 MPa and 8 MPa and an

inlet temperature below and above 301 K, a pressure drop below 2 MPa was observed with a week dependency on the mass flux. For an inlet temperature above 301 K, the pressure drop was strongly dependent on the mass flux ─ higher mass flux resulted in an increased pressure drop.

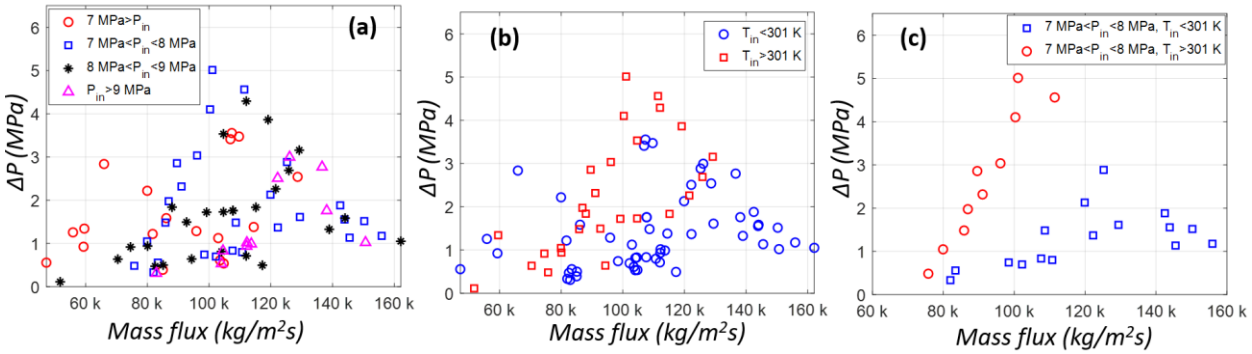

Figure 48- Pressure drop as a function of mass flux, divided to categories by inlet pressure (a), or by inlet temperatures (b). (c) For liquid or pressurized liquid the pressure drop was a weak function of the mass flux (blue squares). For supercritical and vapor phase the pressure drop was strongly dependent on the mass flux (red circles) [187].

6.5.2. Joule-Thomson expansion coefficient

Convective heat transfer in the orifice was evaluated by Newton's law of cooling [137], where the heat transfer coefficient was calculated using the Dittos-Boelter equation [137] for a Reynolds number ranging from 5.4×10^4 to 3.7×10^5. It was found that the added heat (i.e., heat gain) marginally increased the fluid's enthalpy by a maximum value of 0.361 kJ/kg, and therefore, the throttling process was assumed to be isenthalpic. The average experimental Joule-Thomson coefficient was inferred by dividing the total temperature difference across the orifice by the corresponding total pressure drop:

$$JT_h = \frac{T_{inlet} - T_{exit}}{P_{inlet} - P_{exit}}. \quad (30)$$

The experimentally obtained JT_h ranged from about 0.6 K/MPa to about 10 K/MPa, which is consistent with Kazemifar et al. [24] measurement of near-critical CO_2 who obtained a JT_h ranging from about 2 K/MPa to about 8 K/MPa.

Figure 49 presents the measured and predicted JT_h for sub-critical inlet liquid, subcritical inlet vapor, and supercritical inlet temperatures. For an inlet fluid temperature of 296 K, the JT_h predictions from the Span and Wagner [11] and the Wang et al. [162] agreed well with each other and with the experimental results. The sharp drop from about 10 K/MPa to ~2 K/MPa corresponded to a change from a vapor phase to a liquid phase, suggesting that for vapor the JT_h coefficient is much larger than for liquid.

The experimental results shown in Fig. 49 were divided into two groups ― one for the two-phase mixture at the exit (the blue circles) and one for liquid only at the exit (the black squares). For a liquid exit, the JT_h was low and approached zero with increasing inlet pressure. Although the JT_h was slightly negative for three data points, they were assumed to be outliers due to parasitic heat gains in the microchannel's section. As the exit two-phase mixture flow approached saturated vapor conditions, the JT_h increased to about 10 K/MPa. The lower JT_h values for inlet pressures ranging from 6.9 MPa to 7.6 MPa corresponded to an exit mass quality of up to 0.1, while the higher values corresponded to higher mass qualities. The experimental results suggested a more gradual transition of the JT_h coefficient compared to those predicted by the models. Such transition indicated that the JT_h is a strong function of the exit mass quality.

For an inlet temperature above the critical temperature, the Wang et al. [162] model and the Span and Wagner equation [11] were inconsistent. The Wang et al. [162] predicted significant drop in the JT_h with increasing inlet pressure (from 9 K/MPa to about 0.8 K/MPa), while the Span and Wagner equation [11] predicted a more moderate drop (from 9.1 K/MPa to about 2.6 K/MPa) and better predicted experiments. The experimental results indicate a smaller reduction in the JT_h coefficient for inlet temperatures above the critical temperature (e.g., the JT_h dropped from about 10 K/MPa for an inlet pressure of 6.8 MPa to 4.9 K/MPa for 8.6 MPa) and no influence of the exit phase condition (i.e., single-phase exit or two-phase exit had similar JT_h values). For an inlet temperature of T=296 K the MAE was 1.4 K/MPa for both models

and for an inlet temperature of 307 K the MAE was 2.4 K/MPa and 5.4 K/MPa for the Span and Wagner [11] and the Wang et al. [162] models, respectively.

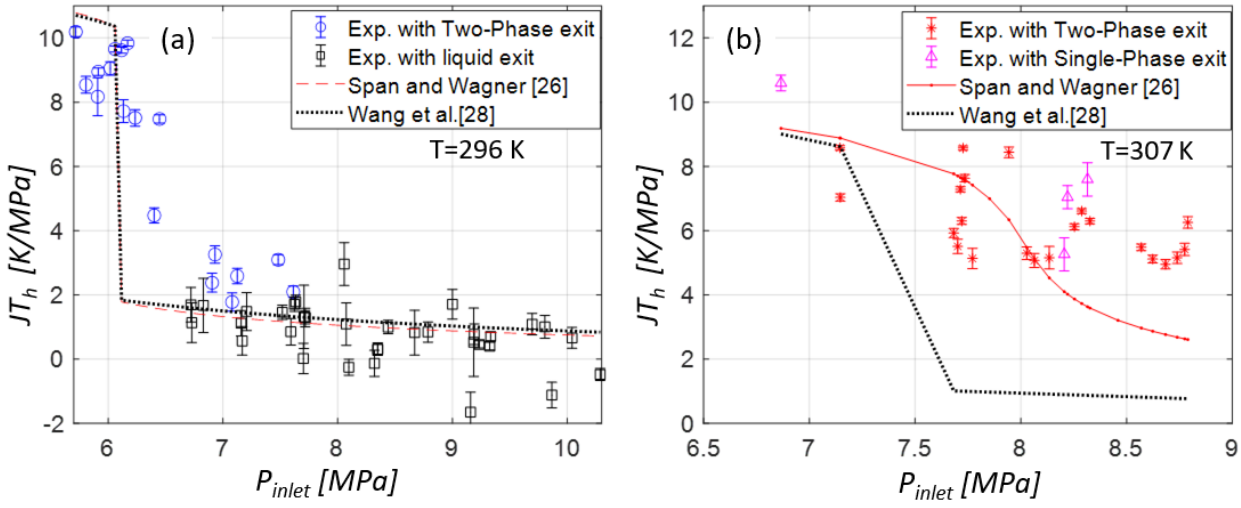

Figure 49- (a) Measured and calculated JTh coefficient for liquid and pressurized liquid at the inlet. The temperature for these experiments was sub-critical and was averaged for the calculation to be 296 K, (b) Measured and calculated JTh coefficient for supercritical and vapor at the inlet with an inlet temperature for calculation of 307 K [187].

For practical purposes, it is useful to map the strength of the Joule-Thomson effect to the phase of the fluid (i.e., vapor, liquid, or supercritical). Thus, the Span and Wagner equation [11] and NIST EFPROP software [161] were used to express the JT_h coefficient in a two-phase diagram, and to provide some measure of the relative strength of the coefficient in the vapor phase, or the vapor-like phase for supercritical fluid, and the liquid phase, or the liquid-like phase for supercritical fluid (Fig. 50). For subcritical conditions, the JT_h coefficient is an order of magnitude larger for vapor than for liquid, and this difference decreases with pressure. Past the critical condition, a large difference between the JT_h of the vapor-like and the liquid-like states still exists, but it gradually diminishes with pressure. When supercritical CO_2 transitions between these two states (i.e., from vapor-like to liquid-like or vice versa), the molecular structure of the fluid changes [170], [188], which results in large changes in its thermophysical properties, including the JT_h coefficient. It is interesting to note that during the transition from subcritical to supercritical, the ratio

between the JT_h of the vapor, or vapor-like, and the liquid, or the liquid-like, is continuous and its gradient is also continuous.

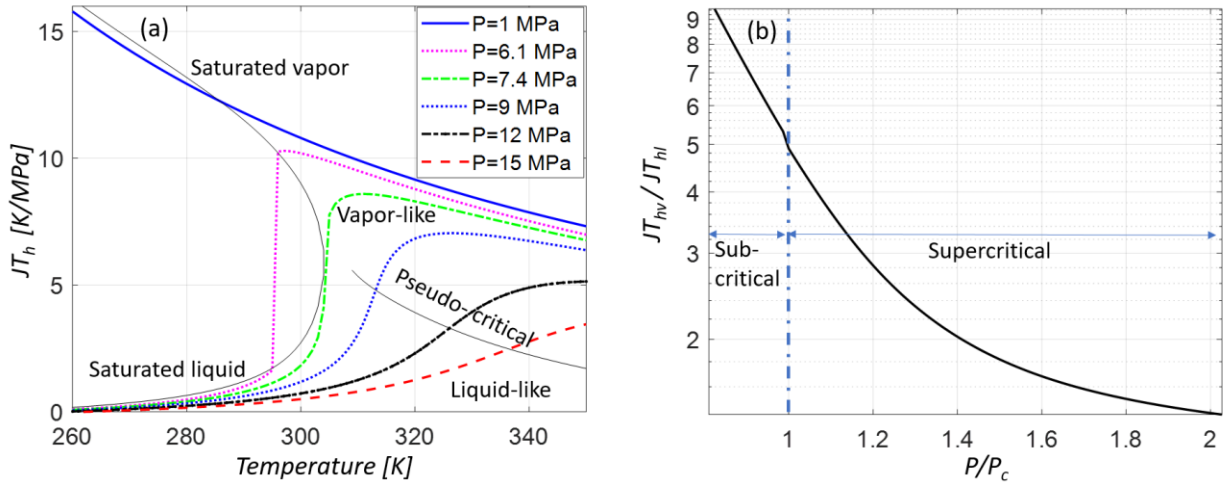

Figure 50- The Joule-Thomson coefficient characteristics. (a) JT_h as function of temperature at different pressures. The descending black line to the right of the two-phase region is the pseudocritical conditions calculated using the Span and Wagner equation [11] at the pseudo critical temperature. The region above the line is the vapor-like supercritical state and the region below is the liquid-like supercritical state. (b) The relative magnitude of the JT_h for the vapor phase (or vapor-like phase for supercritical fluid), JT_{hv}, and the liquid phase, or liquid like phase for supercritical flow, JT_{hl}. JT_{hl} was evaluated at 5 K subcooling temperature, and JT_{hv}, was evaluated at 5 K above the saturation temperature. Properties were calculated using the Span and Wagner [11] equation of state and NIST REFPROP software [161], [187].

6.5.3. Comparison to available correlations

Figure 51 compares the experimental results, which were divided into single-phase (shown as red circles) and two-phase mixture (shown as blue squares) at the orifice exit, to the models given in Table 7. The predictions of the single-phase pressure-drop with the homogeneous and separated flow models were identical since similar equations were used, while the single-phase flow calculated by the capillary tube model was comparable to the single-phase equations used in the homogeneous and separate models. The homogeneous flow, separated flow, and capillary tube models overpredicted the single-phase results

compared to the short-tube orifice model, which slightly underpredicted the pressure drop. For two-phase flow at the orifice exit, the models were more inconsistent. Predictions can be divided to low pressure drops of 1 MPa to 2 MPa, moderate pressure drops of 2 MPa to 4 MPa, and high pressure drops of 4 MPa to 6 MPa. The homogeneous flow model overpredicted experiments for the low and moderate ranges, while it predicted well the high range. The separated flow model mostly overpredicted the experimental results for all ranges. The capillary tube model predicted most of the results within a ±50% margin, although for the high range it mostly underpredicted the pressured drop. The short-tube orifice model underpredicted the high pressure drop range, while it predicted reasonably well experiments at the low and moderate ranges. The homogeneous flow, separated flow, capillary tube, and short-tube orifice models had a total MAE of 0.84 MPa, 1.41 MPa, 0.7 MPa, and 0.75 MPa, respectively.

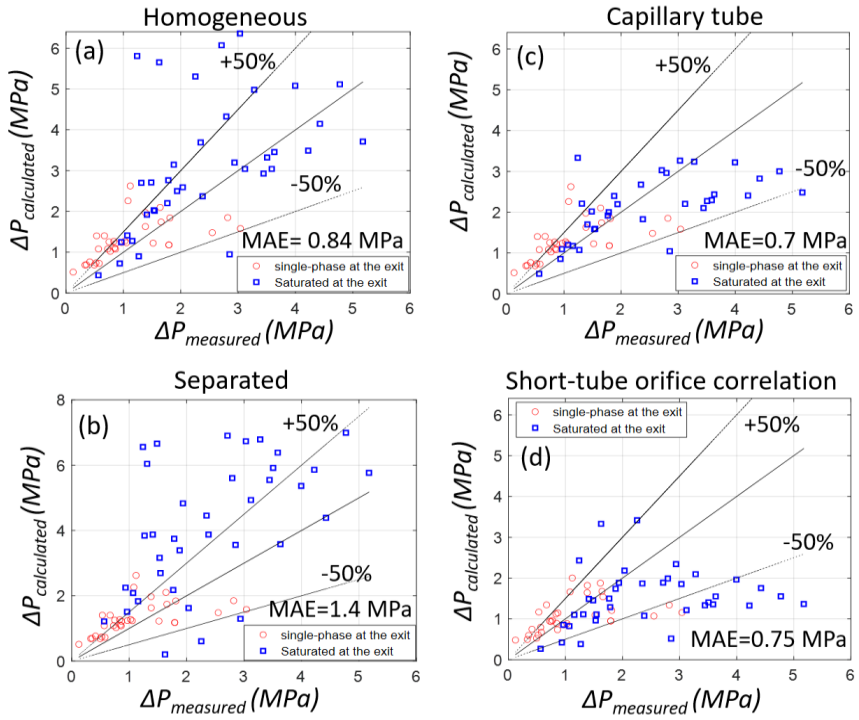

Figure 51- comparison of measured and calculated pressure drop of (a) the homogeneous flow, (b) the separate flow, (c) the capillary tube, and (d) the short-orifice tube correlations/models. MAE of 0.84 MPa, 1.4 MPa, 0.7 MPa, and 0.75 MPa were calculated, respectively [187].

With knowledge of the exit pressure and enthalpy, the exit mass quality can be determined through the equation of state [11] (i.e., $x_{exit}=x(P_{exit},h_{exit})$), and as shown in Fig. 52, most of the exit mass qualities ranged between 0 to 0.6. The mass quality tended to increase with decreasing exit pressure. The homogeneous flow model provided the best fit for the entire range, while the separated flow model overpredicted the experiments for mass qualities from 0 to 0.2, which was directly related to the overprediction of the pressure drop that led to lower exit pressures, and consequently, to higher mass qualities. For the high mass quality experiments of 0.9 to 1, the homogeneous flow and short-tube orifice predicted well the exit quality, while the capillary tube model predicted superheated vapor at the exit. The overall *MAE*s for the mass qualities were 0.07, 0.14, 0.09, and 0.09 for the homogeneous flow, separated flow, capillary tube, and short-tube orifice models, respectively.

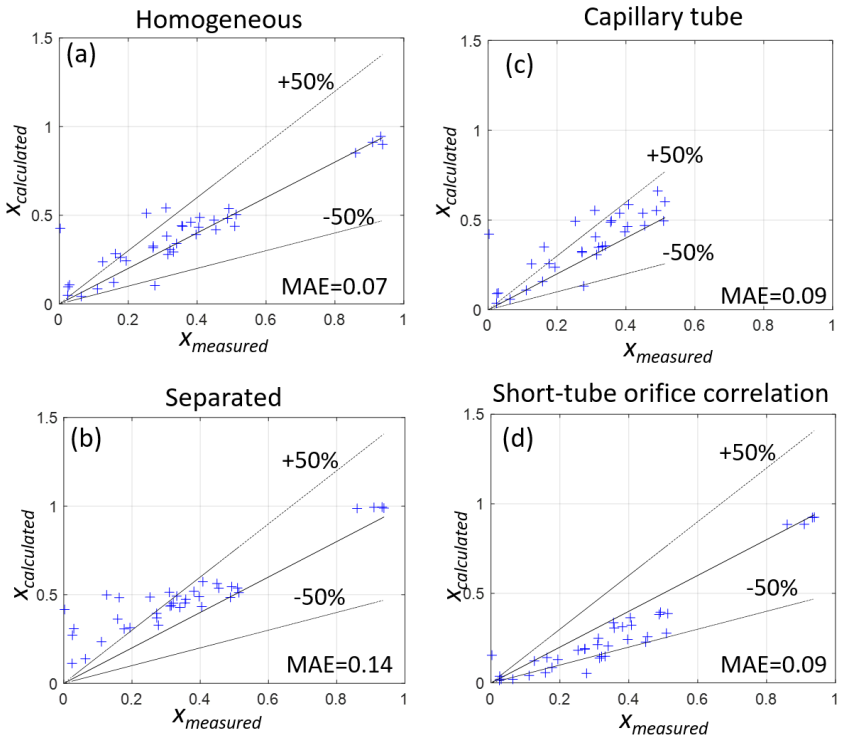

Figure 52- comparison of measured and calculated mass quality for the (a) homogeneous flow, (b) separate flow, (c) capillary tube, and (d) short-orifice tube correlations/models. MAEs were 0.07, 0.14, 0.09, and 0.09, respectively [187].

Figure 53 presents the corresponding temperatures obtained based on the pressure and enthalpy at the orifice exit. Higher pressure-drops led to lower exit pressures, which resulted in lower exit temperatures. The single-phase temperatures were predicted well based on the calculated pressure drop for single-phase flow, the capillary tube equations, and the short-tube orifice correlation. For a two-phase exit, the homogeneous flow model predicted the experimental exit temperature reasonably well, except for five data points that resulted in temperatures below 240 K, which were measured to be about 280 K. The separated flow model underpredicted the exit temperature, as it overpredicted the pressure drops. The capillary tube model overpredicted the lower temperature experiments of 260 K to 270 K, for which the calculated temperatures ranged from 280 K to 290 K. The short-tube orifice correlation overpredicted almost all experiments (except for 4 data points) between 260 K and 270 K, for which the model predicted an exit temperature of 290 K to 300 K ─ about 10 K more than the capillary tube model. The MAEs for the exit temperatures were 7 K, 13.3 K, 5 K, and 5.2 K for the homogeneous flow, separated flow, capillary tube, and short-tube orifice models, respectively.

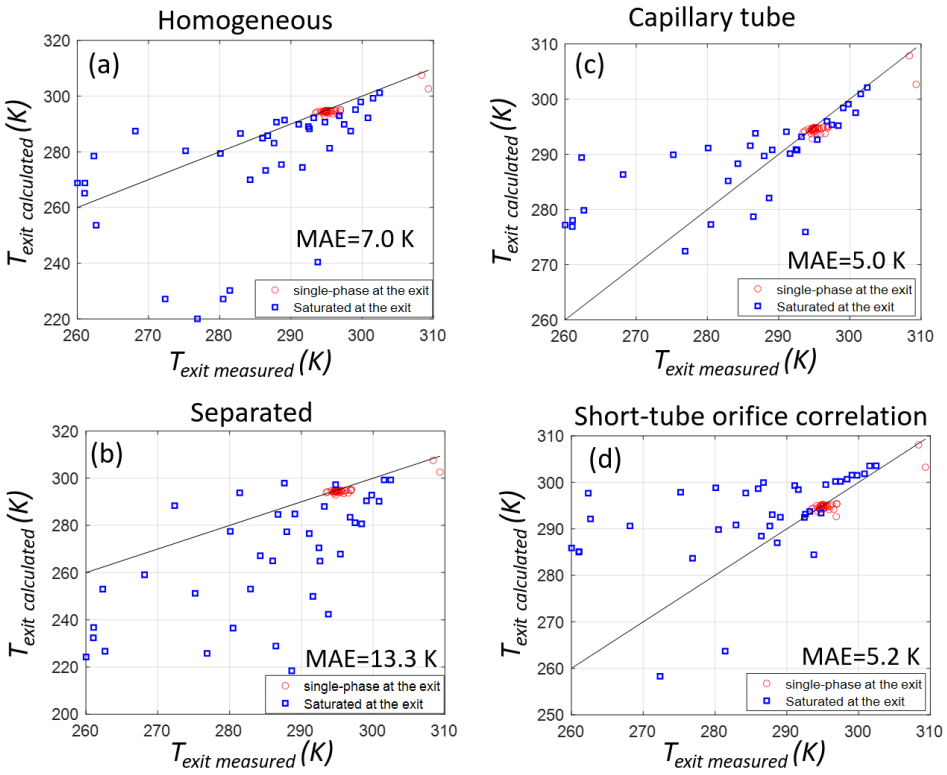

Figure 53-Comparison of measured and calculated temperatures by (a) homogeneous flow (b) separated flow, (c) capillary tube, and (d) short-orifice tube correlations. The MAE were 7 K, 13.3 K, 5 K, and 5.2 K, respectively [187].

7. SUMMARY AND CONCLUSIONS

7.1. Onset of boiling and subcooled flow boiling

In this work, new experimental capabilities revealed a significant heat transfer enhancement with flow boiling of CO_2 near the critical point at the microscale. Low superheated temperature and high heat transfer coefficients were reported. Several analytical models for onset of nucleate boiling, and heat transfer coefficient complemented current experiments and were used to infer the active cavity size. It was found that the superheat temperature at the onset of nucleate boiling is inversely proportional to the operating pressure, which can be attributed to the reduction of the active cavity size required for the onset of nucleate boiling. No dependency between the superheat temperature at the onset of nucleate boiling and mass flux was observed. The proposed corrections to Davis and Anderson's model did not better predict the current experimental data despite the added computational complexity. Experimental results of the onset of nucleate boiling were confined within the analytical models and the empirical correlation. Fixing the active nuclei bubble size derived from Hsu's model, applying it to the Young-Laplace equation, and calculating the saturation temperature for the effective pressure resulted in good agreement with the experiments.

Heat transfer coefficients of 51.2-204.5 kW/m^2K were experimentally obtained, and no dependency on the mass flux was established.

Portions of this chapter previously appeared in:

A. Parahovnik, M. Asadzadeh, S. S. Vasu, and Y. Peles, "Subcooled Flow Boiling of Carbon Dioxide Near the Critical Point Inside a Microchannel," *Phys. Rev. Appl.*, vol. 14, no. 5, p. 054050, Nov. 2020.

Anatoly Parahovnik, Yoav Peles, 2022, "High pressure saturated flow boiling of CO2 at the micro scale", *International Journal of Heat and Mass Transfer*, Vol. 186.

Anatoly Parahovnik, Yoav Peles, 2022, "Bubble dynamics in a subcooled flow boiling of near-critical carbon dioxide", *International Journal of Heat and Mass Transfer*, Vol. 183, Part C.

Anatoly Parahovnik, Yoav Peles, 2022, "Heat transfer mode shift to adiabatic thermalization in near-critical carbon dioxide with flow boiling in a microchannel", *International Journal of Heat and Mass Transfer*, Vol. TBD.

A. Parahovnik, P. Ahmed, Y. Peles, "Pressure drop and Joule-Thomson effect in a micro orifice with trans critical carbon dioxide flow", *Journal of supercritical fluids*, under review.

It was found that Shah's correlation under-predicted experiments for reduced pressures above 0.81. Kandlikar's correlation predicted experiments within a margin of ±30 % and an MAE of 15% with an adjusted coefficient. The Cheng's correlation indicated the experimental data the best, although the error increased as the reduced pressure approached unity.

The discrepancies between the correlations and the experimental results are linked to the high reduced pressure used to obtain the experimental data (from 0.82 to 0.95 compared to less than 0.76, less than 0.8, and less than 0.87 for Shah's, Kandlikar's, and Cheng's correlations, respectively). Furthermore, the Shah's and Kandlikar's correlations were developed using a large number of fluids, and thus, can be more generally applied, but with a somewhat compromised accuracy.

7.2. Saturated flow boiling, film flow boiling and critical heat flux

Saturated flow boiling of carbon dioxide at high pressure in a microchannel was experimentally studied. Saturation conditions were locally generated and maintained within the micro-device. Mass qualities ranging from 0 to 0.94 were examined for heat fluxes of up to 270 W/cm^2. Boiling curves were presented, HTCs were inferred, and CHF conditions were obtained. The ratio of the two-phase heat transfer coefficient to a liquid-portion heat transfer coefficient, Ψ, was evaluated and was found to increase significantly with mass quality. The observed data were explained using flow pattern map proposed by Cheng at al. [1], [40], [43]. The HTCs were compared to three correlations and were found to be best predicted by the Shah correlation [148], which was compared with a saturated carbon dioxide flow in the discussed paper. It was also found that the correlations failed to predict the HTC trend for dry-out, and they significantly underpredicted the HTC for mist flow. It was also found that the flow patterns produced by Cheng et al. [1], [40], [43] can be generally used to explain the physical phenomena of the experiments. Post-CHF heat transfer coefficient was compared with three models that were fitted within 33% accuracy band using a single coefficient. Kutateladze [154] correlation with a data derived coefficient and the Katto et al. [151] correlation predicted the CHF conditions reasonably well. of the agreement between the experiments and Katto et al.[151] correlation confirms the negligibility of gravity effects for pressurized CO2 in

microchannels, and the agreement with the Kutateladze [154] equation suggested that departure from nucleate boiling and dry-out for pressurized CO2 were unaffected by the mass flux.

7.3. Bubble dynamics

Bubble characteristics during subcooled flow boiling of CO_2 near-critical condition was experimentally studied. Bubble diameter, velocity, and bubble-to-bubble interactions were discussed and quantified. The smallest detectable bubble departure diameter was 2 μm, and the bubble generation rate was strongly influenced by the heat flux. It was also found that the average bubble size and the bubble growth were reduced as the pressure approached the critical value. High speed visualization revealed the formation of a distinct boiling inception line perpendicular to the flow for fully developed flow boiling. It was also found that the thermally driven Reyligh-Plesset asymptotic solution and the Poiseuille flow profile with constant relative velocity were adequate to describe the bubbles' dynamics for isolated bubble, while the inertially driven model failed to predict the bubble dynamics. However, when bubbles began interacting with one another, deviation between experiments and the model were noted. An additional term for the thermally driven Reyligh-Plesset solution was proposed, calibrated, and verified. The coefficient 'a' was found to be a function of specific heats ratio and the boiling number. The coefficient completely diminishes when the critical pressure was reached. Finally, it was found that the adjusted model reduced the MDE from 13.5 μm to 6.6 μm — a relative decrease of 51% — and correlated well with the experimental data.

7.4. Adiabatic Thermalization – The piston effect

The piston effect in the vicinity of the critical condition was experimentally studied and quantified for flow boiling heat transfer under terrestrial gravity. Initially, remote local temperature measurements without flow markers were obtained employing the opalescence effect near the critical condition. Subsequently, the data was compared with theoretically calculated temperature increase of fluid's bulk due to the piston effect. The results showed that a reduction in void fraction coincided with an enhanced heat transfer coefficient.

The nature of the shift between low-pressure thermalization (i.e., boiling), associated with a first-order phase change process (i.e., discontinuity of the thermodynamic properties like density and internal energy) and the near-critical pressure thermalization process (i.e., the piston effect), dominated by a second-order phase change (i.e., discontinuity of the thermodynamic properties' derivatives like specific heat at constant pressure and isothermal compressibility) was revealed. For the first time, this work demonstrated the shift from boiling-dominated heat transfer to adiabatic thermalization (i.e., acoustic thermalization) for convective flow boiling under terrestrial gravity, which led to a significant heat transfer enhancement despite the reduction in the void fraction. Since gravity effects are negligible in micro-fluidics in general and specifically under the current conditions [64], the piston effect stand out as a significant heat transfer mechanism. The dominance of the piston effect in forced flow at the micro scale is partially attributed to the laminar regime typical of flow in microsystem in which mixing is suppressed and to the declining effect of gravity with length scale. These conditions have not yet been visualized for near-critical fluids. The adiabatic thermalization mode at the micro scale under terrestrial conditions can be used to manage high-frequency thermal loads, like radar, laser systems and a range of high-frequency applications. The nature of heat transfer pertinent to the piston effect in forced convection flows is poorly understood, but if properly revealed, it holds great potential to revolutionize copious critical technologies that depend on effective thermal transport.

7.5. Pressure drop and Joule-Thompson effect

Pressure drop and the Joule-Tomson effect were experimentally obtained and compared to available models and correlations. Four different models were examined including the homogeneous flow, separated flow, capillary tube, and short-tube orifice models. For the first three, the orifice was divided into 100 subsections to account for changes in the fluid's phase and its thermophysical properties; the short-tube orifice model used the temperature and pressure at the inlet to evaluate the pressure at the exit. Mass qualities and exit temperatures were calculated using NIST REFPROP [161]. The capillary tube model best predicted the

pressure drop and temperatures, while the homogeneous flow model best predicted the mass quality. The homogeneous flow and the capillary tube models are most appropriate for pressure drop prediction.

The Joule-Thomson coefficient was measured for four different inlet phases including liquid, pressurized liquid, vapor, and supercritical flows and resulted in two different exit phases (i.e., single-phase or two-phase). For supercritical and vapor inlets and high mass quality two-phase mixture or supercritical/vapor exits, the JT_h coefficient was significantly higher compared to liquid and pressurized liquid inlet that resulted in low mass qualities of up to 0.1 or a single-phase liquid exit. The Span and Wagner model [162] adequately predicted the experimental results.

For inlet flow at a high temperature (within the examined range) the JT_h coefficient was higher than for liquid inlet conditions (about 7 K/MPa compared to about 1.5 K/MPa). However, even with liquid inlet conditions, a JT_h of about 8 K/MPa was achieved when the exit state reached sufficiently high mass qualities. The JT_h dropped considerably when the supercritical CO_2 transition from 'liquid like' to 'vapor like Flow.' The increase in the JT_h coefficient can be practically implemented since it indicates that if a hotter CO_2 (i.e., 'vapor-like') undergoes isenthalpic expansion, at certain conditions it can result in a considerably lower temperature at the exit of the orifice.

APPENDIX A – BOTTOM PIECE MICROFABRICATION RECIPE

step	Process (Presentation)		Tool & Recipe
Wafer Preparation		(Fused Silica ordered from Mark Optics- Herause Quartz glass optics Supersil 313 brand.)	100 mm × 0.5 mm , DSP
Piranha clean			Using Hamatech Piranha wafer cleaning process
Sputter Ti/Pt/Al 1 (7 nm, 60 nm, 1µm)	2		Using AJA Sputtering tool (detailed description following the table) a. Duaration: 57sec/114sec/5000sec
Al wet etching 1	3	Mask #1	
Photolithography	3		a. HMDS adhesion promoter liquid—P20 b. Spin photoresist S1818 4000rpm 3000 acceleration 45seconds c. Soft bake hotplate 90secs @115°C d. Exposure 4.5secs MA6 contact aligner recipe"Photolithography, 30um, 4.5sec, soft contact, offset off" e. post bake 90secs @115°C f.Develop Hamatech recipe "726MIF 90secs DP" h. hard bake, 90secs @115°C usually sued for more fine features (Skipped this step) g. inspect under the microscope
Al etching	3	Wet etchant	Al etchant 22-30 min @R.T
Strip PR	3		Using 1165 striper 15 min with ultrasound and heating, Cleaning is done with Acetone and then methanol
Pt and Ti etching 1	4	Mask #2	Main tool: AJA Ion mill
Photolithography	4		The same as 3.
Pt, Ti etching	4		**It is AJA ion mill, the tool have the same user interface as the sputtering tool.**(more details in the end)
Strip PR	4		Strip is done using Anatech resist strip (High temperature process) 25min using O2 stripper
Sio2 Deposition 1	5	Oxford PECVD	Thickness: 1.1 µm the idea is to cover entirely the heater layer

step	Process (Presentation)		Tool & Recipe
Sputter Ti/Pt/Al 2 (7 nm, 60 nm, 1µm)	6		b. Duaration: 57sec/114sec/5000sec
Al wet etching 2	7	Mask #3	
Photolithography	7		Same process
Al etching	7	Wet etchant	
Strip PR	7		
Pt and Ti etching 2	8	Mask #4	
Photolithography	8		Same process
Pt, Ti etching	8		
Strip PR	8		
Si oxide deposition 2	9	Oxford PECVD	Thickness: 3 um (10:18 min) (have to close all topological differences for CMP)
CMP	10	CMP Tool	Polishing the surface 2 min+6 min process it removed 1.6 um of oxide- the process is not stabilized yet.
Pads Etching	11	Mask #5	
Photolithography	11		Same process
Dry Etching 1	11	Oxford 81 Dry etch	Oxide $CHF_3\backslash O_2$ Process Etching rate for PECVD oxide is 34.4 nm/min
Strip PR	11		
Only heater pads Etching	12		
Photolithography	12		Same process
Dry Etching 2	12	Oxford 82 Dry etch	Oxide $CHF_3\backslash O_2$ Process Etching rate for PECVD oxide is 34.4 nm/min
Strip PR	12		
Dicing	13		Apply PR to protect the surface. Use white tape

1. **AJA Sputtering tool**: **(Tom)** tool guide is extremely good the main idea is just to follow the instruction page by page.
   - The wafer is mounted on a special plate that is located near the tool

- The mounted plate is manually loaded into the sputtering chamber (use the user's manual book)
- The needed steps are defined according the process specification guide (another book attached to the tool)
- There is 3 main parameters for each process are: a. deposited material, it is attached to specific Gun#. b. chamber pressure (3,7 or 20 mTorr) c. Rotation of the mounted plate during the process.
- The steps were chosen according to the most convenient residual stresses in the deposited layer.

The steps are:
First step is surface cleaning using RF source, the definition of the process is located in the users manual.
Second step Ti: duration:**67 sec**, Pressure: **7 mTorr** and rotation: **On,** Target thickness**:10 nm**
Third step Pt: duration:**114 sec**, Pressure: **20 mTorr** and rotation: **On, ***Target thickness**: 60 nm**

Forth Step Al: duration: **4975 (~5000) sec**, Pressure: **3 mTorr** and rotation: **On, Target Thickness:1000 nm**

* Pt target layer was 30nm which according to calculations corresponds to 407 Ω according to the process guideline book it corresponds to 57 Sec, however after fabrication the measured resistance was 2kΩ which is quite far from the design point and therefore the deposition time was doubled, afterwards the resistance dropped approximately by factor of 2 which leads to 0.8 kΩ of RTD resistance.
- The different steps was defined as 'layers' which later on combined to a process
- run the process
-dismount the wafer.

2. **Photolithography Insights: (Gerry)**
   - There is a need to apply the Vacuum suction while baking the PR.
   - After the spinning there is a thick layer accumulation at the edges of the wafer it can be solved by specific station that help cleaning the edges while spinning
   - If the layer wasn't applied well it can be removed and re-spinned using acetone and isopropanol, this two liquids purred onto the wafer while it spins at first both together and followed only by isopropanol (must be the last liquid purred on the wafer and then spin dry) – Ask Gerry.
   - It is important to check after the development whether the features is intact and looks good, especially the small one (RTDs)

3. **Aluminum Etching: (Chris.)**
   - The etching process can take 22-30 min.
   - The Al has kind of milky color and during the etching there is formation of bubbles inside the vessel.
   - When the etching is done the Pt beneath it has different color, more 'metal' like and the bubbling ends.
   - The process is relatively invariant to time which means that +/- 3 minutes will not damage the device.

4. **AJA Ion Mill: (Jerry D.)**
   - There is a copper lattice that have to be mounted under the plate- make sure it is present.
   - Etching rates (as defined in the adjoined text):
     - Ti - 20-55 nm/min
     - Pt – 75-80 nm/min
   - Working Voltage 400V , Working current 0.4 mA/cm^2
   - Measuring voltage 500V, measuring current 1 mA/cm^2
   - Good estimation for duration adjustment is X5 which means for Pt layer of 30nm and Ti layer of 10nm the needed time for etching is 0.733 min X5X60 ~ 220 sec of actual milling (the setup is 230 sec)
   - In order to reduce wafer heating duty cycle of 0.5 was implemented.
   - The time were split to 10 cycles (='layers') of 23 sec of milling and 23 sec of delay.
   - The layer were defined, first layer is different (ask. Jerry)
   - Other process layers were added as defined in the tool guide.
   - After 8-9 layers the uncovered Pt and Ti was 'gone', the rest of the layers didn't damaged the devices.
   - In later on devices the Pt thickness were doubled the milling layers were adjusted to 14, the process called 'parahovnik thick' the process was successful.

5. **Photo Resist Stripping:**
   - A general note stated (from Jeremy) said that after dry process as Ion Mill you use a dry PR strip process like Anatech resist strip and after wet etching like Al etching you use wet strip like 1165.
   - From my experience 1165 was fine in removing the remints of PR that was left after Plasma etching although in some case 15 min wasn't enough, visual inspection for PR removal in my opinion is adequate.
6. **Oxford PECVD: (Jeremy)**
   - Do a seasoning process of 1-2 min, which means to run the relevant deposition process before loading the sample.
   - Pre heating should be adjusted to 4 min for silica wafer.
   - Duration for 1.1 um is 3:48, the user interface is working with min:sec definition.
   - After 4 um of deposition there is a need to stop the process and clean the chamber HIGH RATE CLEAN.
   - For the top layer a 3 um deposition were done duration 10:18.
   - After finishing working a HIGH RATE CLEAN clean process have to be performed the duration is (Total deposition time inc. seasoning)+ 10 min.
7. **CMP: (Chris)**
   - First wafer were polished for 2 min and then 6 min more after inspection it removed 1.6 um of oxide it didn't flatten completely the surface we have some pattern of 0.15-0.2 um as measured using profilometer (p-7 profilometer were used to to define the surface texture and structure)
   - Second wafer was set to 7:30 min, the wafer was grounded after about 5 min and damaged the shims of the machine.
   - There were no replacement for the shims and therefore other wafers weren't polished.
   - Next time work with Chris again to develop a robust process and ask him for training AGAIN.
8. **Oxford 81 oxide etching: (Jerremy)**
   - The chamber should be re-processed for 1-2 min (As PECVD) before inserting a sample.

- The process is $CHF_3\backslash O_2$ Oxide removal the rate is 34.4 nm/min – different than what is stated in the guide book.
- The PR etching rate is about 1:1.
- It is rather hard to remove the oxide after the process, the most convenient way is by using 1165 with ultrasonic and heating.
- 30 min Max. Etching time were used afterwards the mask were regenerated (washed and applied again) this number can be re-evaluate for different applications.
- In this process the mask were changed from number 5 to 6 and backward in order to reach the desired depth.

9. **Dicing: (Sam)**
   - Dicing process were defined through (Sam. → Advanced) predefined program
   - Parameters are: two way run 0.35 mm high and 0.035 mm high
   - Spacing channel 1: 28mm, Spacing channel 2: 21 mm for automatic cut this spacing is solid to get same size devices
   - Foot print of the blade were adjusted according to the spacing between the devices (0.7mm).
   - Develop the process of dicing on a dummy wafer with sam, the wafer should have the needed pattern, for example by applying and developing a PR with relevant pattern.
10. **Profilomenter P-7: (Jerremy)**
    - Very useful tool for measuring etching depth and topology of the devivce.

APPENDIX B – DERIVATION OF THE RETURNED LIGHT INTENSITY RATIOS AND FLUID TEMPERATURE RELATION

Scattering ratio (R) is defined as the ratio between the scattered light intensity to the induced light intensity:

$$R = \frac{I_i - I}{I_i} \quad (1)$$

The scattered light intensity is the difference between the induced light intensity (I_i) to the returning light intensity (I). The induced light originated in the light source (i.e., MicroLED illuminator) and, therefore, was always constant. In contrast, the returned light was influenced by the critical opalescence scattering, which is temperature dependent (i.e., Eq. 24 in the manuscript).

It is assumed that the scattered light intensity is considerably smaller than the induced light[181], which leads to R1 and R2 << 1, and since the temperature increase was up to several Kelvins, R2=R1+ΔR, where ΔR<<R1 and R2.

The ratio between the scattering light intensity ratios at location 1 and 2 can be expressed according to:

$$\frac{I_{r_2}}{I_{r_1}} = \frac{1 - R_2}{1 - R_1}$$

Then:

$$\frac{I_{r_2}}{I_{r_1}} = \frac{(1 - R_2) \cdot R_2/R_2}{(1 - R_1) \cdot R_1/R_1} = \frac{R_2 - R_2^2}{R_1 - R_1^2} \cdot \frac{R_1}{R_2}$$

Integrating $R_2=R_1+\Delta R$, yields:

$$\frac{I_{r_2}}{I_{r_1}} = \frac{R_2 - R_2^2}{R_1 - R_1^2} \cdot \frac{R_1}{R_2} = \frac{(R_1 + \Delta R - R_1^2 - 2 \cdot \Delta R \cdot R_1 - \Delta R^2)}{R_1 - R_1^2} \cdot \frac{R_1}{R_2}$$

$$\frac{I_{r_2}}{I_{r_1}} = [\frac{(R_1 - R_1^2)}{R_1 - R_1^2} + \frac{\Delta R - 2 \cdot \Delta R \cdot R_1 - \Delta R^2}{R_1 - R_1^2}] \cdot \frac{R_1}{R_2}$$

$$\frac{I_{r_2}}{I_{r_1}} = \left[1 + \frac{\Delta R}{R_1} \cdot \frac{(1 - 2 \cdot R_1 - \Delta R)}{1 - R_1}\right] \cdot \frac{R_1}{R_2} = \left[1 + \frac{\Delta R}{R_1} \cdot \frac{(1 - R_1)}{1 - R_1} - \frac{\Delta R}{R_1} \cdot \frac{(R_1 + \Delta R)}{1 - R_1}\right] \cdot \frac{R_1}{R_2}$$

$$\frac{I_{r_2}}{I_{r_1}} = \left[1 + \frac{\Delta R}{R_1} - \frac{\Delta R}{R_1} \cdot \frac{(R_1 + \Delta R)}{1 - R_1}\right] \cdot \frac{R_1}{R_2}$$

Since $\frac{\Delta R}{R_1} \rightarrow 0$, and $\frac{(R_1+\Delta R)}{1-R_1} \rightarrow R_1$

$$\frac{I_{r_2}}{I_{r_1}} = [1 - \Delta R] \cdot \frac{R_1}{R_2} = \frac{R_1}{R_2}$$

where Condition '2' corresponds to the fluid at the inlet temperature (i.e., T0) and Condition '1' corresponds to the measured temperature (i.e., T). The derived relation leads to Eq. 24 in the manuscript:

$$\frac{I_{To}}{I_T} = \frac{R_T}{R_{To}} = \frac{\frac{k_B \cdot \pi^2}{2 \cdot \lambda_o^4} \cdot T \cdot \beta_T \cdot \left(\rho \cdot \frac{\partial \varepsilon}{\partial \rho}\right)_T^2}{\frac{k_B \cdot \pi^2}{2 \cdot \lambda_o^4} \cdot To \cdot \beta_{To} \cdot \left(\rho \cdot \frac{\partial \varepsilon}{\partial \rho}\right)_{To}^2} = \frac{T \cdot \beta_T \cdot \left(\rho \cdot \frac{\partial \varepsilon}{\partial \rho}\right)_T^2}{To \cdot \beta_{To} \cdot \left(\rho \cdot \frac{\partial \varepsilon}{\partial \rho}\right)_{To}^2} \quad (2)$$

APPENDIX C – MEASUREMENTS OF THE RETURNED LIGHT INTANSITY RATIO

Bitmap files used to calculate returning light intensity were produced from data recorded by the camera. The returned light intensities were averaged perpendicular to the flow (along the marked lines on the images) and created the returning light intensity data presented in supplementary Fig. 2. The background elements influenced the returning light intensity measurements, and therefore, the readings were done on top of the heater where the background was uniform, see Graph in supplementary Fig. 2. The returning light intensity, corresponding to the ambient temperature (i.e., T0), was measured close to the heater's edge, upstream of the boiling inception line, see the blue lines close to the heater's edge in supplementary Fig. 2. The temperature downstream was measured before the RTD's vias; see the blue markings near the resistive temperature detector's via in supplementary Fig. 2. The downstream temperature reading was manually obtained from the figures. Additionally, it was verified that without the heater power, the returning light intensity did not change. No significant difference between the sampled returning light intensity for different images of the same experiment were found, further affirming the invariance of the temperature readings and presence of bubbles.

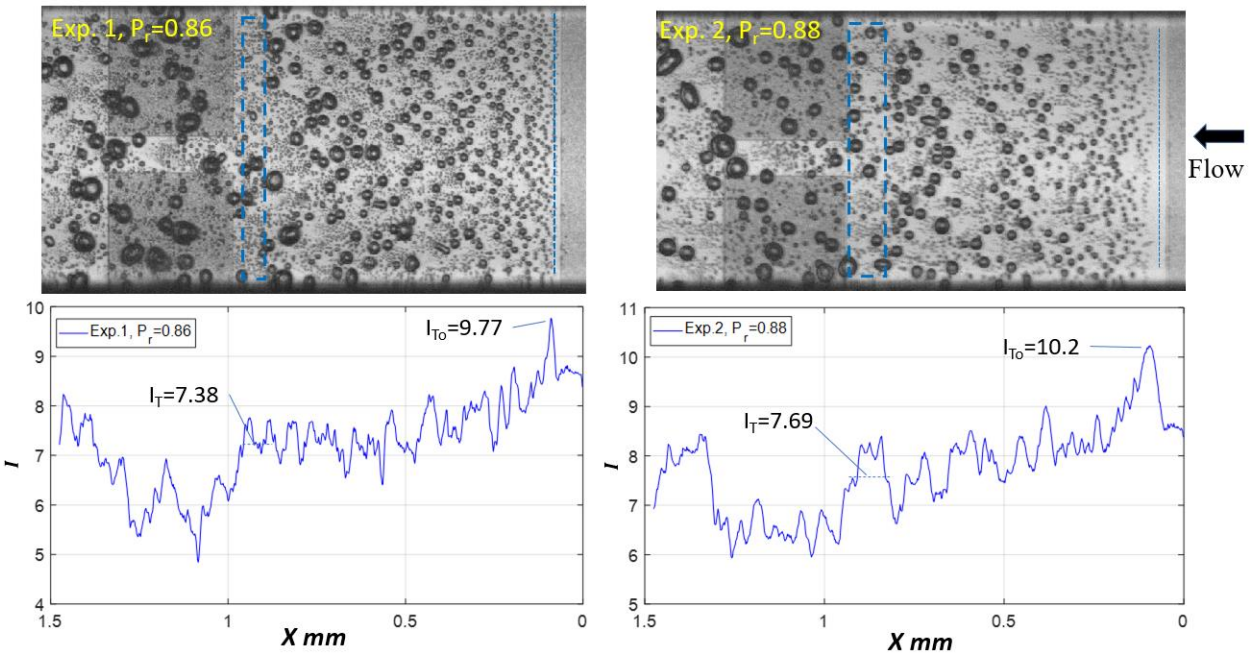

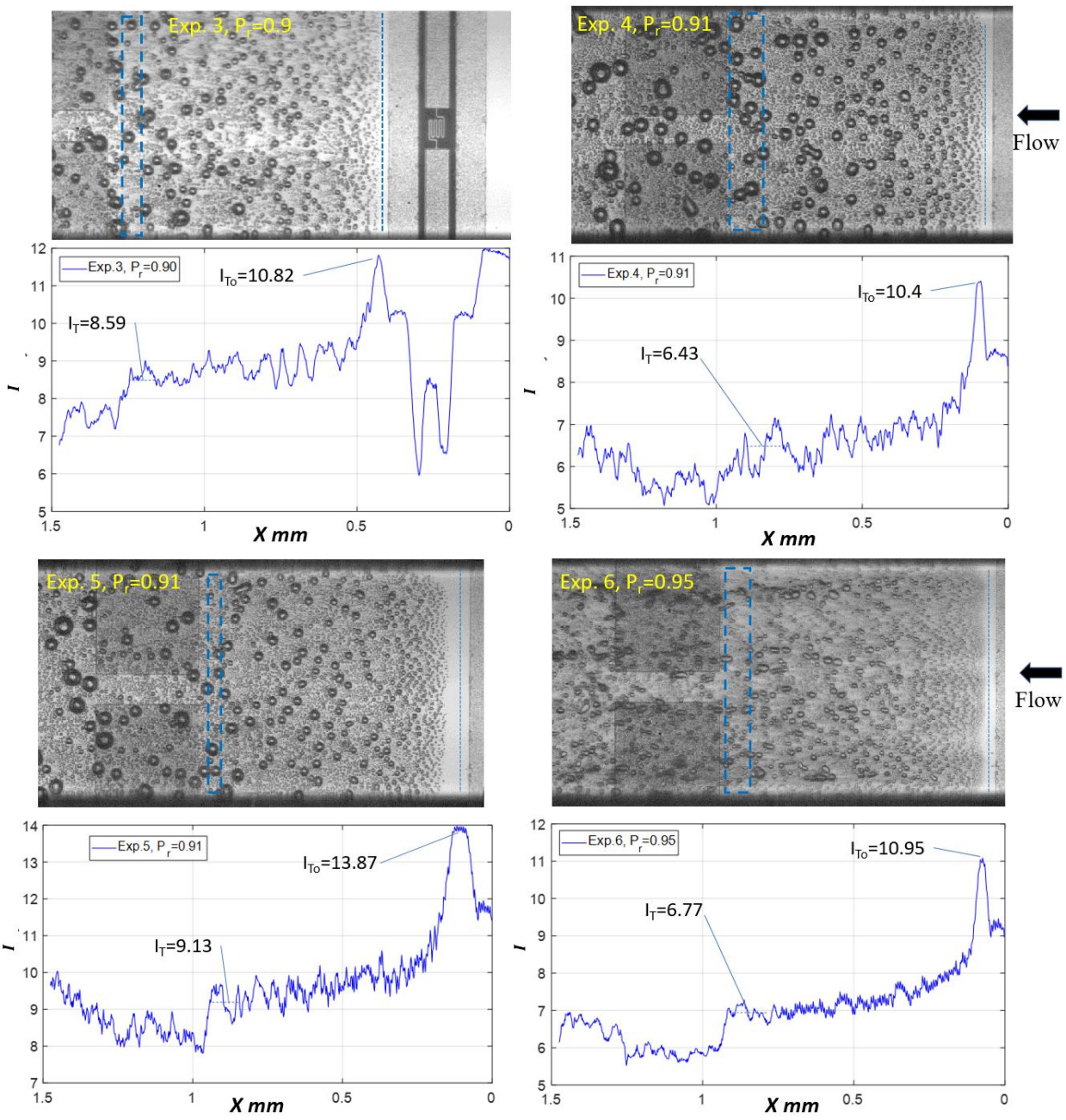
Exp. 3, Pr=0.9
Exp. 4, Pr=0.91
Flow
Exp.3, Pr=0.90
ITo=10.82
IT=8.59
Exp.4, Pr=0.91
ITo=10.4
IT=6.43
X mm
Exp. 5, Pr=0.91
Exp. 6, Pr=0.95
Flow
Exp.5, Pr=0.91
ITo=13.87
IT=9.13
Exp.6, Pr=0.95
ITo=10.95
IT=6.77
X mm

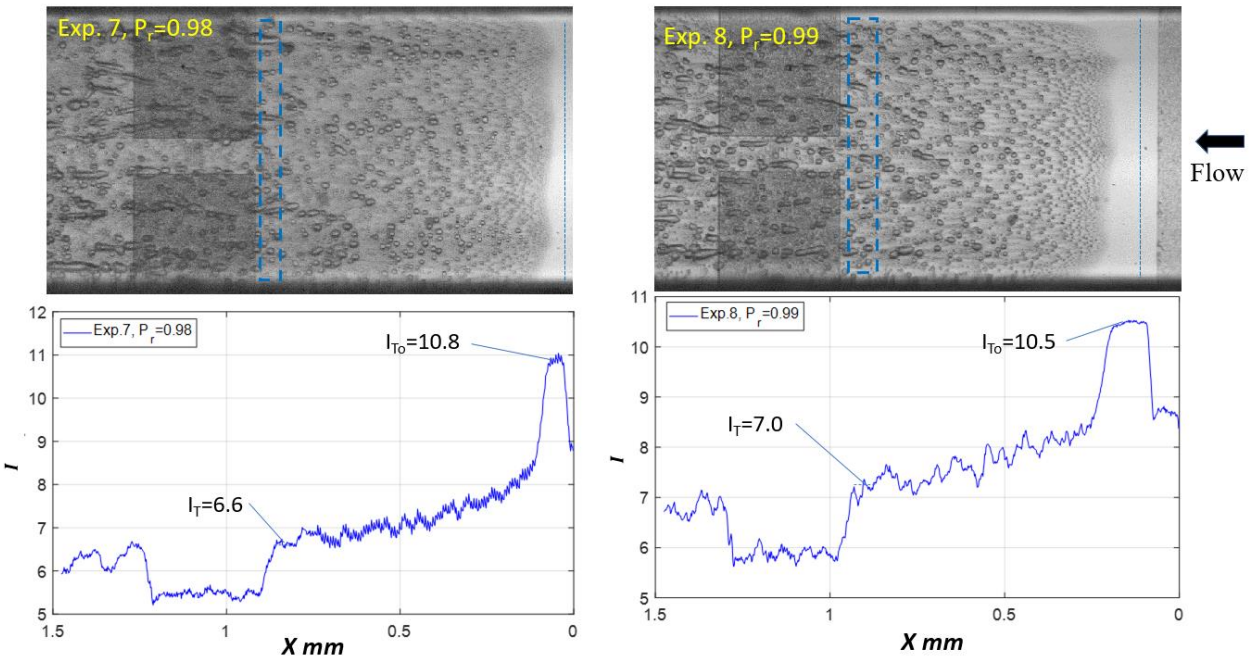

Supplementary Figure 2. Returned light intensity measurement

APPENDIX D – BULK FLUID'S TEMPERATURE CALCULATED FROM THE SCATTERING INTENSITY CHANGE

Supplementary Fig. 3 presents the ratios of the light scattering ratio (i.e., R_T/R_{T_0}) as a function of temperature difference (i.e., $\Delta T_R = T - T_0$) for all experiments. By comparing the returned light intensity ratio (i.e., It/IT) with the ratio of light scattering ratio (i.e., RT/RTo), the temperature difference (i.e., ΔT_R), consistent with the returned light intensity ratio, was inferred. This temperature difference corresponded to the increase in the fluid temperature as measured through the critical opalescence effect.

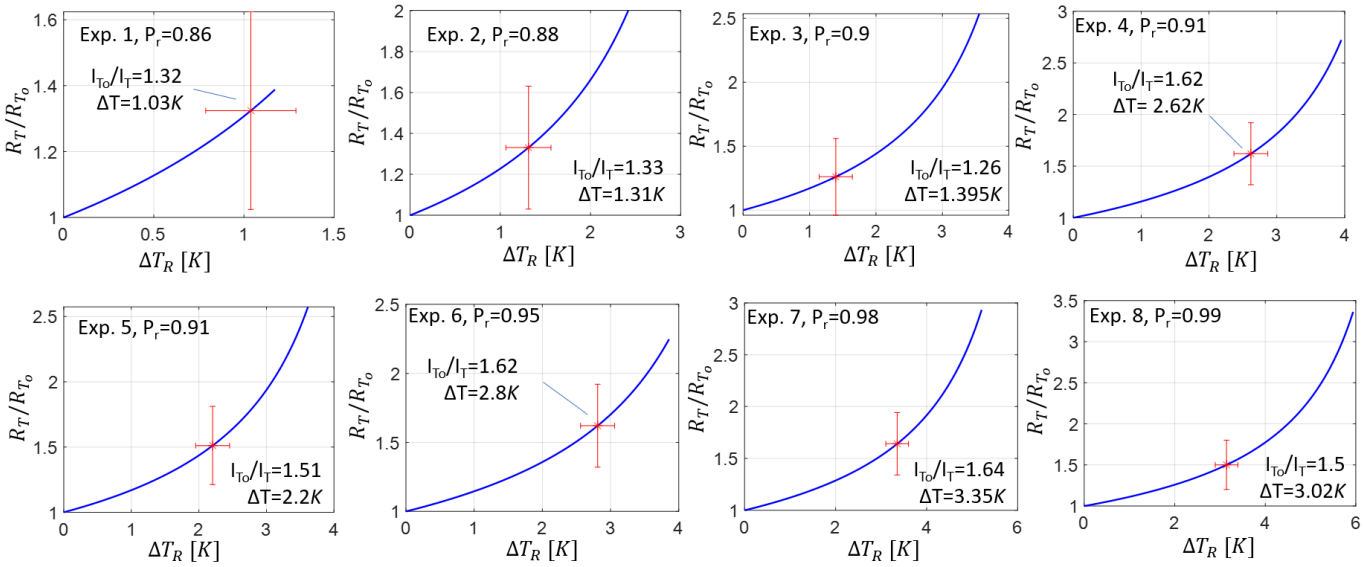

Supplementary Figure 3- The returning light intensity drops and the corresponding temperature difference of the fluid

APPENDIX E – TOP PIECE FABRICATION DRAWING

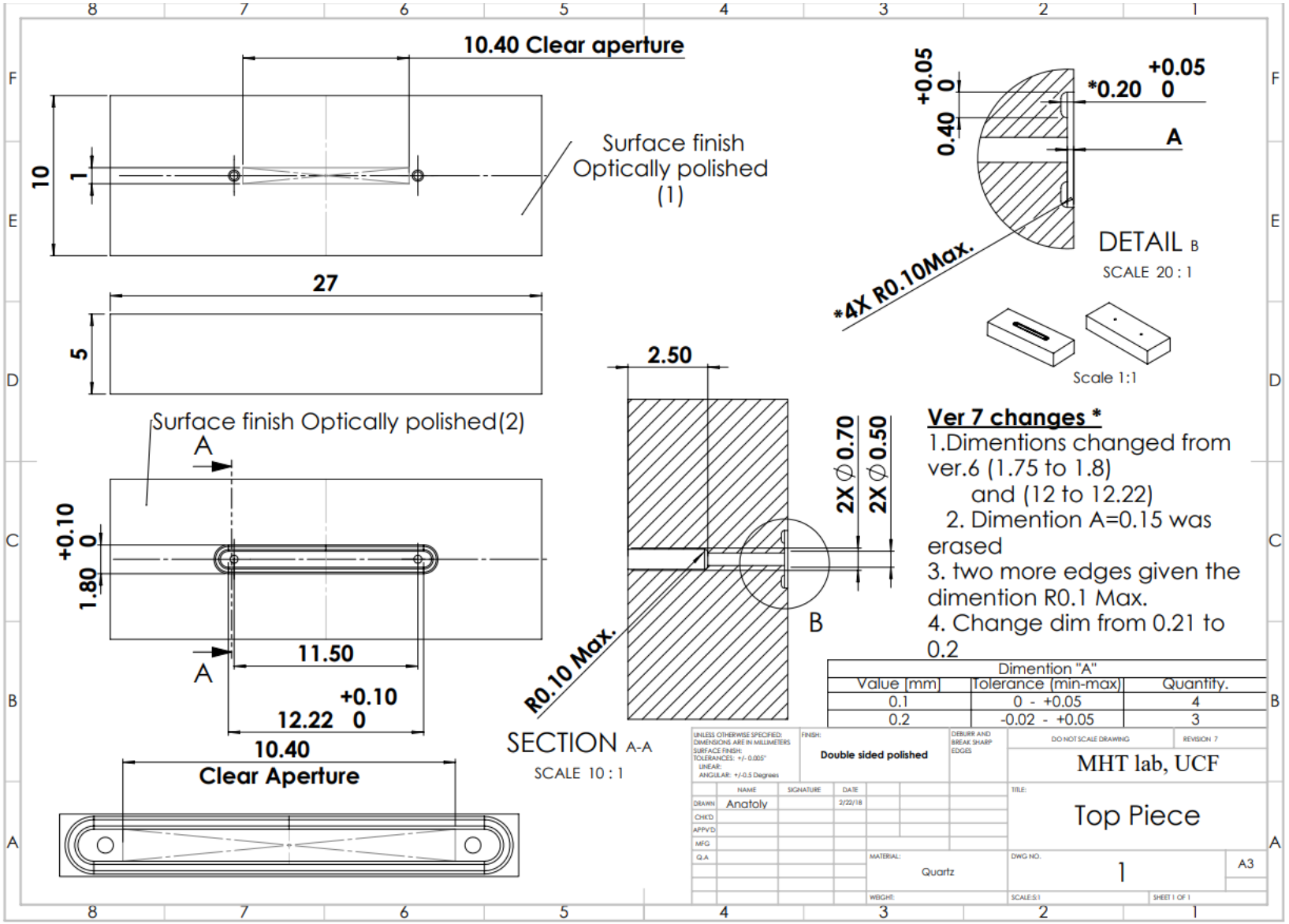
10.40 Clear aperture
10
1
Surface finish
Optically polished
(1)
27
5
Surface finish Optically polished(2)
A
+0.10
0
1.80
11.50
+0.10
12.22 0
10.40
Clear Aperture
+0.05
0
0.40
+0.05
*0.20 0
A
DETAIL B
SCALE 20 : 1
*4X R0.10Max.
Scale 1:1
2.50
2X ⌀0.70
2X ⌀0.50
B
R0.10 Max.
SECTION A-A
SCALE 10 : 1
Ver 7 changes *
1.Dimentions changed from ver.6 (1.75 to 1.8)
and (12 to 12.22)
2. Dimention A=0.15 was erased
3. two more edges given the dimention R0.1 Max.
4. Change dim from 0.21 to 0.2
Dimention "A"
Value [mm] | Tolerance (min-max) | Quantity.
0.1 | 0 - +0.05 | 4
0.2 | -0.02 - +0.05 | 3
UNLESS OTHERWISE SPECIFIED: DIMENSIONS ARE IN MILLIMETERS SURFACE FINISH: TOLERANCES: +/- 0.005" LINEAR: ANGULAR: +/-0.5 Degrees
FINISH: Double sided polished
DEBURR AND BREAK SHARP EDGES
DO NOT SCALE DRAWING
REVISION 7
MHT lab, UCF
NAME SIGNATURE DATE
DRAWN Anatoly 2/22/18
CHK'D
APPV'D
MFG
Q.A
TITLE: Top Piece
MATERIAL: Quartz
DWG NO. 1
A3
WEIGHT:
SCALE:5:1
SHEET 1 OF 1

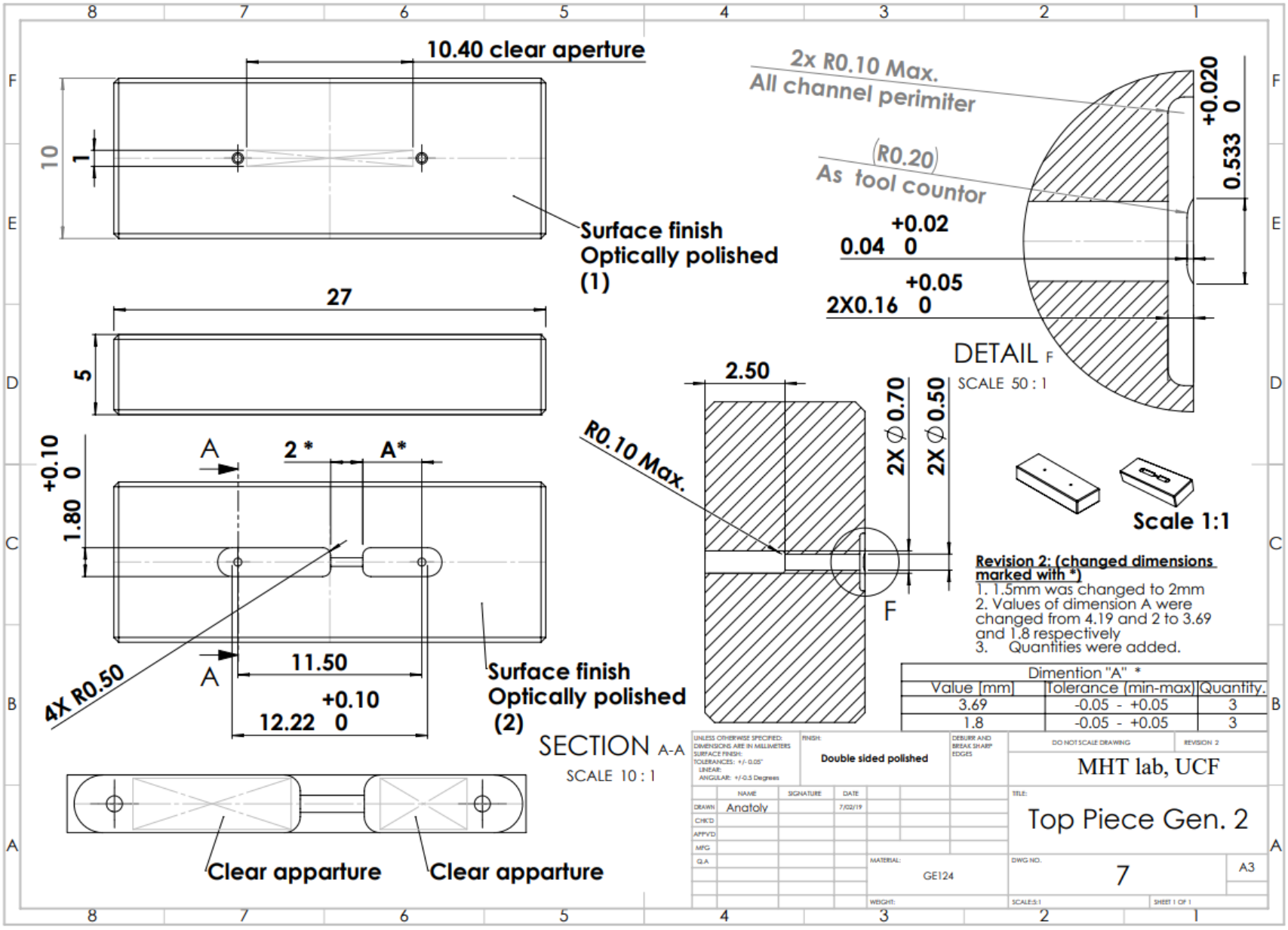
10.40 clear aperture
10
1
Surface finish
Optically polished
(1)
27
5
+0.10
0
1.80
A
2 *
A*
A
11.50
+0.10
12.22 0
4X R0.50
Surface finish
Optically polished
(2)
SECTION A-A
SCALE 10 : 1
Clear apparture
Clear apparture
2x R0.10 Max.
All channel perimiter
(R0.20)
As tool countor
+0.02
0.04 0
+0.05
2X0.16 0
+0.020
0
0.533
DETAIL F
SCALE 50 : 1
2.50
R0.10 Max.
2X ∅0.70
2X ∅0.50
F
Scale 1:1
Revision 2: (changed dimensions marked with *)
1. 1.5mm was changed to 2mm
2. Values of dimension A were changed from 4.19 and 2 to 3.69 and 1.8 respectively
3. Quantities were added.
Dimention "A" *
Value [mm] | Tolerance (min-max) | Quantity
3.69 | -0.05 - +0.05 | 3
1.8 | -0.05 - +0.05 | 3
UNLESS OTHERWISE SPECIFIED: DIMENSIONS ARE IN MILLIMETERS SURFACE FINISH: TOLERANCES: +/- 0.05" LINEAR: ANGULAR: +/-0.5 Degrees
FINISH: Double sided polished
DEBURR AND BREAK SHARP EDGES
DO NOT SCALE DRAWING
REVISION 2
MHT lab, UCF
NAME SIGNATURE DATE
DRAWN Anatoly 7/02/19
CHK'D
APP'VD
MFG
Q.A
TITLE: Top Piece Gen. 2
MATERIAL: GE124
DWG NO. 7
A3
WEIGHT:
SCALE:5:1
SHEET 1 OF 1

APPENDIX F – COPY RIGHT AGREEMENT

For APS journal:

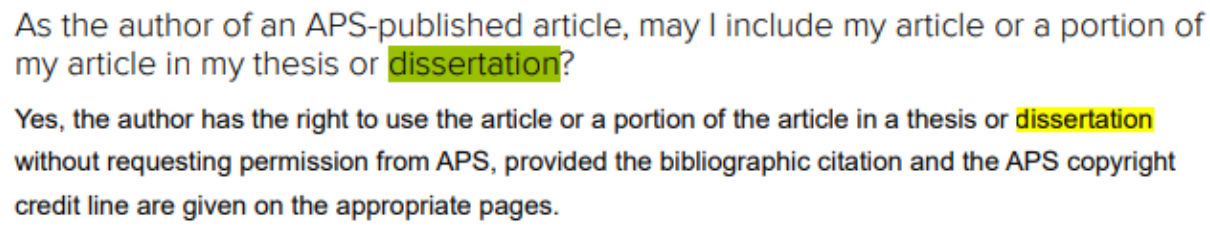

https://journals.aps.org/copyrightFAQ.html

For Elsevier journals:

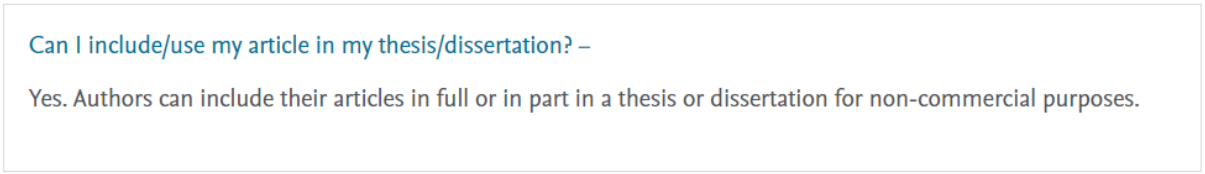

https://www.elsevier.com/about/policies/copyright/permissions

REFERENCES

[1] L. Cheng, G. Ribatski, J. Moreno Quibén, and J. R. Thome, "New prediction methods for CO2 evaporation inside tubes: Part I – A two-phase flow pattern map and a flow pattern based phenomenological model for two-phase flow frictional pressure drops," *Int. J. Heat Mass Transf.*, vol. 51, no. 1, pp. 111–124, Jan. 2008, doi: 10.1016/j.ijheatmasstransfer.2007.04.002.

[2] R. M. Tiggelaar *et al.*, "Fabrication, mechanical testing and application of high-pressure glass microreactor chips," *Chem. Eng. J.*, vol. 131, no. 1, pp. 163–170, Jul. 2007, doi: 10.1016/j.cej.2006.12.036.

[3] V. Dostal, P. Hejzlar, and M. J. Driscoll, "The Supercritical Carbon Dioxide Power Cycle: Comparison to Other Advanced Power Cycles," *Nucl. Technol.*, vol. 154, no. 3, pp. 283–301, Jun. 2006, doi: 10.13182/NT06-A3734.

[4] E. I. Koytsoumpa, C. Bergins, and E. Kakaras, "The CO2 economy: Review of CO2 capture and reuse technologies," *J. Supercrit. Fluids*, Jul. 2017, doi: 10.1016/j.supflu.2017.07.029.

[5] E. G. Feher, "The supercritical thermodynamic power cycle," *Energy Convers.*, vol. 8, no. 2, pp. 85–90, Sep. 1968, doi: 10.1016/0013-7480(68)90105-8.

[6] Y. Ahn *et al.*, "Review of supercritical CO2 power cycle technology and current status of research and development," *Nucl. Eng. Technol.*, vol. 47, no. 6, pp. 647–661, Oct. 2015, doi: 10.1016/j.net.2015.06.009.

[7] "Modelling and simulation of CO2 (carbon dioxide) bottoming cycles for offshore oil and gas installations at design and off-design conditions," *Energy*, vol. 59, pp. 513–520, Sep. 2013, doi: 10.1016/j.energy.2013.06.071.

[8] "Carbon dioxide—new uses for an old refrigerant," *Int. J. Refrig.*, vol. 28, no. 8, pp. 1140–1148, Dec. 2005, doi: 10.1016/j.ijrefrig.2005.09.005.

[9] K. Nikitin, Y. Kato, and L. Ngo, "Printed circuit heat exchanger thermal–hydraulic performance in supercritical CO2 experimental loop," *Int. J. Refrig.*, vol. 29, no. 5, pp. 807–814, Aug. 2006, doi: 10.1016/j.ijrefrig.2005.11.005.

[10] "High performance printed circuit heat exchanger," *Appl. Therm. Eng.*, vol. 27, no. 10, pp. 1702–1707, Jul. 2007, doi: 10.1016/j.applthermaleng.2006.07.007.

[11] R. Span and W. Wagner, "A new equation of state for carbon dioxide covering the fluid region from the triple-point temperature to 1100 K at pressures up to 800 MPa," *J. Phys. Chem. Ref. Data*, vol. 25, no. 6, pp. 1509–1596, 1996.

[12] D. B. Tuckerman and R. F. W. Pease, "High-performance heat sinking for VLSI," *IEEE Electron Device Lett.*, vol. 2, no. 5, pp. 126–129, May 1981, doi: 10.1109/EDL.1981.25367.

[13] S. G. Kandlikar, "History, Advances, and Challenges in Liquid Flow and Flow Boiling Heat Transfer in Microchannels: A Critical Review," *J. Heat Transf.*, vol. 134, no. 3, pp. 034001-034001–15, Jan. 2012, doi: 10.1115/1.4005126.

[14] T. Dixit and I. Ghosh, “Review of micro- and mini-channel heat sinks and heat exchangers for single phase fluids,” *Renew. Sustain. Energy Rev.*, vol. 41, pp. 1298–1311, Jan. 2015, doi: 10.1016/j.rser.2014.09.024.

[15] A. Dewan and P. Srivastava, “A review of heat transfer enhancement through flow disruption in a microchannel,” *J. Therm. Sci.*, vol. 24, no. 3, pp. 203–214, Jun. 2015, doi: 10.1007/s11630-015-0775-1.

[16] Y. Wang and Y. Peles, “An Experimental Study of Passive and Active Heat Transfer Enhancement in Microchannels,” *J. Heat Transf.*, vol. 136, no. 3, pp. 031901-031901–11, Nov. 2013, doi: 10.1115/1.4025558.

[17] Y. Wang, F. Houshmand, D. Elcock, and Y. Peles, “Convective heat transfer and mixing enhancement in a microchannel with a pillar,” *Int. J. Heat Mass Transf.*, vol. 62, no. Supplement C, pp. 553–561, Jul. 2013, doi: 10.1016/j.ijheatmasstransfer.2013.03.034.

[18] X. Yu, C. Woodcock, J. Plawsky, and Y. Peles, “An investigation of convective heat transfer in microchannel with Piranha Pin Fin,” *Int. J. Heat Mass Transf.*, vol. 103, no. Supplement C, pp. 1125–1132, Dec. 2016, doi: 10.1016/j.ijheatmasstransfer.2016.07.069.

[19] S.-M. Kim and I. Mudawar, “Review of databases and predictive methods for heat transfer in condensing and boiling mini/micro-channel flows,” *Int. J. Heat Mass Transf.*, vol. 77, pp. 627–652, Oct. 2014, doi: 10.1016/j.ijheatmasstransfer.2014.05.036.

[20] D. E. Kim, D. I. Yu, D. W. Jerng, M. H. Kim, and H. S. Ahn, “Review of boiling heat transfer enhancement on micro/nanostructured surfaces,” *Exp. Therm. Fluid Sci.*, vol. 66, pp. 173–196, Sep. 2015, doi: 10.1016/j.expthermflusci.2015.03.023.

[21] Y. Wang and Y. Peles, “Subcooled flow boiling in a microchannel with a pin fin and a liquid jet in crossflow,” *Int. J. Heat Mass Transf.*, vol. 86, no. Supplement C, pp. 165–173, Jul. 2015, doi: 10.1016/j.ijheatmasstransfer.2015.02.080.

[22] A. Koşar and Y. Peles, “Boiling heat transfer in a hydrofoil-based micro pin fin heat sink,” *Int. J. Heat Mass Transf.*, vol. 50, no. 5, pp. 1018–1034, Mar. 2007, doi: 10.1016/j.ijheatmasstransfer.2006.07.032.

[23] A. Kosar, C.-J. Kuo, and Y. Peles, “Hydoroil-Based Micro Pin Fin Heat Sink,” pp. 563–570, Jan. 2006, doi: 10.1115/IMECE2006-13257.

[24] X. Yu, C. Woodcock, Y. Wang, J. Plawsky, and Y. Peles, “A Comparative Study of Flow Boiling in a Microchannel With Piranha Pin Fins,” *J. Heat Transf.*, vol. 138, no. 11, pp. 111502-111502–12, Jun. 2016, doi: 10.1115/1.4033743.

[25] W. Wibel, U. Schygulla, and J. J. Brandner, “Micro device for liquid cooling by evaporation of R134a,” *Chem. Eng. J.*, vol. 167, no. 2, pp. 705–712, Mar. 2011, doi: 10.1016/j.cej.2010.11.051.

[26] S. Basu, S. Ndao, G. J. Michna, Y. Peles, and M. K. Jensen, “Flow Boiling of R134a in Circular Microtubes—Part I: Study of Heat Transfer Characteristics,” *J. Heat Transf.*, vol. 133, no. 5, May 2011, doi: 10.1115/1.4003159.

[27] S. Basu, S. Ndao, G. J. Michna, Y. Peles, and M. K. Jensen, “Flow Boiling of R134a in Circular Microtubes—Part II: Study of Critical Heat Flux Condition,” *J. Heat Transf.*, vol. 133, no. 5, May 2011, doi: 10.1115/1.4003160.

[28] N. Al-Khalidy, “An experimental study of an ejector cycle refrigeration machine operating on R113: Etude expérimentale d’une machine frigorifique à éjecteur au R113,” *Int. J. Refrig.*, vol. 21, no. 8, pp. 617–625, Dec. 1998, doi: 10.1016/S0140-7007(98)00030-9.

[29] D. W. Zhou and C. F. Ma, “Local jet impingement boiling heat transfer with R113,” *Heat Mass Transf.*, vol. 40, no. 6, pp. 539–549, May 2004, doi: 10.1007/s00231-003-0463-7.

[30] S. Marre, A. Adamo, S. Basak, C. Aymonier, and K. F. Jensen, “Design and Packaging of Microreactors for High Pressure and High Temperature Applications,” *Ind. Eng. Chem. Res.*, vol. 49, no. 22, pp. 11310–11320, Nov. 2010, doi: 10.1021/ie101346u.

[31] P. P. P. M. Lerou *et al.*, “Progress in Micro Joule-Thomson Cooling at Twente University,” in *Cryocoolers 13*, Boston, MA, 2005, pp. 489–496. doi: 10.1007/0-387-27533-9_62.

[32] H. S. Cao *et al.*, “Joule-Thomson microcooling developments at University of Twente,” *IOP Conf. Ser. Mater. Sci. Eng.*, vol. 171, no. 1, p. 012064, 2017, doi: 10.1088/1757-899X/171/1/012064.

[33] M.-H. Lin, P. E. Bradley, M. L. Huber, R. Lewis, R. Radebaugh, and Y. C. Lee, “Mixed refrigerants for a glass capillary micro cryogenic cooler,” *Cryogenics*, vol. 50, no. 8, pp. 439–442, Aug. 2010, doi: 10.1016/j.cryogenics.2010.04.004.

[34] I. L. Pioro, W. Rohsenow, and S. S. Doerffer, “Nucleate pool-boiling heat transfer. I: review of parametric effects of boiling surface,” *Int. J. Heat Mass Transf.*, vol. 47, no. 23, pp. 5033–5044, Nov. 2004, doi: 10.1016/j.ijheatmasstransfer.2004.06.019.

[35] “Heat Transfer and Wall Heat Flux Partitioning During Subcooled Flow Nucleate Boiling—A Review | Journal of Heat Transfer | ASME Digital Collection.” https://asmedigitalcollection.asme.org/heattransfer/article/128/12/1243/467536/Heat-Transfer-and-Wall-Heat-Flux-Partitioning (accessed Jan. 08, 2020).

[36] R. K. Zeytounian, “The BeÂ nard ± Marangoni thermocapillary-instability problem,” p. 28.

[37] A. Karbalaei, R. Kumar, and H. J. Cho, “Thermocapillarity in Microfluidics—A Review,” *Micromachines*, vol. 7, no. 1, p. 13, Jan. 2016, doi: 10.3390/mi7010013.

[38] D. Hellenschmidt *et al.*, “New insights on boiling carbon dioxide flow in mini- and micro-channels for optimal silicon detector cooling,” *Nucl. Instrum. Methods Phys. Res. Sect. Accel. Spectrometers Detect. Assoc. Equip.*, vol. 958, p. 162535, Apr. 2020, doi: 10.1016/j.nima.2019.162535.

[39] J. R. Thome and J. El Hajal, “Flow boiling heat transfer to carbon dioxide: general prediction method,” *Int. J. Refrig.*, vol. 27, no. 3, pp. 294–301, May 2004, doi: 10.1016/j.ijrefrig.2003.08.003.

[40] L. Cheng, G. Ribatski, L. Wojtan, and J. R. Thome, “New flow boiling heat transfer model and flow pattern map for carbon dioxide evaporating inside horizontal tubes,” *Int. J. Heat Mass Transf.*, vol. 49, no. 21, pp. 4082–4094, Oct. 2006, doi: 10.1016/j.ijheatmasstransfer.2006.04.003.

[41] M. Ducoulombier, S. Colasson, J. Bonjour, and P. Haberschill, “Carbon dioxide flow boiling in a single microchannel – Part I: Pressure drops,” *Exp. Therm. Fluid Sci.*, vol. 35, no. 4, pp. 581–596, May 2011, doi: 10.1016/j.expthermflusci.2010.12.010.

[42] M. Ducoulombier, S. Colasson, J. Bonjour, and P. Haberschill, “Carbon dioxide flow boiling in a single microchannel – Part II: Heat transfer,” *Exp. Therm. Fluid Sci.*, vol. 35, no. 4, pp. 597–611, May 2011, doi: 10.1016/j.expthermflusci.2010.11.014.

[43] L. Cheng, G. Ribatski, and J. R. Thome, “New prediction methods for CO2 evaporation inside tubes: Part II—An updated general flow boiling heat transfer model based on flow patterns,” *Int. J. Heat Mass Transf.*, vol. 51, no. 1, pp. 125–135, Jan. 2008, doi: 10.1016/j.ijheatmasstransfer.2007.04.001.

[44] Y. Y. Hsu, “On the Size Range of Active Nucleation Cavities on a Heating Surface,” *J. Heat Transf.*, vol. 84, no. 3, pp. 207–213, Aug. 1962, doi: 10.1115/1.3684339.

[45] E. J. Davis and G. H. Anderson, “The incipience of nucleate boiling in forced convection flow,” *AIChE J.*, vol. 12, no. 4, pp. 774–780, 1966, doi: 10.1002/aic.690120426.

[46] J. H. Lienhard, “Correlation for the limiting liquid superheat,” *Chem. Eng. Sci.*, vol. 31, no. 9, pp. 847–849, Jan. 1976, doi: 10.1016/0009-2509(76)80063-2.

[47] “(PDF) A general correlation for heat transfer during subcooled boiling in pipes and annuli.” https://www.researchgate.net/publication/282578410_A_general_correlation_for_heat_transfer_during_subcooled_boiling_in_pipes_and_annuli (accessed Nov. 12, 2019).

[48] S. G. Kandlikar, “A General Correlation for Saturated Two-Phase Flow Boiling Heat Transfer Inside Horizontal and Vertical Tubes,” *J. Heat Transf.*, vol. 112, no. 1, pp. 219–228, Feb. 1990, doi: 10.1115/1.2910348.

[49] Y. K. Prajapati and P. Bhandari, “Flow boiling instabilities in microchannels and their promising solutions–A review,” *Exp. Therm. Fluid Sci.*, vol. 88, pp. 576–593, 2017.

[50] C.-J. Kuo and Y. Peles, “Flow boiling instabilities in microchannels and means for mitigation by reentrant cavities,” *J. Heat Transf.*, vol. 130, no. 7, 2008.

[51] D. Bogojevic, K. Sefiane, G. Duursma, and A. J. Walton, “Bubble dynamics and flow boiling instabilities in microchannels,” *Int. J. Heat Mass Transf.*, vol. 58, no. 1–2, pp. 663–675, 2013.

[52] G. Wang, P. Cheng, and H. Wu, “Unstable and stable flow boiling in parallel microchannels and in a single microchannel,” *Int. J. Heat Mass Transf.*, vol. 50, no. 21–22, pp. 4297–4310, 2007.

[53] A. E. Bergles and S. G. Kandlikar, “On the nature of critical heat flux in microchannels,” *J Heat Transf.*, vol. 127, no. 1, pp. 101–107, 2005.

[54] R. Revellin and J. R. Thome, “A theoretical model for the prediction of the critical heat flux in heated microchannels,” *Int. J. Heat Mass Transf.*, vol. 51, no. 5–6, pp. 1216–1225, 2008.

[55] S. Xie, M. S. Beni, J. Cai, and J. Zhao, “Review of critical-heat-flux enhancement methods,” *Int. J. Heat Mass Transf.*, vol. 122, pp. 275–289, 2018.

[56] A. Bar-Cohen and P. Wang, “On-chip thermal management and hot-spot remediation,” in *Nano-Bio-Electronic, Photonic and MEMS Packaging*, Springer, 2010, pp. 349–429.

[57] A. Bar-Cohen, “Gen-3 thermal management technology: role of microchannels and nanostructures in an embedded cooling paradigm,” *J. Nanotechnol. Eng. Med.*, vol. 4, no. 2, 2013.

[58] Y. Won, J. Cho, D. Agonafer, M. Asheghi, and K. E. Goodson, “Fundamental cooling limits for high power density gallium nitride electronics,” *IEEE Trans. Compon. Packag. Manuf. Technol.*, vol. 5, no. 6, pp. 737–744, 2015.

[59] H. Seon Ahn and M. Hwan Kim, “A review on critical heat flux enhancement with nanofluids and surface modification,” *J. Heat Transf.*, vol. 134, no. 2, 2012.

[60] S. Mori and Y. Utaka, “Critical heat flux enhancement by surface modification in a saturated pool boiling: a review,” *Int. J. Heat Mass Transf.*, vol. 108, pp. 2534–2557, 2017.

[61] B. S. Kim, G. Choi, D. I. Shim, K. M. Kim, and H. H. Cho, “Surface roughening for hemi-wicking and its impact on convective boiling heat transfer,” *Int. J. Heat Mass Transf.*, vol. 102, pp. 1100–1107, 2016.

[62] A. Fazeli, M. Mortazavi, and S. Moghaddam, “Hierarchical biphilic micro/nanostructures for a new generation phase-change heat sink,” *Appl. Therm. Eng.*, vol. 78, pp. 380–386, 2015.

[63] Y. Zhu *et al.*, “Surface structure enhanced microchannel flow boiling,” *J. Heat Transf.*, vol. 138, no. 9, 2016.

[64] A. Parahovnik, M. Asadzadeh, S. S. Vasu, and Y. Peles, “Subcooled Flow Boiling of Carbon Dioxide Near the Critical Point Inside a Microchannel,” *Phys. Rev. Appl.*, vol. 14, no. 5, p. 054050, Nov. 2020, doi: 10.1103/PhysRevApplied.14.054050.

[65] B. B. Mikic, W. M. Rohsenow, and P. Griffith, “On bubble growth rates,” *Int. J. Heat Mass Transf.*, vol. 13, no. 4, pp. 657–666, Apr. 1970, doi: 10.1016/0017-9310(70)90040-2.

[66] M. S. Plesset, “The dynamics of cavitation bubbles,” *J. Appl. Mech.*, vol. 16, pp. 277–282, 1949.

[67] C. E. Brennen, *Cavitation and Bubble Dynamics*. Cambridge University Press, 2014.

[68] W. H. Besant, *A treatise on hydrostatics and hydrodynamics*. Deighton, Bell, 1859.

[69] Lord Rayleigh, “VIII. On the pressure developed in a liquid during the collapse of a spherical cavity,” *Lond. Edinb. Dublin Philos. Mag. J. Sci.*, vol. 34, no. 200, pp. 94–98, 1917.

[70] Y. Y. Hsu, “On the size range of active nucleation cavities on a heating surface,” 1962.

[71] E. J. Davis and G. H. Anderson, “The incipience of nucleate boiling in forced convection flow,” *AIChE J.*, vol. 12, no. 4, pp. 774–780, 1966.

[72] R. L. Mohanty and M. K. Das, “A critical review on bubble dynamics parameters influencing boiling heat transfer,” *Renew. Sustain. Energy Rev.*, vol. 78, pp. 466–494, Oct. 2017, doi: 10.1016/j.rser.2017.04.092.

[73] X. Lei, W. Zhang, J. Zhang, N. Dinh, and H. Li, “Experimental investigations on the boiling heat transfer of horizontal flow in the near-critical region,” *Int. J. Heat Mass Transf.*, vol. 125, pp. 618–628, Oct. 2018, doi: 10.1016/j.ijheatmasstransfer.2018.04.043.

[74] H.-S. Pham *et al.*, “A numerical study of cavitation and bubble dynamics in liquid CO2 near the critical point,” *Int. J. Heat Mass Transf.*, vol. 102, pp. 174–185, 2016.

[75] E. R. Hosler, “FLOW PATTERNS IN HIGH PRESSURE TWO-PHASE (STEAM--WATER) FLOW WITH HEAT ADDITION.,” Bettis Atomic Power Lab., Pittsburgh, Pa., WAPD-T-1824; CONF-670807-1, Jan. 1967. Accessed: Feb. 28, 2021. [Online]. Available: https://www.osti.gov/biblio/4844120

[76] V. Prodanovic, D. Fraser, and M. Salcudean, “Bubble behavior in subcooled flow boiling of water at low pressures and low flow rates,” *Int. J. Multiph. Flow*, vol. 28, no. 1, pp. 1–19, Jan. 2002, doi: 10.1016/S0301-9322(01)00058-1.

[77] F. C. GUNTHER, “Photographic Study of Surface-Boiling Heat Transfer to Water Forced Convection,” *Trans ASME*, vol. 73–2, pp. 115–123, 1951.

[78] S. G. Kandlikar, V. R. Mizo, and M. D. Cartwright, “Investigation of bubble departure mechanism in subcooled flow boiling of water using high-speed photography,” in *Convective Flow Boiling*, CRC Press, 2019, pp. 161–166.

[79] W. C. Chen, J. F. Klausner, and R. Mei, “A simplified model for predicting vapor bubble growth rates in heterogeneous boiling,” 1995.

[80] S. G. Kandlikar and B. J. Stumm, “A control volume approach for investigating forces on a departing bubble under subcooled flow boiling,” 1995.

[81] G. Tsung-Chang and S. G. Bankoff, “On the mechanism of forced-convection subcooled nucleate boiling,” 1990.

[82] S. G. Kandlikar and H. Nariai, “Flow boiling in circular tubes,” in *Handbook of Phase Change: Boiling and Condensation*, Routledge, 2019, pp. 367–402.

[83] T. Ghidini, “Materials for space exploration and settlement,” *Nat. Mater.*, vol. 17, no. 10, Art. no. 10, Oct. 2018, doi: 10.1038/s41563-018-0184-4.

[84] L. Vesely, V. Dostal, and S. Entler, “Study of the cooling systems with S-CO2 for the DEMO fusion power reactor,” *Fusion Eng. Des.*, vol. 124, pp. 244–247, Nov. 2017, doi: 10.1016/j.fusengdes.2017.05.029.

[85] R. van Erp, R. Soleimanzadeh, L. Nela, G. Kampitsis, and E. Matioli, “Co-designing electronics with microfluidics for more sustainable cooling,” *Nature*, vol. 585, no. 7824, Art. no. 7824, Sep. 2020, doi: 10.1038/s41586-020-2666-1.

[86] K. Nitsche and J. Straub, “The critical hump of C sub V under microgravity: Results from the D 1 Spacelab experiment Waermekapazitaet,” 1987.

[87] A. Onuki, “Phase Transition Dynamics,” 2006. doi: 10.1016/b0-12-512666-2/00461-2.

[88] A. Onuki, “Thermoacoustic effects in supercritical fluids near the critical point: Resonance, piston effect, and acoustic emission and reflection,” *Phys. Rev. E*, vol. 76, no. 6, p. 061126, 2007.

[89] A. Gorbunov and E. Soboleva, “Three equations of state of near-critical fluids and numerical simulation of the piston effect,” *Microgravity Sci. Technol.*, vol. 32, no. 1, pp. 47–57, 2020.

[90] P. Carlès, “A brief review of the thermophysical properties of supercritical fluids,” *J. Supercrit. Fluids*, vol. 53, no. 1, pp. 2–11, Jun. 2010, doi: 10.1016/j.supflu.2010.02.017.

[91] H. Boukari, J. N. Shaumeyer, M. E. Briggs, and R. W. Gammon, “Critical speeding up in pure fluids,” *Phys. Rev. A*, vol. 41, no. 4, pp. 2260–2263, Feb. 1990, doi: 10.1103/PhysRevA.41.2260.

[92] B. Zappoli and P. Carles, “The thermo-acoustic nature of the critical speeding up,” *Eur. J. Mech. B Fluids*, vol. 14, no. 1, pp. 41–65, 1995.

[93] Y. Garrabos, R. Wunenburger, J. Hegseth, C. Lecoutre-Chabot, and D. Beysens, “Critical boiling phenomena observed in microgravity,” in *AIP Conference Proceedings*, 2000, vol. 504, no. 1, pp. 737–743.

[94] Y. Garrabos, D. Beysens, C. Lecoutre, A. Dejoan, V. Polezhaev, and V. Emelianov, "Thermoconvectional phenomena induced by vibrations in supercritical S F 6 under weightlessness," *Phys. Rev. E*, vol. 75, no. 5, p. 056317, 2007.

[95] R. Wunenburger, Y. Garrabos, C. Lecoutre-Chabot, D. Beysens, and J. Hegseth, "Thermalization of a two-phase fluid in low gravity: heat transferred from cold to hot," *Phys. Rev. Lett.*, vol. 84, no. 18, p. 4100, 2000.

[96] A. B. Kogan, D. Murphy, and H. Meyer, "Rayleigh-Bénard convection onset in a compressible fluid: 3 He near T C," *Phys. Rev. Lett.*, vol. 82, no. 23, p. 4635, 1999.

[97] A. B. Kogan and H. Meyer, "Heat transfer and convection onset in a compressible fluid: 3 He near the critical point," *Phys. Rev. E*, vol. 63, no. 5, p. 056310, 2001.

[98] Y. Miura *et al.*, "High-speed observation of the piston effect near the gas-liquid critical point," *Phys. Rev. E*, vol. 74, no. 1, p. 010101, 2006.

[99] B. Shen and P. Zhang, "Thermoacoustic waves along the critical isochore," *Phys. Rev. E*, vol. 83, no. 1, p. 011115, 2011.

[100] A. Furukawa and A. Onuki, "Convective heat transport in compressible fluids," *Phys. Rev. E*, vol. 66, no. 1, p. 016302, 2002.

[101] Y. Chiwata and A. Onuki, "Thermal plumes and convection in highly compressible fluids," *Phys. Rev. Lett.*, vol. 87, no. 14, p. 144301, 2001.

[102] S. Amiroudine and B. Zappoli, "Piston-Effect-Induced Thermal Oscillations at the Rayleigh-Bénard Threshold in Supercritical H e 3," *Phys. Rev. Lett.*, vol. 90, no. 10, p. 105303, 2003.

[103] G. Accary, I. Raspo, P. Bontoux, and B. Zappoli, "Three-dimensional Rayleigh–Bénard instability in a supercritical fluid," *Comptes Rendus Mécanique*, vol. 332, no. 3, pp. 209–216, 2004.

[104] B. Zappoli, "Influence of Convection on the Piston Effect," p. 13.

[105] P. Carles and B. Zappoli, "The unexpected response of near-critical fluids to low-frequency vibrations," *Phys. Fluids*, vol. 7, no. 11, pp. 2905–2914, 1995.

[106] I. Raspo, S. Meradji, and B. Zappoli, "Heterogeneous reaction induced by the piston effect in supercritical binary mixtures," *Chem. Eng. Sci.*, vol. 62, no. 16, pp. 4182–4192, 2007.

[107] M. Barmatz, I. Hahn, J. A. Lipa, and R. V. Duncan, "Critical phenomena in microgravity: Past, present, and future," *Rev. Mod. Phys.*, vol. 79, no. 1, pp. 1–52, Jan. 2007, doi: 10.1103/RevModPhys.79.1.

[108] C. Dang and E. Hihara, "In-tube cooling heat transfer of supercritical carbon dioxide. Part 1. Experimental measurement," *Int. J. Refrig.*, vol. 27, no. 7, pp. 736–747, Nov. 2004, doi: 10.1016/j.ijrefrig.2004.04.018.

[109] S. M. Liao and T. S. Zhao, "An experimental investigation of convection heat transfer to supercritical carbon dioxide in miniature tubes," *Int. J. Heat Mass Transf.*, vol. 45, no. 25, pp. 5025–5034, Dec. 2002, doi: 10.1016/S0017-9310(02)00206-5.

[110] X. Fang and P. S. Hrnjak, "Heat Transfer and Pressure Drop of Gas Coolers," p. 18.

[111] X. L. Huai, S. Koyama, and T. S. Zhao, “An experimental study of flow and heat transfer of supercritical carbon dioxide in multi-port mini channels under cooling conditions,” *Chem. Eng. Sci.*, vol. 60, no. 12, pp. 3337–3345, Jun. 2005, doi: 10.1016/j.ces.2005.02.039.

[112] H.-K. Oh and C.-H. Son, “New correlation to predict the heat transfer coefficient in-tube cooling of supercritical CO2 in horizontal macro-tubes,” *Exp. Therm. Fluid Sci.*, vol. 34, no. 8, pp. 1230–1241, Nov. 2010, doi: 10.1016/j.expthermflusci.2010.05.002.

[113] A. Onuki, H. Hao, and R. A. Ferrell, “Fast adiabatic equilibration in a single-component fluid near the liquid-vapor critical point,” *Phys. Rev. A*, vol. 41, no. 4, p. 2256, 1990.

[114] B. Zappoli, D. Beysens, and Y. Garrabos, *Heat Transfers and Related Effects in Supercritical Fluids*, vol. 108. Dordrecht: Springer Netherlands, 2015. doi: 10.1007/978-94-017-9187-8.

[115] J. P. Joule and W. Thomson, “LXXVI. On the thermal effects experienced by air in rushing through small apertures,” *Lond. Edinb. Dublin Philos. Mag. J. Sci.*, vol. 4, no. 28, pp. 481–492, 1852.

[116] R. Radebaugh, “Cryocoolers: the state of the art and recent developments,” *J. Phys. Condens. Matter*, vol. 21, no. 16, p. 164219, 2009.

[117] J. R. Barbosa Jr, G. B. Ribeiro, and P. A. de Oliveira, “A state-of-the-art review of compact vapor compression refrigeration systems and their applications,” *Heat Transf. Eng.*, vol. 33, no. 4–5, pp. 356–374, 2012.

[118] J. P. Chen, J. P. Liu, Z. J. Chen, and Y. M. Niu, “Trans-critical R744 and two-phase flow through short tube orifices,” *Int. J. Therm. Sci.*, vol. 43, no. 6, pp. 623–630, 2004.

[119] J. G. Collier and J. R. Thome, “Convective Boiling and Condensation, Oxford University Press, Oxford, 1994”.

[120] D. L. da Silva, C. J. Hermes, C. Melo, J. M. Gonçalves, and G. C. Weber, “A study of transcritical carbon dioxide flow through adiabatic capillary tubes,” *Int. J. Refrig.*, vol. 32, no. 5, pp. 978–987, 2009.

[121] C. J. Hermes, D. L. da Silva, C. Melo, J. M. Gonçalves, and G. C. Weber, “Algebraic solution of transcritical carbon dioxide flow through adiabatic capillary tubes,” *Int. J. Refrig.*, vol. 32, no. 5, pp. 973–977, 2009.

[122] C. J. Hermes, C. Melo, and J. M. Gonçalves, “Modeling of non-adiabatic capillary tube flows: A simplified approach and comprehensive experimental validation,” *Int. J. Refrig.*, vol. 31, no. 8, pp. 1358–1367, 2008.

[123] O. Garcıa-Valladares, “Review of numerical simulation of capillary tube using refrigerant mixtures,” *Appl. Therm. Eng.*, vol. 24, no. 7, pp. 949–966, 2004.

[124] L. Cecchinato, M. Corradi, E. Fornasieri, G. Schiochet, and C. Zilio, “Assessment on the use of common correlations to predict the mass-flow rate of carbon dioxide through capillary tubes in transcritical cycles,” *Int. J. Refrig.*, vol. 32, no. 5, pp. 1041–1048, 2009.

[125] T. Yilmaz and S. U\" nal, “General equation for the design of capillary tubes,” 1996.

[126] R. E. Henry, “The two-phase critical discharge of initially saturated or subcooled liquid,” *Nucl. Sci. Eng.*, vol. 41, no. 3, pp. 336–342, 1970.

[127] K. Nilpueng and S. Wongwises, “Review on the experimental studies of refrigerant flow mechanisms inside short-tube orifices,” *Int. J. Refrig.*, vol. 35, no. 1, pp. 27–35, 2012.

[128] K. Nilpueng, C. Supavarasuwat, and S. Wongwises, “Flow pattern, mass flow rate, pressure distribution, and temperature distribution of two-phase flow of HFC-134a inside short-tube orifices,” *Int. J. Refrig.*, vol. 32, no. 8, pp. 1864–1875, 2009.

[129] “AJA Sputter Deposition | CNF Users.” https://www.cnfusers.cornell.edu/node/138 (accessed Jan. 10, 2020).

[130] “Photolithography | CNF Users.” https://www.cnfusers.cornell.edu/Photolithography (accessed Jan. 10, 2020).

[131] “AJA Ion Mill | CNF Users.” https://www.cnfusers.cornell.edu/node/114 (accessed Jan. 10, 2020).

[132] “Oxford PECVD | CNF Users.” https://www.cnfusers.cornell.edu/node/188 (accessed Jan. 10, 2020).

[133] “P7 Profilometer | CNF Users.” https://www.cnfusers.cornell.edu/node/93 (accessed Jan. 10, 2020).

[134] ASME, “ASME BPVC Offerings - Boilers and Pressure Vessels.” https://resources.asme.org/https/resources.asme.org/bpvc-secs-iv-vi-vii-xii-boilers-pressure-vessels-products (accessed Jan. 09, 2020).

[135] “Property Information.” http://www-materials.eng.cam.ac.uk/mpsite/properties/non-IE/elongation.html (accessed Jan. 10, 2020).

[136] R. J. Moffat, “Describing the uncertainties in experimental results,” *Exp. Therm. Fluid Sci.*, vol. 1, no. 1, pp. 3–17, Jan. 1988, doi: 10.1016/0894-1777(88)90043-X.

[137] F. P. Incropera, D. P. DeWitt, T. L. Bergman, and A. S. Lavine, *Fundamentals of heat and mass transfer*, vol. 6. Wiley New York, 1996.

[138] C. F. Colebrook, C. M. White, and G. I. Taylor, “Experiments with fluid friction in roughened pipes,” *Proc. R. Soc. Lond. Ser. - Math. Phys. Sci.*, vol. 161, no. 906, pp. 367–381, Aug. 1937, doi: 10.1098/rspa.1937.0150.

[139] C. F. Colebrook, “Turbulent flow in pipes, with particular reference to the transition region between the smooth and rough pipe laws.,” *J. Inst. Civ. Eng.*, vol. 11, no. 4, pp. 133–156, Feb. 1939, doi: 10.1680/ijoti.1939.13150.

[140] “Convection Heat Transfer by Adrian, Bejan.” https://www.biblio.com/convection-heat-transfer-by-adrian-bejan/work/242193 (accessed Aug. 16, 2019).

[141] T. L. Bergman, A. S. Lavine, F. P. Incropera, and D. P. DeWitt, *Fundamentals of Heat and Mass Transfer*, 7 edition. Chichester: Wiley, 2011.

[142] “Heat Transfer Characteristics in Partial Boiling, Fully Developed Boiling, and Significant Void Flow Regions of Subcooled Flow Boiling | Journal of Heat Transfer | ASME Digital Collection.” https://asmedigitalcollection.asme.org/heattransfer/article/120/2/395/456739/Heat-Transfer-Characteristics-in-Partial-Boiling (accessed Nov. 12, 2019).

[143] V. V. Gnielinski, “Neue Gleichungen fiir den Wiirme- und den Stoffiibergang in turbulent durchstrSmten Rohren und Kan/ilen,” p. 9, 1975.

[144] M. Ducoulombier, S. Colasson, J. Bonjour, and P. Haberschill, “Carbon dioxide flow boiling in a single microchannel – Part II: Heat transfer,” *Exp. Therm. Fluid Sci.*, vol. 35, no. 4, pp. 597–611, May 2011, doi: 10.1016/j.expthermflusci.2010.11.014.

[145] L. Cheng, G. Ribatski, and J. R. Thome, “New prediction methods for CO2 evaporation inside tubes: Part II—An updated general flow boiling heat transfer model based on flow patterns,” *Int. J. Heat Mass Transf.*, vol. 51, no. 1, pp. 125–135, Jan. 2008, doi: 10.1016/j.ijheatmasstransfer.2007.04.001.

[146] A. Parahovnik and Y. Peles, “High pressure saturated flow boiling of CO2 at the micro scale,” *Int. J. Heat Mass Transf.*, vol. 186, p. 122449, 2022.

[147] S. G. Kandlikar, “A general correlation for saturated two-phase flow boiling heat transfer inside horizontal and vertical tubes,” 1990.

[148] M. M. Shah, “Chart correlation for saturated boiling heat transfer: equations and further study,” *ASHRAE Trans.*, vol. 88, 1982.

[149] M. M. Shah and S. MM, “A new correlation for heat transfer during boiling flow through pipes.,” 1976.

[150] L. A. Bromley, N. R. LeRoy, and J. A. Robbers, “Heat transfer in forced convection film boiling,” *Ind. Eng. Chem.*, vol. 45, no. 12, pp. 2639–2646, 1953.

[151] Y. Katto and H. Ohno, “An improved version of the generalized correlation of critical heat flux for the forced convective boiling in uniformly heated vertical tubes,” *Int. J. Heat Mass Transf.*, vol. 27, no. 9, pp. 1641–1648, 1984.

[152] Y. Katto, “A generalized correlation of critical heat flux for the forced convection boiling in vertical uniformly heated round tubes,” *Int. J. Heat Mass Transf.*, vol. 21, no. 12, pp. 1527–1542, 1978.

[153] M. Song, X. Liu, and X. Cheng, “Prediction of critical heat flux (CHF) for the high-pressure region in uniformly heated vertical round tubes,” *Ann. Nucl. Energy*, vol. 158, p. 108303, 2021.

[154] S. S. Kutateladze, “On the transition to film boiling under natural convection,” *Kotloturbostroenie*, vol. 3, pp. 10–12, 1948.

[155] S. G. Kandlikar, “A scale analysis based theoretical force balance model for critical heat flux (CHF) during saturated flow boiling in microchannels and minichannels,” *J. Heat Transf.*, vol. 132, no. 8, 2010.

[156] M. B. Bowers and I. Mudawar, “High flux boiling in low flow rate, low pressure drop mini-channel and micro-channel heat sinks,” *Int. J. Heat Mass Transf.*, vol. 37, no. 2, pp. 321–332, 1994.

[157] A. Parahovnik and Y. Peles, “Bubble dynamics in a subcooled flow boiling of near-critical carbon dioxide,” *Int. J. Heat Mass Transf.*, vol. 183, p. 122191, 2022.

[158] O. Garcia-Valladares, “Numerical simulation of trans-critical carbon dioxide (R744) flow through short tube orifices,” *Appl. Therm. Eng.*, vol. 26, no. 2–3, pp. 144–151, 2006.

[159] Z. Wang, B. Sun, J. Wang, and L. Hou, “Experimental study on the friction coefficient of supercritical carbon dioxide in pipes,” *Int. J. Greenh. Gas Control*, vol. 25, pp. 151–161, Jun. 2014, doi: 10.1016/j.ijggc.2014.04.014.

[160] F. Aakenes, “Frictional pressure-drop models for steady-state and transient two-phase flow of carbon dioxide,” Master’s Thesis, Institutt for energi-og prosessteknikk, 2012.

[161] E. W. Lemmon, M. L. Huber, and M. O. McLinden, “NIST Standard Reference Database 23: Reference Fluid Thermodynamic and Transport Properties-REFPROP, Version 8.0,” Apr. 2007, Sep. 03, 2021.

[162] J. Wang, Z. Wang, and B. Sun, “Improved equation of CO2 Joule–Thomson coefficient,” *J. CO2 Util.*, vol. 19, pp. 296–307, 2017.

[163] J. Benesty, J. Chen, Y. Huang, and I. Cohen, “Pearson Correlation Coefficient,” in *Noise Reduction in Speech Processing*, I. Cohen, Y. Huang, J. Chen, and J. Benesty, Eds. Berlin, Heidelberg: Springer, 2009, pp. 1–4. doi: 10.1007/978-3-642-00296-0_5.

[164] J. G. Collier and J. R. Thome, *Convective Boiling and Condensation*. Clarendon Press, 1994.

[165] A. E. Bergles and S. G. Kandlikar, “On the Nature of Critical Heat Flux in Microchannels,” *J. Heat Transf.*, vol. 127, no. 1, pp. 101–107, Jan. 2005, doi: 10.1115/1.1839587.

[166] *Atkins’ Physical Chemistry*. Accessed: Jun. 05, 2020.

[167] N. Zuber, “On the stability of boiling heat transfer,” *Trans Am Soc Mech Engrs*, vol. 80, 1958.

[168] N. Zuber, “Hydrodynamic aspects of boiling heat transfer,” *Dr. Diss. Univ. Calif.*, 1959.

[169] S. G. Kandlikar, “Fundamental issues related to flow boiling in minichannels and microchannels,” *Exp. Therm. Fluid Sci.*, vol. 26, no. 2, pp. 389–407, Jun. 2002, doi: 10.1016/S0894-1777(02)00150-4.

[170] S. Trasatti, *Atkins’ Physical Chemistry, P. Atkins, J. De Paula, Oxford University Press, Oxford, UK (2006), ISBN: 0198700725*. Pergamon, 2007.

[171] R. Span and W. Wagner, “A New Equation of State for Carbon Dioxide Covering the Fluid Region from the Triple-Point Temperature to 1100 K at Pressures up to 800 MPa,” *J. Phys. Chem. Ref. Data*, vol. 25, no. 6, pp. 1509–1596, Nov. 1996, doi: 10.1063/1.555991.

[172] A. Parahovnik, U. Manda, and Y. Peles, “Heat transfer mode shift to adiabatic thermalization in near-critical carbon dioxide with flow boiling in a microchannel,” *Int. J. Heat Mass Transf.*, vol. 188, p. 122629, 2022.

[173] M. R. Moldover, “Interfacial tension of fluids near critical points and two-scale-factor universality,” *Phys. Rev. A*, vol. 31, no. 2, p. 1022, 1985.

[174] D. Bolmatov, M. Zhernenkov, D. Zav’yalov, S. N. Tkachev, A. Cunsolo, and Y. Q. Cai, “The Frenkel Line: a direct experimental evidence for the new thermodynamic boundary,” *Sci. Rep.*, vol. 5, p. 15850, 2015.

[175] E. Mareev, V. Aleshkevich, F. Potemkin, V. Bagratashvili, N. Minaev, and V. Gordienko, “Anomalous behavior of nonlinear refractive indexes of CO 2 and Xe in supercritical states,” *Opt. Express*, vol. 26, no. 10, pp. 13229–13238, 2018.

[176] E. R. Gopal, “Critical opalescence,” *Resonance*, vol. 5, no. 4, pp. 37–45, 2000.

[177] J. A. White and B. S. Maccabee, “Temperature dependence of critical opalescence in carbon dioxide,” *Phys. Rev. Lett.*, vol. 26, no. 24, p. 1468, 1971.

[178] A. A. A. Abdel-Azim and P. Munk, “Light scattering of liquids and liquid mixtures. 1. Compressibility of pure liquids,” *J. Phys. Chem.*, vol. 91, no. 14, pp. 3910–3914, 1987.

[179] V. G. Puglielli and N. C. Ford Jr, “Turbidity Measurements in S F 6 Near Its Critical Point,” *Phys. Rev. Lett.*, vol. 25, no. 3, p. 143, 1970.

[180] Einstein, A. Ann. Phys. (Leipzig) 1910, 33, 1275.

[181] Yu. A. Chaikina, “Molecular Model for Critical Opalescence of Carbon Dioxide,” *Russ. J. Phys. Chem. B*, vol. 12, no. 7, pp. 1182–1192, Dec. 2018, doi: 10.1134/S1990793118070023.

[182] T. M. Aminabhavi, H. T. S. Phayde, and R. S. Khinnavar, “Densities, Refractive Indices, Speeds of Sound and Shear Viscosities of Diethylene Glycol Dimethyl Ether Methyl Salicylate at Temperatures from 298.15 to 318.15 K,” *Collect. Czechoslov. Chem. Commun.*, vol. 59, no. 7, pp. 1511–1524, 1994, doi: 10.1135/cccc19941511.

[183] T. Moriyoshi, T. Kita, and Y. Uosaki, “Static relative permittivity of carbon dioxide and nitrous oxide up to 30 MPa,” *Berichte Bunsenges. Für Phys. Chem.*, vol. 97, no. 4, pp. 589–596, 1993.

[184] L. Prandtl, “Über Flussigkeitsbewegung bei sehr kleiner Reibung,” *Verhandl III Intern. Math-Kong Heidelb. Teubner Leipz. 1904*, pp. 484–491, 1904.

[185] A. Bejan, *Convection heat transfer*. John wiley & sons, 2013.

[186] W. B. Hall, J. D. Jackson, and A. Watson, “Paper 3: A Review of Forced Convection Heat Transfer to Fluids at Supercritical Pressures,” *Proc. Inst. Mech. Eng. Conf. Proc.*, vol. 182, no. 9, pp. 10–22, Sep. 1967, doi: 10.1243/PIME_CONF_1967_182_262_02.

[187] A. Parahovnik, P. Ahmed, Y. Peles, “Pressure drop and Joule-Thomson effect in a micro orifice with trans critical carbon dioxide flow”, *Journal of supercritical fluids*, under review.

[188] D. Bolmatov, D. Zav’yalov, M. Gao, and M. Zhernenkov, “Structural evolution of supercritical CO2 across the Frenkel line,” *J. Phys. Chem. Lett.*, vol. 5, no. 16, pp. 2785–2790, 2014.